Fall 12-15-2023

Advances in Cellulose Nanomaterial-based Foams for Environmental Applications

Md Musfiqur Rahman
University of Maine, md.musfiqur.rahman@maine.edu

ADVANCES IN CELLULOSE NANOMATERIAL-BASED FOAMS FOR ENVIRONMENTAL APPLICATIONS

By

Md Musfiqur Rahman

B.Sc. Shahjalal University of Science & Technology, 2017

M.Sc. Shahjalal University of Science & Technology, 2019

A DISSERTATION

Submitted in Partial Fulfillment of the

Requirements for the Degree of

Doctor of Philosophy

(in Forest Resources)

The Graduate School

The University of Maine

December 2023

Advisory Committee:

Mehdi Tajvidi, Associate Professor of Renewable Nanomaterials (Co-Advisor)

Islam Hafez, Assistant Professor of Wood Science & Engineering (Co-Advisor)

Aria Amirbahman, Professor of Civil, Environmental and Sustainable Engineering

Douglas W. Bousfield, Professor of Chemical and Biomedical Engineering

Michael D. Mason, Professor of Biomedical Engineering

ADVANCES IN CELLULOSE NANOMATERIAL-BASED FOAMS FOR ENVIRONMENTAL APPLICATIONS

By Md Musfiqur Rahman

Dissertation Advisors: Dr. Mehdi Tajvidi and Dr. Islam Hafez

An Abstract of the Dissertation Presented
in Partial Fulfillment of the Requirements for the
Degree of Doctor of Philosophy
(in Forest Resources)
December 2023

The use of metal-oxide nanoparticles adsorbents is limited to fixed-bed columns in industrial-scale water treatment applications. This limitation is commonly attributed to the tendency of nanoparticles to aggregate, the use of non-sustainable and inefficient polymeric resins as supporting materials, or a lack of adsorption capacity. Foams and aerogels derived from cellulose nanomaterials have unique characteristics, such as high porosity and low density, which enables their use in a variety of environmental applications, including water treatment. However, the overall use of cellulose nanomaterial-based foams in various environmental sectors is limited due to the high cost of production associated with time- and cost-intensive manufacturing processes such as freeze-drying and supercritical CO_2 drying. In addition, additive manufacturing is a prominent technology for accurately developing and controlling micro-to-macrostructures with continuous automation; however, the use of cellulose-based materials in additive manufacturing is also limited due to its complex processing route involved in different stages of manufacturing. Hence this dissertation initially assessed the feasibility of the synthesis and immobilization of magnesium-doped amorphous iron oxide nanoparticles (IONPs) on the surface of a freeze-dried and crosslinked cellulose nanofibril (CNF) aerogel for arsenic removal from water. The adsorption kinetics and isotherms were studied for both As(III) and As(V).

Further work involved the use of urea as an additive to develop a microwave-assisted thawing procedure for creating CNF-based hybrid foams at a significantly shorter time and lower energy consumption than any previously reported methods. A freezing rate-dependent mechanism for foam formation was proposed, along with a new crosslinking pathway that was confirmed by FTIR and nitrogen content analyses. The foams' mechanical properties were examined in both dry and wet conditions. In addition, the dissertation provides with an investigation for the 3D-printability of a CNF paste by optimizing the solid content of CNFs with the composition of urea and carboxymethyl cellulose (CMC). The amplitude-sweep tests and zeta potential analyses demonstrated conclusively that the rheological properties of the paste are significantly influenced by the addition of urea and CMC at various concentrations. Compression and tensile strengths were evaluated, and it was discovered that a higher CMC content positively affected interlayer adhesion along the printing direction, thereby increasing the compression and tensile strengths of the structures. Using the Fourier-transform infrared spectroscopy (FTIR), a comprehensive investigation of the chemical interactions between CNF, urea, and CMC was conducted. Consequently, this method provides an economically viable alternative for promoting sustainable nanomaterials in the field of additive manufacturing, thereby creating new opportunities for increasing production scale and efficiency.

DEDICATION

To my parents (Mostafizur Rahman and Nafiza Begum) for their lifelong struggle to raise and guide me against all odds and teaching me the way of life and humanity.

ACKNOWLEDGEMENTS

I would like to thank my great advisors, Dr. Mehdi Tajvidi and Dr. Islam Hafez for their constant guidance and support throughout my entire PhD. I believe the best part of my PhD tenure to get the opportunity to work at Laboratory of Renewable Nanomaterials (LRN) where I have not only developed the ability to solve fundamental problems but have also been granted the liberty to explore my interests.

I would like to acknowledge my committee member Dr. Aria Amirbahman for guiding me from the beginning of my PhD. Special thanks for his insightful suggestions on the arsenic adsorption experiments.

I also would like to thank my committee members Dr. Douglas W. Bousfield and Dr. Michael D. Mason for their insightful suggestions and for granting me access to their lab spaces when needed. Also, I would like to thank Dr. Ling Li for providing me with access to her lab and offering me all the guidance and advice.

I also would like to thank our funding agencies: United States Department of Agriculture (USDA) Forest Services, USDA National Institute of Food and Agriculture, McIntire-Stennis, and The University of Maine.

My heartfelt gratitude to all my present and previous lab members (Md Ikramul Hasan, Rakibul Hossain, Nabanita Das, Alexander Collins, and Dr. Wenjing Sun) at Laboratory of Renewable Nanomaterials (LRN) for providing me their help and support. I gratefully acknowledge Advanced Structures and Composites Center (ASCC), Process Development Center (PDC), Forest Bioproducts Research Institute (FBRI), Frontier Institute for Research in Sensor Technologies (FIRST), Dr. Emma Perry (UMaine Microscopy Laboratory Manager), Dr. Brian G. Frederick (Department of Chemistry), Michael Handley (Climate Change Institute), Dr. Siamak Es-haghi (ASCC) and others who have kindly helped me throughout my doctoral research.

I acknowledge all my friends and well-wishers at University of Maine especially Mohammed Abdul Baten, Kallol Barai, Diprajit Biswas, Dr. Muhammad Radowan Hossen, Dr. Sabrina Sultana, and Adeeb Ibne Alam for their enormous support when I needed.

I also want to thank the Office of International Programs (OIP), especially Mireille Le Gal and Sarah Joughin for their great help and advice during these years.

At last, I am undoubtedly grateful to my brother Minhazur Rahman and my uncle Md Monir Uddin for supporting me with their help, motivation, and encouragement all these years.

TABLE OF CONTENTS

LIST OF TABLES

LIST OF FIGURES

CHAPTER 1

INTRODUCTION

1.1 Research motivation

Plastic and synthetic polymers began to be perceived as a curse in the 20th century, whereas they were regarded as a boon a century earlier. This is since they are non-biodegradable, causing disruption to the natural ecosystem and infiltration of the food chain. Cellulose, the most abundant natural polymer, is considered a potentially viable alternative for synthetic polymers in this context. Cellulose is being explored as a potential substitute for synthetic plastics and polymers in a variety of industrial fields, including food packaging, reinforced composites, construction, energy storage, and environmental applications including gas and liquid filtration. There are various types of cellulose nanomaterials, with cellulose nanofibrils (CNFs) and cellulose nanocrystals (CNCs) being the most prevalent. Among these, CNFs are the most economically viable cellulose nanomaterials. Foams and aerogels derived from CNFs are low-density porous structures with vast potential for a variety of applications, including support material for nanoparticles in filtration applications and hybrid membranes. The potential for economically viable production of cellulose nanofibrils (CNFs) as a porous support material could facilitate the uniform dispersion of nanoparticles across the surface of CNF, thereby preventing substantial aggregation. However, freeze-drying, and supercritical CO_2 drying are most used techniques for producing CNF-based foams and aerogels. Although those techniques are effective in terms of producing high quality CNF foam/aerogels, the energy cost and time associated with these techniques are high preventing these sustainable foams to be adopted by the industries instead of synthetic polymer-based foams. Hence, the search for alternative CNF-foam manufacturing techniques is a research area that needs attention. In addition, porous CNF structures have diverse application facilitated with the aid of 3D printing or additive manufacturing which involves with making complex geometric design. With the aid of 3D printing, the higher structural control could be achieved than the conventional molded structures. However, the limited use of CNF in

3D printing process over other polymers is due to the complex processing through chemical modifications for achieving printability followed by high energy and time consumption for drying the structures. Therefore, new CNF-based 3D printing technique needs to be developed with minimal effort for both printability and post processing.

All those notions have served as a motivation for our exploration, investigation, and design of innovative CNF-based porous systems that hold promise for implementation in water filtration and a myriad of other environmental uses.

1.2 Research questions

Over the next chapters, we will seek answers to the following questions:

- ◊ Is it possible to immobilize iron-oxide nanoparticles on CNF aerogel without sacrificing nanoscale particle dimension and minimizing agglomeration? How does it perform towards arsenic adsorption from water?
- ◊ Is it possible to manufacture low-density molded hybrid CNF foams without conventional freeze-drying or supercritical CO_2 drying? Is it possible to use microwave irradiation for CNF foam forming? How do the foams prepared via microwave drying compare to freeze dried foams and what are the governing factors of the microwave process?
- ◊ Is there any potential way to extend and apply the cost-efficient CNF-foam manufacturing technique towards the 3D printing application? What are the factors that affect the 3D printability of CNF paste?

1.3 Research goal and objectives

The comprehensive goal of this dissertation was to explore and examine innovative pathways to produce CNF-based foams and to determine their effectiveness in environmental applications such as water treatment.

The objectives for each chapter are as follows.

CHAPTER 2. HIGHLY EFFICIENT IRON-OXIDE NANOPARTICLES IMMOBILIZED ON CELLULOSE NANOFIBRILS AEROGELS FOR ARSENIC REMOVAL FROM WATER.

- Synthesize Mg-doped iron-oxide nanoparticles (IONPs) with coprecipitation and solvent-thermal synthesis method.
- Develop a hassle-free method to immobilize the nanoparticles into the CNF surface freeze-drying and use Polycup^{TM} resin for crosslinking CNF for wet stability.
- Understand the role of CNFs in the homogeneous distribution of IONPs and study the chemical interactions between CNF and IONPs and crosslinking reaction.
- Study arsenic adsorption kinetics and isotherms and predict the maximum adsorption capacity of CNF-IONPs towards both arsenic (III) and (V) adsorption from water also optimize the CNF:IONPs ratio for highest adsorption efficiency.

Chapter 3. FUNDAMENTALS OF HYBRID CELLULOSE NANOFIBRIL FOAM PRODUCTION BY MICROWAVE-ASSISTED THAWING/DRYING MECHANISM.

- Assess the optimum content of urea as an additive with CNF suspension for foam forming microwave irradiation of a pre-frozen suspension.
- Understand the effect of freezing rate towards foam density and internal pore morphology and establish a foam forming mechanism.
- Study the effect of thawing time and comparison among freeze-drying, convection and microwave drying towards foams' density, shrinkage, and mechanical properties.
- Investigate possible chemical interactions/crosslinking reaction between urea and CNF and assess the feasibility of producing nanoparticles immobilized CNF-foams.

Chapter 4. 3D PRINTING OF CELLULOSE NANOFIBRILS ENABLED BY MICROWAVE TECHNOLOGY.

- Use carboxymethyl cellulose (CMC) and urea as additives for CNF-based pastes and optimize the overall paste solid content for multilayer 3D printed structures.
- Understand the effect of variable level of CMC and urea towards the paste rheology.
- Optimization of 3D printing parameters and evaluate the structural shrinkage and volumetric accuracy with different paste formulations upon microwave drying.

- Investigate the compressive and tensile properties of the 3D printed structures to understand the role of CMC and urea content on overall mechanical properties.

1.4 Dissertation outline

This dissertation consists of five chapters. The present chapter (**Chapter 1)** or the introductory chapter to provide research motivation, questions, goal, objectives, and dissertation outline.

In **chapter 2**, Mg-doped iron oxide nanoparticles (IONPs) were synthesized and immobilized into crosslinked CNF aerogels (CNF-IONPs) through freeze-drying. It was observed that the CNFs can efficiently restrict the nanoparticles to agglomerate which retains their nanoscale dimension with high specific surface area. The arsenic adsorption behavior of CNF-IONP adsorbents were evaluated through adsorption kinetics and isotherm modelling. The chemical interactions between CNF and IONPs were studied and the ratio of CNF to IONPs were evaluated for maximum adsorption efficiency.

However, the freeze-drying technique is time and energy-consuming which is a great barrier CNF-based foam manufacturing. To address this issue, a novel manufacturing pathway for hybrid CNF foams was developed in **chapter 3** using urea as additive with energy efficient rapid microwave irradiation. The new mechanism of CNF-foam forming was proposed. Additionally, effect of the rate of freezing and thawing time was studied for efficient foam preparation. The possible heat induced in-situ crosslinking reaction was proposed due to fact of the foam's wet stability. The chemical and mechanical properties were comprehensively studied and compared with freeze-dried foams of similar density for a meaningful comparison.

Following the successful development of molded foam by microwave irradiation in **chapter 3**, the similar concept was modified and successfully used in **chapter 4,** to address both the processing and manufacturing challenges in CNF-based additive manufacturing/3D printing. Using carboxymethyl cellulose (CMC), urea and CNF; the 3D printing pastes were formulated for multilayer structures. The paste rheology was studied, and structural accuracy and shrinkage

were evaluated. The chemical and mechanical properties were also studied for the microwave dried structures with different paste formulations.

Finally, **chapter 5** presents the conclusions and future work.

CHAPTER 2

HIGHLY EFFICIENT IRON-OXIDE NANOPARTICLES IMMOBILIZED ON CELLULOSE NANOFIBRILS AEROGELS FOR ARSENIC REMOVAL FROM WATER

2.1 Chapter Summary

The application and optimal operation of nanoparticle adsorbents in fixed-bed columns or industrial-scale water treatment applications are limited. This limitation is generally due to the tendency of nanoparticles to aggregate, the use of non-sustainable and inefficient polymeric resins as supporting materials in fixed-bed columns, or low adsorption capacity. In this study, magnesium-doped amorphous iron oxide nanoparticles (IONP) were synthesized and immobilized on the surface of cellulose nanofibrils (CNF) within a lightweight porous aerogel for arsenic removal from water. The IONP had a specific surface area of 165 m^2 g^{-1}. The IONP-containing CNF aerogels were stable in water and under constant agitation due to the induced cross-linking using an epichlorohydrin cross-linker. The adsorption kinetics showed that both As(III) and As(V) adsorption followed a pseudo second-order kinetic model, and the equilibrium adsorption isotherm was best fitted using the Langmuir model. The maximum adsorption capacities of CNF-IONP aerogel for As(III) and As(V) were 48 and 91 mg As g-$IONP^{-1}$, respectively. The optimum IONP concentration in the aerogel was 12.5 wt.% which resulted in a maximum arsenic removal, minimal mass loss, and minimal leaching of iron into water.

2.2 Introduction

Arsenic is one of the most toxic elements that can be found in groundwater at high concentrations in many locations across the globe (Shankar et al., 2014). Long-term exposure to arsenic from drinking water is associated with health issues such as cancers, skin lesions, and cardiovascular diseases (Ratnaike, 2003). Arsenic is a metalloid that has two major oxidation states at the ambient environment: arsenite, As(III), and arsenate, As(V). According to the United States Environmental Protection Agency (US-EPA), the maximum contaminant level (MCL) for arsenic in drinking water is 10 μg L^{-1}.

Arsenic can be removed from water by techniques such as reverse osmosis, oxidation, ion exchange, and coagulation-flocculation (Nicomel et al., 2015). These technologies are efficient but are often costly and are based on non-sustainable materials. Adsorption-based techniques have the potential to effectively treat drinking water if an appropriate and efficient adsorbent is developed (Hao et al., 2018). A number of studies have focused on the development of cost-effective and sustainable adsorbents for arsenic removal (Mohan & Pittman, 2007). Iron oxide-based nanoparticles typically have a high affinity towards arsenic. Crystalline iron oxide nanoparticles such as hematite (α-Fe_2O_3), magnetite (Fe_3O_4), or maghemite (γ-Fe_2O_3) have relatively low specific surface areas (<100 m^2 g^{-1}) (Hao et al., 2018; Macera et al., 2020). Amorphous iron oxide nanoparticles (IONP) tend to have a higher surface area than crystalline nanoparticles; however, their transitions to other crystalline phases over time limits their application (Das et al., 2011; Liao et al., 2001; Phu et al., 2011). Doping IONP with another metal ion could inhibit its phase transition and retain its amorphous nature, hence maintaining the increased surface area (Baltpurvins et al., 1997; Iacob et al., 2015; Phu et al., 2011). Another common challenge with using IONP is their tendency to aggregate, which results in a decrease in its specific surface area (Bushell et al., 2020). This means that the application and optimal operation of nanoparticle adsorbents in fixed-bed columns or industrial scale would be limited. Researchers have attempted to utilize nanoparticulate aggregates in fixed-bed columns (Casentini et al., 2019; Ghosh et al., 2014; Hu et al., 2015). In these attempts, the adsorption capacity was often sacrificed because of the increased extent of aggregation.

Cellulose nanomaterials have emerged as promising materials in environmental applications. Cellulose is a linear polysaccharide composed of glucose units connected through β 1–4 glycosidic bonds (Moon et al., 2011). Cellulose nanofibrils (CNF) is a highly entangled form of nanocellulose generally produced by mechanical refining or other mechanical size reduction methods such as microfluidization, homogenization, or grinding (Yi et al., 2020). The diameter of the fibrils is typically 5–50 nm, and the fibrils can be several μm in length (Moon et al., 2011).

A large number of scientific reports have been published to prove the concept of nano-cellulose-based materials for a variety of water and wastewater treatment processes, including the removal of toxic heavy metals and dyes (Voisin et al., 2017). The ongoing research on nanocellulose-based materials for sustainable water treatment has largely focused on the development of chemically functionalized materials such as TEMPO (2,2,6,6-tetramethylpiperidine-1-oxyl)-oxidized, carboxylated, sulfonated, phosphorylated, and amino-functionalized nanocellulose to enhance the adsorption capacity (Mohammed et al., 2018). The functionalization route remains a challenging task due to the complexity of the process and the low adsorption capacity.

Immobilizing the IONP on the surface of cellulose fibrils could be a promising solution to tackle the two challenges mentioned above: nanoparticle aggregation and their limited application in fixed-bed columns. CNF has the potential to decrease the extent of IONP aggregation owing to its stable aqueous suspension and nanoscale dimensions. In such a case, drying a stable suspension of CNF and IONP into a foam or aerogel structure could result in uniformly distributed IONP within the CNF network with minimal aggregation. A few attempts have been made to incorporate iron oxide nanoparticles into CNF porous structures (Dong et al., 2020; Yu, 2013). Although the incorporation of the nano-entities has been successful, several issues have been identified. First, the studies lacked adequate characterization of adsorbent stability under wet conditions, which is essential given their intended application in water treatment. Second, information relative to the stability of the nanoparticles within the cellulose structures remains to be elucidated. Third, a favorable adsorption capacity was obtained by incorporating a high load of iron oxide nanoparticles within the aerogel (36%) without investigating the structural stability of the adsorbents in water (Yu et al., 2013).

In the present work, a novel protocol to produce porous CNF structures loaded with uniformly distributed IONP with minimal aggregation and considerably high specific surface area was studied. The IONP were immobilized on CNF, and the adsorbents were tested for their

adsorption performance towards As(III) and As(V). In addition, extensive physical and chemical characterizations of the CNF-IONP aerogels were conducted, as well as an assessment of their stability under various IONP loadings.

2.3 Experimental section

2.3.1 Materials

CNF was provided by the Process Development Center (PDC) of the University of Maine. The 3 wt.% CNF was produced by mechanically refining bleached softwood Kraft pulp. This is the standard grade of CNF produced by the PDC and contains 90% fines. In this context, the fines content indicates the percentage of fibers with lengths < 200 μm. Polycup™ (polyamide-epichlorohydrin) 5150 cross-linker (26 wt.%) was supplied by Solenis (Wilmington, DE). Anhydrous ferric chloride ($FeCl_3$; 98%) and magnesium chloride ($MgCl_2$; 99%) were purchased from Alfa Aeser (Haverhill, MA). Anhydrous ethyl alcohol (C_2H_5OH; 99.5%) was obtained from Acros Organics (Jair Lawn, NJ). HEPES (4-(2-hydroxyethyl)-1-piperazineethanesulfonic acid) buffering agent (≥ 99.5%), sodium chloride (NaCl; ≥99%), sodium hydroxide (NaOH; ≥ 97%), hydrochloric acid (HCl; 37%), sodium (meta) arsenite ($NaAsO_2$), and sodium arsenate dibasic heptahydrate ($Na_2HAsO_4.7H_2O$; ≥98%) were purchased from Sigma-Aldrich (St. Louis, MO). All chemicals and solvents were used without any further purification.

2.3.2 Synthesis of Mg-doped amorphous IONP

To synthesize the Mg-doped amorphous IONP, 0.09 M $FeCl_3$ and 0.01 M $MgCl_2$ solutions were prepared by dissolving 1.02 g $FeCl_3$ and 0.066 g $MgCl_2$ salts together in 70 mL of ethanol (Tang et al., 2013). A 20 mL 2.3 M ethanolic NaOH solution was prepared by dissolving 1.84 g solid NaOH. Ten mL of 2.3 M ethanolic NaOH solution was added to the salt mixture which results in a red yellowish precipitate of the amorphous Mg-doped ferric hydroxide, $(Fe, Mg)_x(OH)_y$. The solution was continuously ultrasonicated by a Branson 450 sonicator (VWR Scientific, Radnor, PA) for 1 h to break up the aggregates. The reaction mixture was then transferred to a 100 mL Teflon-lined autoclave container and placed in a preheated oven at 150 °C for 2 h. During the

heating process, simultaneous nucleation and homogeneous heating further decreased the particle size (Phu et al., 2011). Subsequently, the autoclave was cooled to room temperature. The IONP suspension was washed with distilled water 2–3 times using a centrifuge to remove ethanol and other dissolved components until pH 7.0 was reached. Finally, the volume of the IONP suspension was adjusted to 50 mL by adding distilled water, and the suspension was stored at 2-5°C.

2.3.3 Preparation of CNF-IONP adsorbent

Initially, a batch of 1 wt.% CNF suspension was mixed with Polycup^{TM} cross-linker (5 wt.% of the total dry mass of CNF) and stirred with a magnetic stirrer at 300 rpm for 5 min to ensure a homogeneous distribution of the cross-linker. CNF aerogels containing IONP content of 12.5 wt.% were prepared by mixing IONP and CNF suspensions according to the amounts listed in Table A1. The suspension mixture was mechanically stirred with a magnetic stirrer at 300 rpm followed by a continuous ultrasonication for 5 min. Finally, the CNF-IONP suspension mixture was poured into a cylindrical plastic mold (height: 2.5 cm and diameter: 1.3 cm) and freeze-dried using a freeze-dryer (Harvest Right, North Salt Lake, UT). The temperature cycles of the freeze dryer were -34.4, -6.7, 4.4, 15.6, and 32.2 °C for 8, 10, 8, 3, and 3 h, respectively. A schematic illustration that describes the synthesis process is presented in Figure A1. After freeze-drying, the CNF-IONP aerogel adsorbents were heated in a vacuum oven (25 mm Hg = 86 kPa) at 105 ± 2 °C to induce cross-linking. The proposed reaction mechanism is presented in Figure A2.

2.3.4 Characterization

A Panalytical X'Pert PRO X-ray diffractometer (Royston, UK) was used to assess the nature of the nanoparticles and the crystalline structure of the CNF aerogels. The XRD anode material was Cu with Kα at a wavelength of 1.54 nm. The generator voltage and current were 40 kV and 40 mA, respectively. The scan step size and 2θ range were 0.05° sec^{-1} and 10–80°, respectively. The baseline correction, smoothing and background subtraction for the XRD data were performed using Origin Pro 2021 software.

The surface morphology of CNF aerogels before and after IONP immobilization was assessed by a Zeiss Nvision 40 scanning electron microscope (SEM; Oberkochen, Germany). The aerogel samples of a thickness of 2–4 mm were prepared by slicing through the middle section using a sharp blade. Prior to imaging, all the samples were sputter-coated by a thin layer of gold-palladium and scanned at an accelerating voltage of 3 kV.

Energy-dispersive X-ray spectroscopy (EDS; iXRF model 550i AMRay 1820, Bedford, MA) was used for the elemental mapping of Fe, Mg, C, and O atoms at the CNF-IONP surface. An accelerating voltage of 20 kV was maintained for the EDS analysis.

The specific surface areas (SSA) of freeze-dried CNF aerogel and IONP samples were measured by the BET (Brunauer, Emmett and Teller) nitrogen adsorption method using an ASAP 2020 instrument (Micromeritics; Norcross, GA). The CNF aerogel and IONP samples were degassed in a vacuum for 5 h at 75 °C and 130 °C, respectively.

The ATR-FTIR analysis was performed using a PerkinElmer Spectrum Two™ FT-IR spectrophotometer (Shelton, CT) to evaluate the nature of the interaction between the CNF and IONP in the aerogel. The data obtained for CNF and CNF-IONP aerogels were normalized with respect to the wavenumber 1055 cm^{-1}, which represents the stretching vibration of the cellulose backbone (not altered by the cross-linking reaction).

A Nano ZS90 Zetasizer (Malvern, UK) was used to measure the zeta potentials of CNF and IONP in water. The isoelectric points (IEP) were determined by measuring the zeta potentials at pH 3–11. Relatively low concentrations (~0.1 wt.%) of CNF and IONP suspensions were used with a constant ionic strength of 0.01 M NaCl for all the zeta potential measurements.

The density (ρ, g cm^{-3}) and porosity (%) of the aerogels were calculated by measuring the void volume ($v1$) by an Accupyc II gas pycnometry system (Norcross, GA), the total volume ($v2$) using a digital caliper, and corresponding mass (m) according to Equations 2.1 and 2.2, respectively.

Density of the aerogel, $\rho = \frac{m}{v2}$ (2.1)

Porosity (%) = $(1-\frac{v1}{v2}) \times 100$ (2.2)

The shape recovery tests were conducted by compressing the aerogels at a pressure of 1.2 kPa using a Dake® manual hydraulic pump. The aerogel was compressed into a 5 mm thin disk and submerged in 80 mL distilled water for 10 sec. The aerogel heights before compression (h_i) and after submerging in water (h_f) were recorded. The shape recovery was calculated using Equation 2.3.

Shape recovery (%) = $\frac{h_f}{h_i} \times 100$ (2.3)

The water absorption capacity of the aerogels was determined by calculating the mass differences of aerogels before (w_i) and after (w_f) soaking in 80 mL distilled water for 12 h according to Equation 2.4.

Water absorption capacity (g-water g-dry mass^{-1}) = $\frac{(W_f - W_i)}{W_i}$ (2.4)

The mass losses of the CNF and CNF-IONP aerogels were determined gravimetrically after submerging the aerogels into 80 mL distilled water for 12 h with constant agitation and drying in an oven at 75°C for 5 h. The % of mass loss was calculated by comparing the initial (m_1) and after drying (m_2) dry mass according to Equation 2.5.

Mass loss (%) = $(\frac{m_1 - m_2}{m_1}) \times 100$ (2.5)

2.3.5 Arsenic adsorption experiments

All batch arsenic adsorption experiments were carried out in 100 mL Falcon tubes filled up to 80 mL at room temperature (~25°C) under constant agitation (VWR Scientific Products rocking platform model 100, Radnor, PA). For the kinetic experiments, 3 mL of solution were removed at specific time intervals. Samples were acidified immediately after collection by 1% v/v of concentrated HNO_3, and the arsenic and iron concentrations were measured by a Thermo Scientific™ Element 2™ ICP-MS (Waltham, MA) calibrated using SLRS-6, a river certified

reference material from National Research Council of Canada. The initial arsenic concentration for adsorption kinetic studies was ~300 μg L^{-1} for both As(III) and As(V). For the kinetic experiments involving both As species, the initial IONP concentrations were 16, 31, and 63 mg L^{-1}. Samples were collected for analysis at different time intervals up to 12 h. For the equilibrium adsorption experiments, the initial arsenic concentration ranged from 0.055 to 15.89 mg L^{-1} for As(III), and 0.073 to 21.65 mg L^{-1} for As(V). All arsenic solutions were prepared in a 0.01 M HEPES buffer with 0.05 M NaCl. The pH remained constant at 7.0–7.2 throughout all experiments. A set of equilibrium adsorption experiments were conducted at different pH values and at an initial As(V) and As(III) concentration of 1 mg L^{-1} with a dosage of 63 mg of IONP L^{-1}. The role of IONP concentration in the CNF-IONP aerogel was investigated by varying the wt.% of IONP between 1 and 30% and adjusting the CNF concentration accordingly. A concentration of 7.2 mg L^{-1} of As(V) solution was used to perform the analysis with 12 h of contact time under constant agitation.

2.4 Results and discussion

2.4.1 Arsenic adsorption experiments

Figure 2.1 shows the adsorption kinetics of As(III) and As(V) for three CNF-IONP sorbent concentrations. Given that CNF alone did not remove significant As(III) and As(V) concentrations, the reported sorbent dosages are those of IONP. As(III) and As(V) concentrations decreased rapidly in the first 1-2 h depending on the sorbent dosage due to the increased number of available IONP surface sites. For both arsenic species, near-equilibrium adsorption was reached within ~3 h. IONP dosages of 63 mg L^{-1} resulted in the removal of As(III) and As(V) to <10 μg L^{-1} after 12 h of contact time.

The adsorption kinetic data were best represented using a pseudo second-order rate equation,

$$\frac{t}{q_t} = \frac{t}{q_e} + \frac{1}{K_{ad}\, q_e^2} \tag{2.6}$$

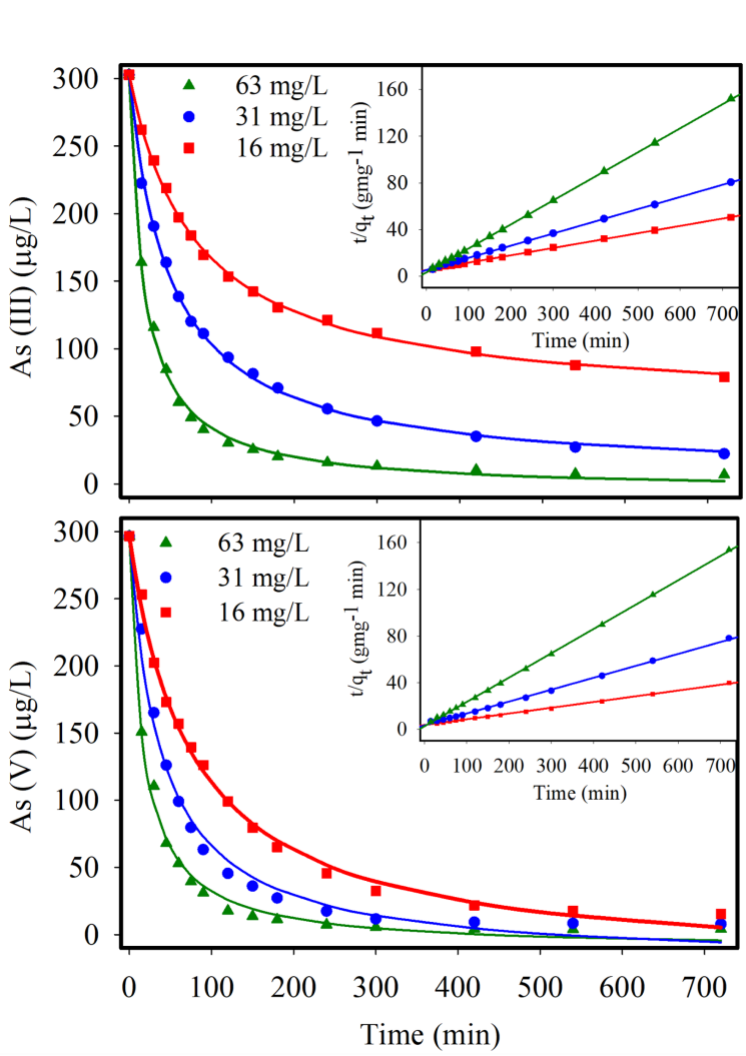

Figure 2.1. As (III) and As (V) adsorption kinetics with three different IONP loadings within CNF aerogel. The reported dosages are the IONP concentrations. The fitted aqueous arsenic concentrations were determined from the difference between the initial and adsorbed arsenic concentrations. The inset graphs are the pseudo second-order kinetic fits for the corresponding dosage of adsorbent according to Equation 2.6.

where q_e and q_t are the adsorbed arsenic (mg-As g-IONP^{-1}) at equilibrium and at time t, respectively, and K_{ad} is the pseudo second-order rate constant (g-IONP mg-As.min^{-1}). The K_{ad} values for As(III) and As(V) uptake increased with increasing the adsorbent dosage (Table 2.1), indicating a faster uptake rate with a higher adsorbent concentration.

Table 2.1. Summary of kinetic parameters for As(III) and As(V) adsorption on IONP in CNF-IONP aerogel.

Adsorption parameters	As(III)			As(V)		
Initial As Concentration (mg-As L^{-1})	0.0296			0.0302		
Adsorbent Loading (mg-IONP L-As^{-1})	16	31	63	16	31	63
q_e (mg-As g-$IONP^{-1}$)	15.87	9.57	4.85	20.41	9.78	4.78
K_{ad} (g-IONP mg-As·min^{-1})	7.6×10^{-4}	2.1×10^{-3}	1.35×10^{-2}	6.7×10^{-4}	3.2×10^{-3}	1.67×10^{-2}
r^2	0.99	0.99	0.99	0.99	0.99	0.99

The equilibrium adsorption of As(III) and As(V) onto CNF-IONP aerogels at pH 7 was investigated (Figure 2.2). Experimental data for both arsenic species were well represented by the Langmuir isotherm model (Equation 2.7), which is applicable to a monolayer ad-sorption behavior assuming a uniform surface adsorption energy (Stumm & Morgan, 2012).

$$q_e = \frac{q_{max} K_L C_e}{1 + K_L C_e} \tag{2.7}$$

where q_e is the mass of As(III) or As(V) adsorbed at equilibrium per mass of IONP (mg-As g-$IONP^{-1}$), q_{max} is the maximum adsorption capacity (mg-As g-$IONP^{-1}$), C_e is the equilibrium As(III) or As(V) concentration (mg L^{-1}) in post-adsorption water samples, and K_L is the Langmuir constant for adsorption. The maximum adsorption capacities of the CNF-IONP aerogel adsorbent were 47.75 and 90.90 mg-As g-$IONP^{-1}$ for As(III) and As(V), respectively.

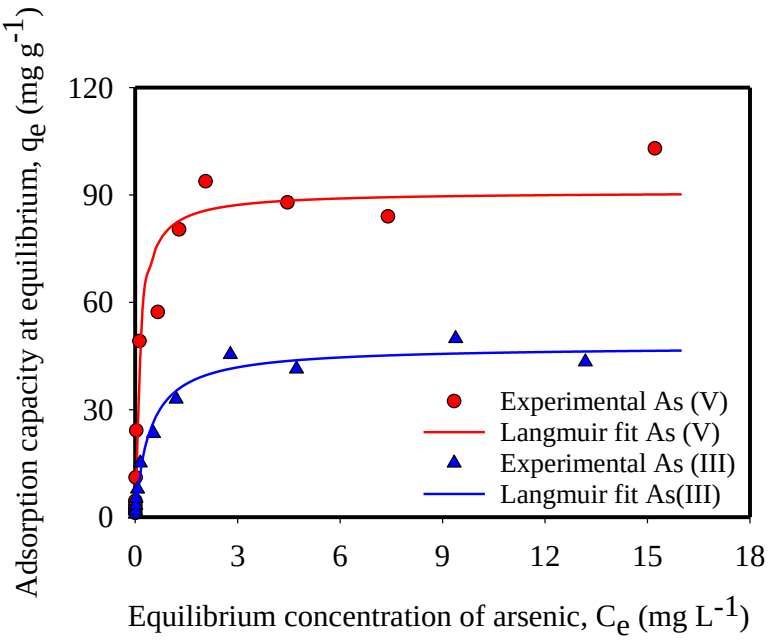

Figure 2.2. Equilibrium adsorption isotherms of As(III) and As(V). The adsorbent dosage was 63 mg of IONP L^{-1} of arsenic ion.

Table 2.2. Summary of Langmuir isotherm model fits for arsenic adsorption onto the CNF-IONP aerogel.

	As(III)	As(V)
q_{max} (mg-As g-IONP^{-1})	47.75	90.90
K_L	2.36	7.95
r^2	0.99	0.99

The constant K_L in Equation 2.7 indicates the sorption affinity of a solute toward a sorbent. Our results show that As(V) has a significantly higher affinity toward the IONP than As(III) (Table 2.2). The difference in affinity between the two arsenic species is especially evident at low aqueous arsenic concentrations that are representative of natural waters, indicating that As(III) is more mobile in the environment (Smedley & Kinniburgh, 2002). This may be attributed to the largely uncharged form of As(III) at pH 7 ($H_3AsO_3 \Leftrightarrow H^+ + H_2AsO_3^-$, pK = 9.15) compared to As(V) that is negatively charged at the same pH ($H_3AsO_4 \Leftrightarrow H^+ + H_2AsO_4^-$, pK = 2.3; $H_2AsO_4^- \Leftrightarrow H^+ + HAsO_4^{2-}$, pK = 7.16). The negatively charged As(V) species interact more favorably with the

positively charged surface of IONP, resulting in a higher adsorption affinity and capacity (Table 2.2).

Findings from previous studies shown in Table 2.3 highlight the importance of functionalizing the micro- and nano-sized cellulosic materials to result in an acceptable affinity towards arsenic. The table also shows the superior performance of our adsorbent to other iron oxide-based nanoparticles used for arsenic removal. However, comparisons with iron oxide nanoparticles incorporated in cellulosic-based structures must be interpreted with caution. Of particular interest is the work of Yu et al. and Dong et al. (Dong et al., 2020; Yu et al., 2013), whose studies investigated iron oxide-based nanoparticles in cellulosic structures. The maximum adsorption capacity obtained herein is comparable to that of Yu et al. However, it is worth noting that the Fe_2O_3 content used in their study was 36%, which is approximately three times that of the IONP content used in this study (12.5%). The maximum adsorption capacity obtained by our adsorbent is considerably higher than that obtained by Dong et al. This could be attributed to the lower iron oxide content in their work (9.4%).

Table 2.3. Arsenic adsorption capacities of cellulose- and iron oxide-based adsorbents from the literature

Adsorbent	As concentration range, C_0 (mg L^{-1})	Maximum As adsorption capacity, q_{max} (mg g^{-1})	BET surface area (m^2 g^{-1})	pH	Reference
Cellulose-g-PDMAEMA	As(III) & As(V): 0.05 – 8.9	As(III): 8.96; As(V): 27.93	-	< 10	(Tian et al., 2011)
FeOOH/CuO@WBC	As(III): 20 – 200	As(III): 76.1	-	3.5	(Liu et al., 2020)
DETA-g-DA-NCC	As(III) & As(V): 0.005 – 50	As(III): 10.56; As(V): 12.06	-	7.5	(Singh et al., 2015)

Table 2.3 continued

Functionalized CNF	As(V): 0.025 – 40	As(V): 24.9	0.16	4-8	(Najib & Christodoulatos, 2019)
Cellulose-g-GMA-b-TEPA	As(III): ~ 5 – 35; As(V): ~20 – 100	As(III): 5.71; As(V): 75.13	3.68	As(III): 7 & As(V): 5	(Yu et al., 2013)
Fe(III)-AM-PGMACell	As(V): 25 – 400	As(V): 78.8	39.9	6	(Anirudhan et al., 2011)
AM-Fe-PGDC	As(V): 10 – 400	As(V): 105.47	31.6	6	(Anirudhan et al., 2013)
Cell-N-Cu	As(V): 100–700	As(V): 98.9	-	8.4	(Yousif et al., 2016)
CNs/ Fe_2O_3 nanorod	-	As(III): 13.87, As(V): 15.71	-	7 & 3	(Dong et al., 2020)
Cellulose@Fe_2O_3 composites*	-	As(III): 64.33, As(V): 89.19	113	7	(Yu et al., 2013)
iMNP	As(V): 1- 10	As(V): 12.74	145.5	6.6	(Zeng et al., 2020)
Fe_3O_4/ AC composite	As(III): 2-120	As(III): 7.5	-	8	(Joshi et al., 2019)
OMIM	As(III) & As(V): 1-100	As(III): 67.89, As(V): 93.54	154	3	(Wen et al., 2014)
IONP@CNF-IONP aerogel*	As(III): 0.055 – 15.9; As(V): 0.073 – 21.7	As(III): 47.75; As(V): 90.90	165	7	This work

Abbreviations: Cellulose-g-PDMAEMA: Native cellulose fibers modified with poly(N,N-dimethyl aminoethyl methacrylate), FeOOH/CuO@WBC: Iron(III) oxyhydroxide/ copper oxide composite based on water bamboo cellulose, DETA-g-DA-NCC: diethylene triamine grafted dialdehyde nanocrystalline cellulose, Functionalized CNF: Cellulose nanofibrils modified with trimethylammonium chloride, Cellulose-g-GMA-b-TEPA: Glycidyl methacrylate grafted cellulose

modified with tetraethylenepentamine, Fe(III)-AM-PGMACell: Iron(III)-coordinated amino-functionalized poly(glycidyl methacrylate)-grafted cellulose, AM-Fe-PGDC: Fe(III)-coordinated amino-functionalized poly(glycidylmethacrylate)-grafted TiO_2-densified cellulose, Cell-N-Cu: Copper containing modified cellulose, CNs/ Fe_2O_3 nanorod: Cellulose nanocrystals/ iron oxide nanorod composite, Cellulose@Fe_2O_3 composites: Composite material containing magnetic Fe_2O_3 and cellulose iMNP: Magnetic nanoparticles prepared from iron containing sludge, Fe_3O_4/ AC composite$_3$: Iron oxide/ commercial activated carbon composite, OMIM: Mesoporous iron manganese bimetal oxides.

Note: the maximum adsorption capacities are based on the total mass of adsorbent except those with an asterisk which are based on the iron oxide only.

The pH-dependent dissolved arsenic speciation affects its adsorption behavior. Figure 2.3A shows that a high removal rate (> 93%) was achieved for both arsenic species within an acidic to neutral pH (3-7), but drastically dropped after pH 7. Given the circumneutral pH of drinking water, it can be expected that the CNF-IONP adsorbent can be used effectively to remove arsenic. Figure 2.3B shows the measured zeta potentials of CNF and IONP. CNF surface is negatively-charged within the pH range 3–11 due to the presence of carboxylate groups on the surface of CNF (Liu et al., 2014). The IONP, however, has a low isoelectric point (IEP) of 4.6 compared to the 7–9 range reported for synthetic iron oxides (Parks, 1965). This is due to the positive charge deficit brought about by the presence of divalent Mg^{2+} ions in the iron oxide structure (Mohapatra et al., 2012). The pH-dependent adsorption of arsenic species onto the IONP may be explained by the opposite electrostatic charges between arsenic and the IONP surface at low pH values that favor adsorption (Farrell & Chaudhary, 2013), and electrostatic repulsion between the deprotonated surface groups of IONP and the anionic arsenic species at higher pH values that result in diminished adsorption (Mondal et al., 2007).

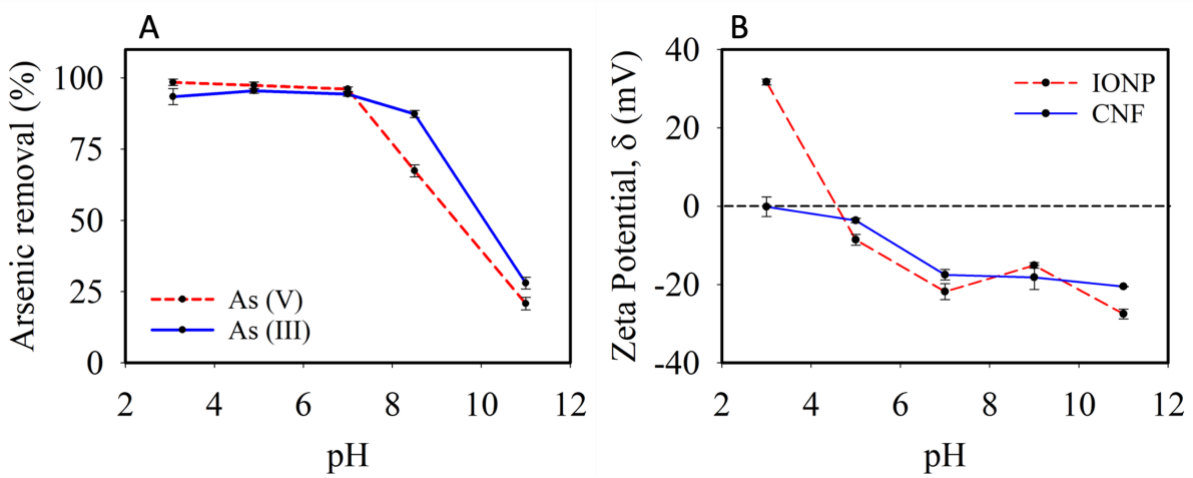

Figure 2.3. Effect of pH on arsenic removal percentage. Initial arsenic ion concentration: 1 mg L^{-1}, IONP dosage: 63 mg of IONP L^{-1} (A); and Zeta potential measurements of CNF and IONP suspensions at different pH values (B). Error bars represent standard deviation from triplet measurements.

The experiments to determine the effect of the IONP loading in the aerogel on adsorption were conducted using As(V). Figure 2.4A shows that the percent of arsenic removal was enhanced with the increase of IONP up to 12.5 wt.%, above which, increasing the IONP concentration resulted in a decrease in arsenic removal. Note that the results presented earlier were obtained with 12.5 wt.% IONP. A one-way ANOVA statistical test showed differences among the five groups of different IONP concentrations in CNF-IONP aerogel. Post hoc analysis indicated that the 12.5 wt.% sample exhibited maximum arsenic removal. The decrease in arsenic removal with an increase in IONP loading may be hypothesized that higher IONP loadings would result in densely packed IONP particles in the aerogel resulting in a decreased surface area for adsorption. High-resolution SEM images for CNF-IONP aerogels at 12.5 and 25 wt.% IONP loadings (Figure 2.4B,C) show that an increasing IONP concentration can lead to particle aggregation at the surface. A similar observation was reported in a study where increasing the magnetite concentration beyond a threshold value resulted in a decrease in Cr(VI) adsorption, and the observation was attributed to the aggregation of nanoparticles and the reduction in the availability of active adsorption sites (Padmavathy et al., 2016).

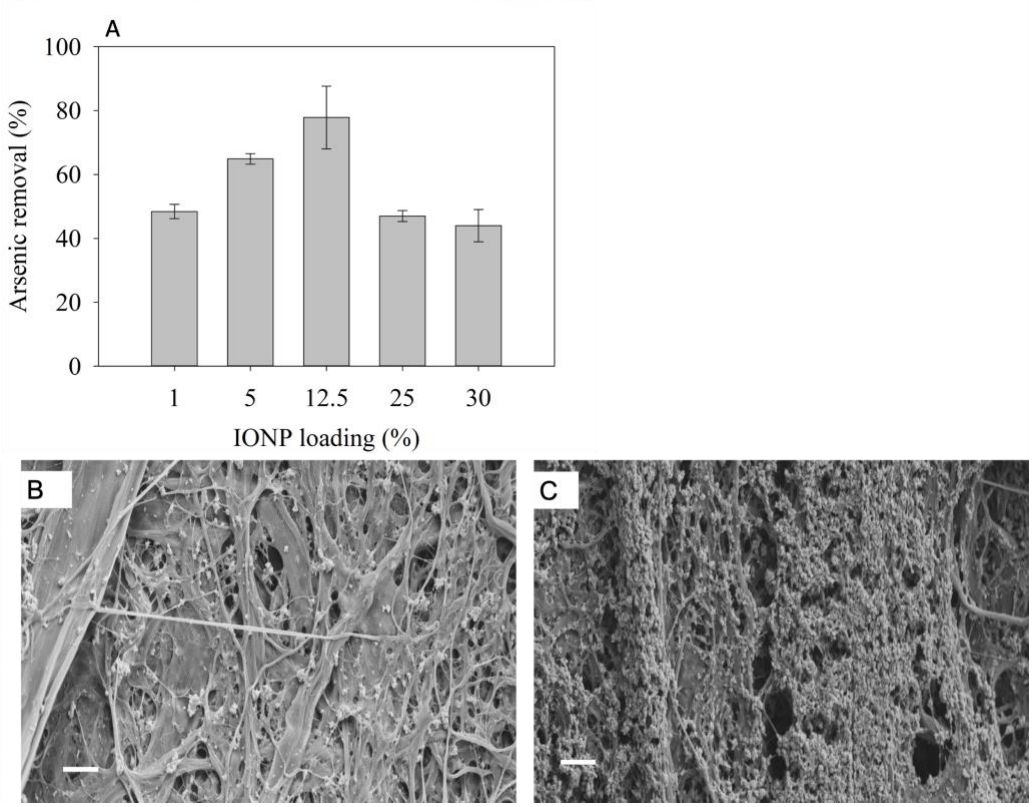

Figure 2.4. As(V) adsorption with different wt.% of IONP in CNF-IONP aerogel. The error bars represent standard deviation from triplet measurements (A); SEM micrographs (scale bar: 1 μm) of 12.5 wt.% (B) and 25 wt.% (C) of IONP in CNF-IONP aerogel.

The stability of IONP in the aerogel was investigated through the measurement of leached iron upon soaking the aerogels in water under constant agitation. For the 12.5 wt.% IONP in the CNF-IONP aerogel, an insignificant amount (<10 μg L^{-1}) of iron was leached at pH 7, which is below the WHO and US-EPA MCL of 300 μg L^{-1} for iron concentration in drinking water.

2.4.2 Characterization of the adsorbent

Figure 2.5 shows the XRD patterns for freeze-dried IONP, CNF-IONP and CNF aerogels. The XRD pattern of freeze-dried IONP showed no peaks, indicating the amorphous nature of the nanoparticles. The XRD peaks of both CNF and CNF-IONP aerogels were similar. The broad peak between 15° and 16.5° corresponds to Miller indices (1-10) and (110), respectively, and the sharp peak around 22.5° corresponds to the lattice diffraction of (200) plane (French, 2014). The low-intensity peak around 35° corresponds to the plane (004) of cellulose I (Hafez et al., 2020). A

noticeable decrease was observed in peak intensities for cellulose in CNF-IONP aerogel resulting from the incorporation of the IONP.

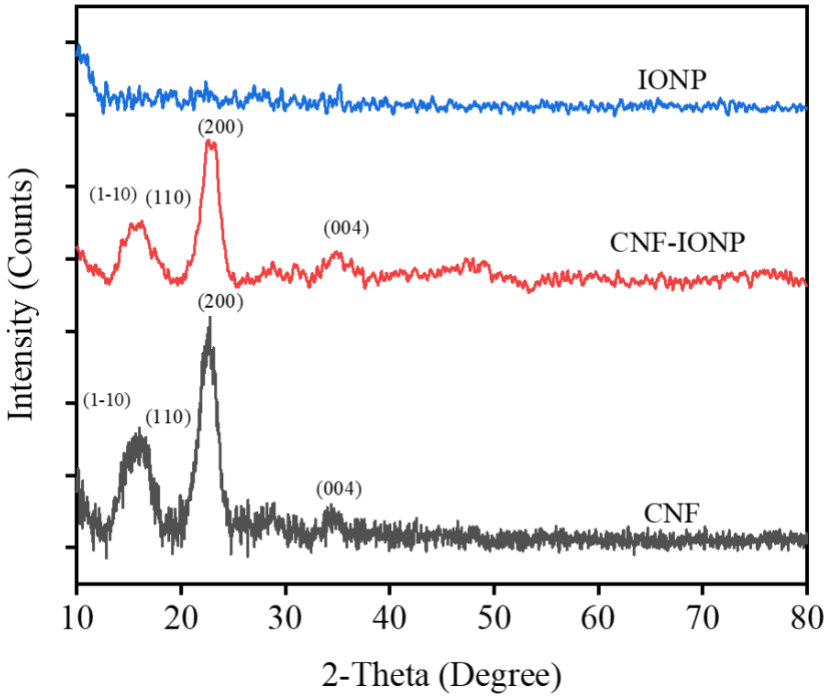

Figure 2.5. XRD spectra of the freeze-dried IONP, CNF-IONP and CNF aerogels.

Additional SEM analysis was conducted to evaluate the internal structure and morphology of IONP, CNF, and CNF-IONP aerogels (Figure 2.6). Figure 2.6A shows a photograph of the CNF-IONP aerogel. The IONP suspension precipitated in the absence of CNF due to their tendency to aggregate (Figure 2.6B). However, in the presence of CNF, the IONP did not precipitate. Instead, the IONP were immobilized on the cellulose fibrils (Figure 2.6B). Without IONP, CNF forms a highly porous structure resulting from freeze-drying of CNF suspensions (Figure 2.6C). The role of CNF in immobilizing the IONP on its surface was further verified by observing the IONP in the presence and absence of CNF using SEM. Figure 2.6D shows the freeze-dried IONP aggregates. The stable CNF suspension immobilized the IONP on the fibrils, resulting in a uniformly distributed nanoparticles within the aerogel (Figure 2.6E). This finding was further supported by EDS analysis (Figure 2.6F) of the aerogel which verified the uniform distribution of the IONP.

The porosity values of CNF and CNF-IONP aerogels were 98 and 95%, and their densities were 0.009 ± 0.01 and 0.013 ± 0.03 g cm^{-3}, respectively. The water absorption capacities for the CNF and CNF-IONP aerogels were 96.5 ± 4.9 and 74.9 ± 2.6 g g^{-1}, respectively. These results are in agreement with previously reported CNF aerogels of similar densities (Zhang et al., 2012).

The freeze-dried IONP exhibited a considerably high specific surface area of 165 m^2 g^{-1}. The BET surface area of CNF aerogel without additives is 13 m^2 g^{-1}, which is typical for this type of material (González-Ugarte et al., 2020). The minimal aggregation and uniform distribution of the IONP in the aerogel suggest that the surface area of the IONP was not compromised. The surface area of the amorphous IONP in this study is also higher than those of crystalline iron oxides such as hematite and maghemite (Hao et al., 2018; Macera et al., 2020) and comparable to other adsorbents doped with iron oxide nanoparticles (Hao et al., 2018).

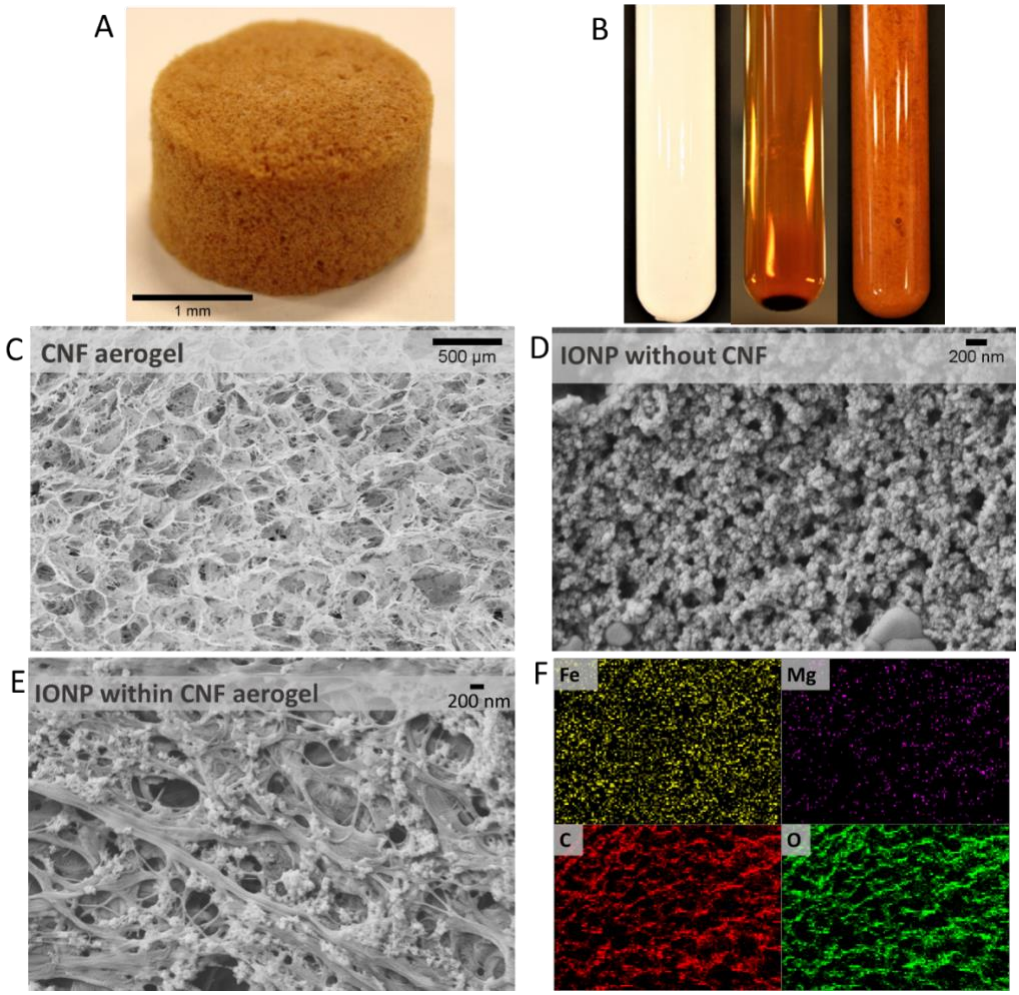

Figure 2.6. Photograph of CNF-IONP aerogel (A); from left to right: CNF suspension of 1 wt.% solids content, aggregated and precipitated IONP suspension, and IONP immobilized on CNF (B); SEM image of CNF aerogel macrostructure without IONP (C); SEM image of IONP (D); SEM image of 12.5% CNF-IONP aerogel (E); Corresponding EDS elemental mapping for CNF-IONP (scale bar: same as Figure C) (F). Note the different scales.

The structural stability of CNF-IONP aerogels when soaked in water and under constant agitation was assessed through mass loss measurements. The results showed that the <3% mass loss of aerogels was not statistically different ($p>0.05$) under various IONP loadings (Figure 2.7). This result shows that regardless of the IONP loading, they maintain their contact with the fibrils which renders the aerogel stable even with constant agitation for 12 h. We further supported this result by assessing the leaching of iron under the same conditions. The iron concentration in water after soaking the aerogels increased by <10 µg L^{-1} at pH 7. Although the leaching of iron is

minimal, this result has revealed the importance of rinsing the aerogels with water prior to its intended application.

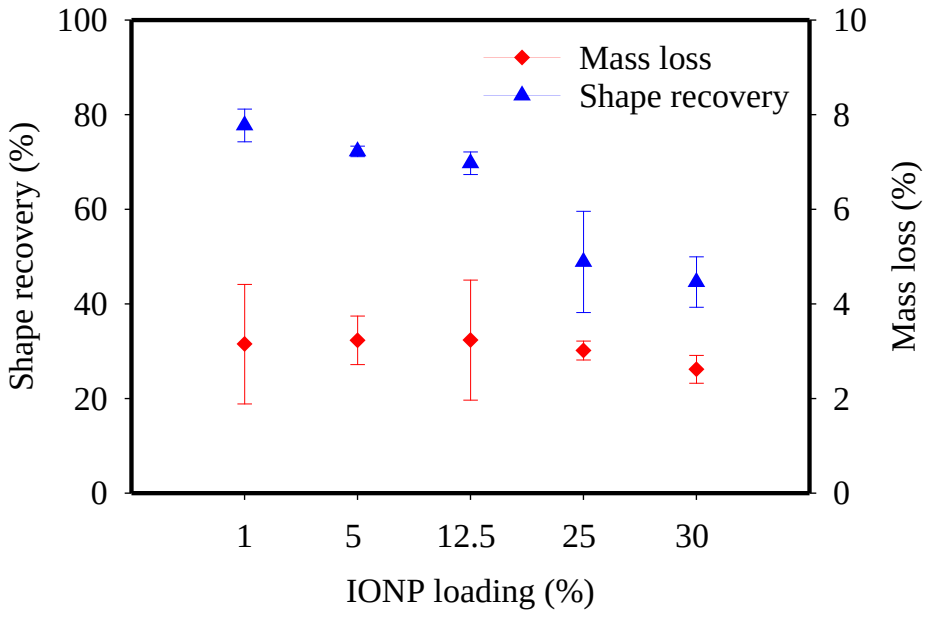

Figure 2.7. Shape recovery and mass loss of CNF-IONP aerogels at various IONP loading. Error bars represent standard deviation from triplet measurements.

In addition, the aerogels exhibited an interesting shape recovery pattern resulting from the addition of the epichlorohydrin cross-linker. The key role of the cross-linker is to impart adequate stability upon soaking the aerogels in water. Typically, CNF-based aerogels without a cross-linker tend to disintegrate in water. Here, when the CNF-IONP dry aerogel is compressed into a thin disk, at least 50% of the shape is recovered upon soaking in water. The shape recovery percentage ranged from 50% to 80% depending on the amount of IONP (Figure 2.7); a higher loading of IONP decreased the shape recovery. Typically, in crosslinked CNF-only aerogels, this phenomenon is attributed to the high surface tension of water which creates large capillary forces that expand the fibrils. Additionally, the diffusion of water into the pores coupled with partial swelling of amorphous cellulose augment the extent of recovery (González-Ugarte et al., 2020; Qing et al., 2013; Zhang et al., 2012). It is not surprising that the presence of the IONP decreased

the shape recovery percentage, which is presumably due to the partial disruption of the CNF network which renders the recovery more challenging.

To investigate the interaction between CNF and IONP, FT-IR spectroscopy was performed (Figure 2.8). In freeze-dried IONP sample, the peak at ~590 cm^{-1} is attributed to Fe-O band vibration (Battisha et al., 2006; Lassoued et al., 2017). The broad peaks at 3200~3500 cm^{-1} and ~1640 cm^{-1} were assigned to the stretching and bending vibrations of the OH group, respectively (Darezereshki, 2011). On the other hand, CNF and CNF-IONP aerogels exhibited almost similar IR spectra. The broad peak around 3380 cm^{-1} corresponds to OH stretching of CNF (Kondo, 1997). The N-H stretching originated from the cross-linking reaction (Rodriguez, 2010) overlaps with the OH stretching peak. Figure A2 shows the structure of the cross-linker and the proposed cross-linking reaction. The peak at 2905 cm^{-1} corresponds to the aliphatic C-H stretching (Zhang et al., 2017). The peaks at 1635 cm^{-1} and 1550 cm^{-1} correspond to amide I and II, respectively (Obokata & Isogai, 2007). In addition, the broad peak around 1250 cm^{-1} may be assigned to C-O stretching vibration for ester bonds due to the cross-linking (Obokata & Isogai, 2007). The intensity of this broad peak is lower in uncross-linked CNF samples compared to the cross-linked samples (Figure A3).

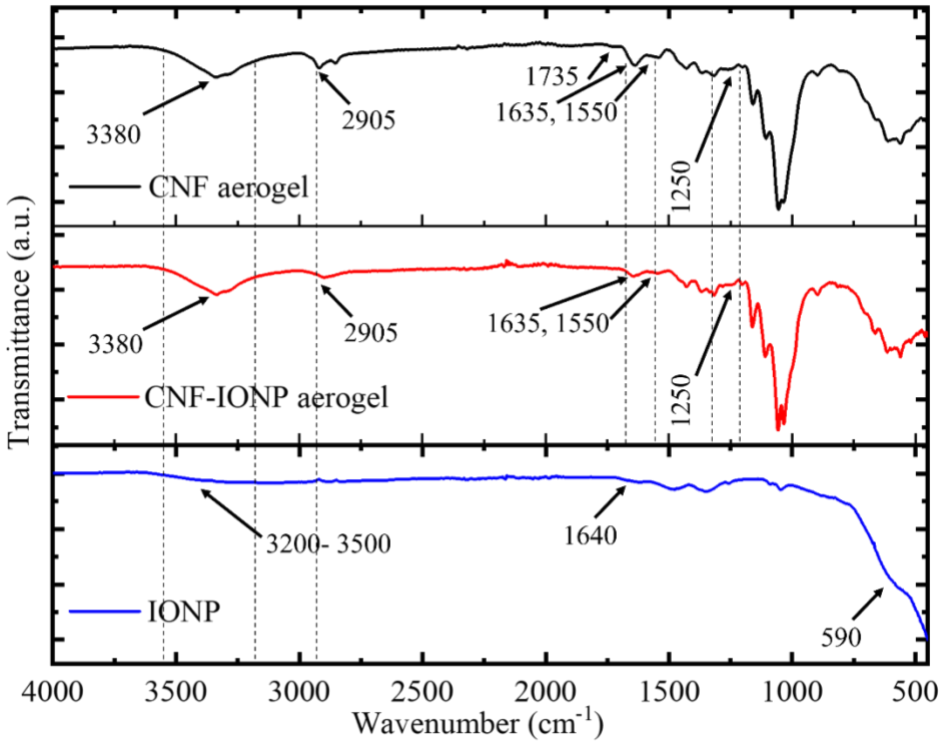

Figure 2.8. FT-IR spectra for freeze-dried IONP, cross-linked CNF, and CNF-IONP aerogels.

Although the CNF-IONP aerogels showed excellent stability in water aided by the cross-linker, no characteristic peak at ~1735 cm^{-1} which is attributed to C=O stretching vibration for ester group (Obokata & Isogai, 2007) was observed. However, this peak was visible in the cross-linked CNF aerogels, which can be disrupted by the presence of IONP. The FT-IR spectra of the CNF aerogels before and after cross-linking are presented in Figure A3. Besides this, no noticeable change was observed in the FT-IR spectra of CNF-IONP aerogel compared to CNF aerogel, which indicates that there is no evidence of chemical reaction between CNF and IONP. It is somewhat surprising that despite the absence of evidence for a chemical reaction, IONP is retained within the CNF structure remarkably well. This suggests that, in addition to Van der Waals interactions between CNF and IONP, other factors may be contributing to the stability of IONP within the aerogel such as mechanical interlocking (Zhang et al., 2019). It also suggests that the attraction forces between CNF and IONP are stronger than those between the IONP.

2.5 Conclusions

A novel and highly efficient CNF-IONP aerogel was prepared by incorporating IONP in CNF by simultaneous freeze-drying. This method addresses the previous issues of nanoparticle aggregation that enables the application of nanoparticle adsorbents in fixed-bed columns at the industrial scale. The amorphous nature of the IONP was verified by means of XRD analysis. The IONP had a remarkably high specific surface area (165 m^2 g^{-1}). A 12.5 wt.% IONP in the CNF aerogel resulted in a maximum arsenic removal and uniform distribution on the cellulose fibrils. The maximum adsorption capacities of CNF-IONP aerogel for As(III) and As(V) were 48 and 91 mg As g-$IONP^{-1}$, respectively. The adsorbent was stable in water and under constant agitation with negligible mass loss. In addition, the adsorbent exhibited a partial shape recovery functionality that could be advantageous in transportation purposes. Overall, this study will also provide a near-term alternative to efficient and bio-based commercial adsorbents for arsenic removal from water.

CHAPTER 3

FUNDAMENTALS OF HYBRID CELLULOSE NANOFIBRIL FOAM PRODUCTION BY MICROWAVE-ASSISTED THAWING/DRYING MECHANISM

3.1 Chapter summary

Cellulose nanofibrils (CNF) porous structures (foams/aerogels) are typically produced using energy-intensive processes such as freeze drying. In this study, a novel microwave-assisted thawing process was developed to produce low-density (36 kg/m^3) CNF foams. The process involved freezing of CNF and urea suspension followed by immediate thawing in the microwave. A slow freezing rate produced a uniform pore structure, whereas fast freezing using liquid nitrogen resulted in aggregation of CNF upon thawing. The in-situ carbamate crosslinking resulted from the addition of urea provided wet stability and was confirmed by FT-IR and nitrogen content analysis. The compressive properties of the foams were evaluated in both dry and wet conditions. In addition, iron oxide nanoparticles (IONPs) were used to assess the feasibility of producing hybrid foams through this novel method. This innovative and energy-efficient approach to produce foams from cellulosic nanomaterials has the potential to be scaled up and is expected to promote the use of renewable nanomaterials in a wider range of applications.

3.2 Introduction

Cellulosic-based materials have been receiving interest from a wide range of fields because of their distinctive attributes, particularly chemical inertness, exceptional mechanical properties, vast abundance, biodegradability, scope for chemical modification, and low thermal expansion coefficient (Moon et al., 2011; Phanthong et al., 2018; Trache et al., 2020). For example, the interest in cellulose-based packaging materials is continually rising as researchers attempt to replace petroleum-based plastics with goods manufactured from renewable materials (Chen et al., 2022; Hasan et al., 2021; Hossain et al., 2022). Other applications included recyclable composites (Li et al., 2022), energy storage (Chen & Hu, 2018), biological applications

(Jorfi & Foster, 2015), nutritional additives (LakshmiBalasubramaniam et al., 2021), and water treatment (Voisin et al., 2017).

While many forms of cellulose nanomaterials do exist, cellulose nanofibrils (CNFs) are a major type that are prepared by mechanical refining or other mechanical size reduction techniques (Moon et al., 2011). CNF-based foams are excellent alternatives to those made of petroleum-based materials (Nechita & Năstac, 2022). Due to the low thermal conductivity of CNF-based foams, there is a tremendous potential for their application in insulation (S. Jiang et al., 2021) and replacement of petroleum-based materials. Additionally, these foams and aerogels have effectively been used to filter contaminated water (Abdelhamid & Mathew, 2021; da Silva & Rosa, 2022; Rahman et al., 2021; Zhu et al., 2016).

Freeze drying and supercritical drying are common methods to produce low-density structures from CNFs (Lavoine & Bergström, 2017). However, these processes are lengthy and complex rendering them unattractive options to the industrial sector. Additionally, chemical modifications are oftentimes needed to overcome the inherent hydrophilicity of cellulosic materials. Other researchers have attempted to produce CNF-based foams using oven drying and foaming agents (Cervin et al., 2016; Park et al., 2021). A recent study reported the application of freeze-thawing-drying cycles in the presence of urea (Josset et al., 2017) to produce low-density structures from microfibrillated cellulose (MFC)- another term often used in lieu of CNF, using a combination of oven and air drying. An MFC to urea ratio of 1:1 was needed for producing the MFC foams with the least shrinkage and deformation. In addition, those MFC foams showed higher compressive properties compared to freeze-dried foams. However, the overall drying step was still time-consuming and somewhat comparable with freeze-drying/ supercritical CO_2 drying.

Urea has been extensively utilized to improve the solubility of cellulose in aqueous NaOH or LiOH solutions. To explain the urea-NaOH-water system, Cai & Zhang (Cai & Zhang, 2005) proposed a mechanism where dissolution of cellulose in LiOH/ urea and NaOH/ urea was performed at low temperature by forming a coating of urea hydrate around individual fibrils

governed by hydrogen bonding donor-acceptor interaction to prevent aggregation. A similar concept was utilized by Fauziyah et al. (Fauziyah et al., 2019) to make crosslinked cellulose aerogels from coir fibers. However, the interaction mechanism between cellulose and urea to form foam structures remains unclear.

A non-conventional technique to produce foams from lignocellulosic materials using microwave drying has been reported recently (Hafez & Tajvidi, 2021; Tauhiduzzaman et al., 2021). In those works, low-density foams from thermomechanical pulp fibers and wood sawdust were prepared using microwave drying, and CNFs were added as a binder. Compared to convection/oven drying, this method is considerably faster and more energy efficient (Nirmaan et al., 2020; Sun et al., 2016). During microwaving, heat is generated when a dielectric material with induced or permanent dipoles is subjected to microwave radiation. According to the literature, two mechanisms—dipolar polarization and ionic conduction—underlie microwave heating, while a third, known as interfacial polarization, combines the two (Anwar et al., 2015; Mingos & Baghurst, 1991).

Due to the potential to impart multifunctionality to the low-density fiber reinforced structures, hybrid CNF-based foams have received significant interest. Previous studies have addressed the importance of nanoparticle-incorporated CNF foams and the applications in fields such as fire retardant (Wang et al., 2019), energy storage (Rabani et al., 2021) and contaminant removal from water (Salahuddin et al., 2022). The absence of alternate drying techniques is a significant contributor to the high cost and energy consumption of the manufacturing process of these hybrid CNF foams. In our recent work (Rahman et al., 2021), we produced a freeze-dried iron-oxide-incorporated CNF aerogel that showed promising results for arsenic removal from water. However, the preparation of these low-density hybrid CNF aerogels is expensive, time-consuming, and not scalable. Therefore, presenting a proof-of-concept for the potential of other methods to produce hybrid foams will be valuable for a wide range of applications.

This study highlights a novel process of forming foams from CNF based on an immediate thawing protocol of frozen CNF suspension that was not previously reported. The study also provides an in-depth understanding of the immediate thawing process, chemical and physical interactions between CNF, urea, and water. In addition, the mechanism of foam formation using microwave system is investigated. The obtained foamed structures are characterized and the feasibility of forming hybrid foams from CNF and iron oxide nanoparticles is examined.

3.3 Experimental section

3.3.1 Material

Cellulose nanofibrils (CNFs) were provided by the University of Maine Process Development Center (PDC) (Orono, ME). The mechanically refined bleached softwood kraft pulp was used to produce 90% fine content (percentage of fibers with length < 200 μm) with a consistency of 3 wt.% CNF. Urea (NH_2CONH_2; 99.0-100.5%) was purchased from Sigma-Aldrich (St. Louis, MO, USA). Polycup^{TM} (polyamide-epichlorohydrin) 5150 crosslinker (26 wt.%) was supplied by Solenis (Wilmington, DE, USA). All reagents were obtained as analytical grade and used without further purification.

3.3.2 Foam preparation

A dry CNF to urea ratio of 1:0.25 was found most suitable for this foam forming method. Based on these calculations, the amount of urea required for the foam forming was added as an aqueous solution to dilute the 3 wt.% CNF suspension to 2 wt.% followed by a high shear mixing using an electric stirrer mixer (JJ-1 Precise Power Mixer, Hangzhou Feng Hai Electronic Commerce Co. Ltd., Zhejiang, China) for 5 min. In a rectangular plastic mold (5.23 cm x 5.23 cm x 1.82 cm), 40 g of CNF-urea suspension (UCNF) was placed. To control the freezing rate, the freezing chamber of a Harvest Right freeze-dryer (North Salt Lake, UT, USA) was used (no vacuum was applied). The UCNF suspensions were placed in the freezing chamber initially at 2 °C, and three freezing rates (0.06, 0.39 and 1.78 °C/min) were used to lower the temperature to

-20 °C. Freezing with liquid nitrogen (flash freezing) was also tested. Finally, all the frozen samples were stored in a freezer at -20 °C prior to the subsequent step.

The frozen UCNF suspensions were removed from the mold and placed on a paper towel in an LG LMC1575 microwave oven (LG Electronics Inc., Seoul, South Korea). The microwave oven has the option of customizing the power input (up to 1200 W) using a built-in smart inverter. The drying procedure comprised two stages. First, 1200 W of energy was applied for 3 min. Then, a total of 4 min of heating at 360 W was applied with 1 min intervals between every minute of heating to avoid over-drying. The final moisture content after microwaving was ~7-10%. Drying beyond a 7% moisture content resulted in shrinkage and warpage of the samples. To avoid this, the samples were kept at room temperature overnight to further reduce the moisture content. Finally, the foams were conditioned at a relative humidity of 50 ± 2% and a temperature of 23 ± 2 °C for 24 hours before further testing.

Hybrid foams were prepared by adding various amounts of iron oxide nanoparticles (IONPs) (3, 5, 7, and 10 wt.% based on the dry mass of CNF) to CNF and urea mixture. The preparation of IONPs was described by Rahman et al. (2021) (Rahman et al., 2021) and used herein to demonstrate the feasibility of preparing hybrid foams using our microwave-assisted thawing/drying method. Scheme 1 schematically illustrates the UCNF foam forming procedure.

Freeze dried foams were prepared for comparison purposes. To this end, two different batches of 2 wt.% CNF were prepared with and without Polycup^{TM} crosslinker (5 wt.% of the total dry mass of CNFs). The CNFs with crosslinker were stirred with a magnetic stirrer for 5 mins to ensure the homogeneous mixing of the crosslinker. Finally, the suspensions were poured in the rectangular molds to freeze dry in a Harvest Right freeze-dryer (North Salt Lake, UT, USA).The temperature cycles of the freeze dryer were - 34.4, - 6.7, 4.4, 15.6, and 32.2 °C for 8, 10, 8, 3, and 3 h, respectively. The CNF samples with crosslinker were cured in a vacuum oven for 3h for 105 °C to induce the crosslinking.

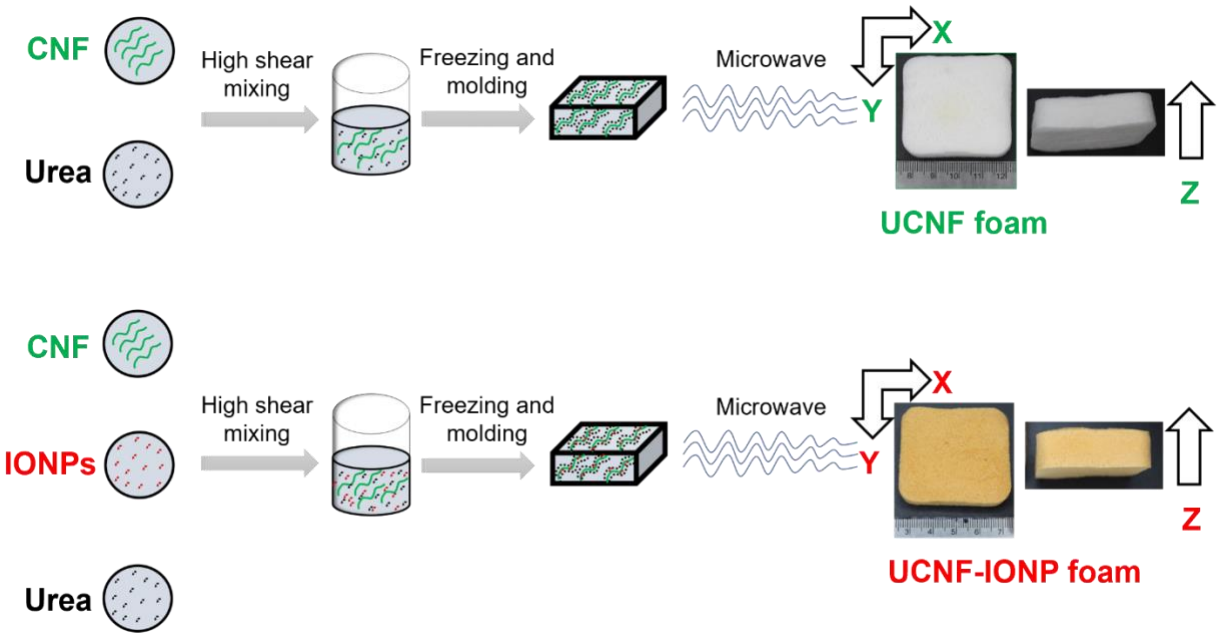

Figure 3.1. Schematic diagram of UCNF and UCNF-IONP foam forming procedure

3.3.3 Foam characterization

The morphology of the foams was examined using a Zeiss NVision 40 scanning electron microscope (SEM; Carl Zeiss AG, Oberkochen, Germany). The foam specimen was sliced (2-4 mm thick) with a sharp blade and placed on a sample stub using a double-sided carbon tape. All the samples were sputter coated with a 10 nm layer of gold-palladium and an electron high tension (EHT) voltage of 3 kV was maintained at the time of scanning.

Optical microscopy was performed using an Olympus SZX16 dissecting microscope (Olympus Corporation, Shinjuku-ku, Tokyo, Japan) fitted with a Zeiss Axiocam Erc 5s (Carl Zeiss AG, Oberkochen, Germany). The X-Y and Z- directional cross sections of the UCNF foams were sliced using a sharp blade while maintaining 2-4 mm of thickness.

The nitrogen content of the UCNF foams was measured by a Leco TruMac CN928 Carbon/Nitrogen analyzer (Leco corporation, St. Joseph, MI, USA) using the combustion method. Leco orchard leaves were used as a certified reference material with a N content of 2.31 ± 0.05 %. Three replicates of each type were used to calculate an average.

The mass loss experiments for both UCNF and UCNF-IONP hybrid foams in water were conducted by agitating the foams at 125 rpm for 48 h followed by drying in a convection oven at 80 °C for 6 h. The mass loss (%) was calculated gravimetrically by comparing the dry weights of the initial and post-dried foams.

A Spectrum Two™ FTIR spectrophotometer (PerkinElmer, Waltham, MA, USA) was used to examine chemical interactions between CNF and urea. Additionally, one of the UCNF foam samples was rinsed thoroughly with 2 L of water to remove residual urea and subsequently dried in a convection oven for 6 h at 80 °C. The spectra were normalized with respect to the wavenumber 1055 cm^{-1} that represents the stretching vibration of cellulose backbone not altered by any reaction (Zhang et al., 2012).

To further evaluate the chemical properties of the foams, ^{13}C solid state NMR was performed using a Neo 600 MHz system (Bruker Corporation, Billerica, MA, USA) equipped with a high-resolution magic-angle spinning (HRMAS) probe operated at 10,000 Hz. Foam samples were cut into 1 mm x 3 mm pieces weighing ~30 mg, and firmly packed into a 50 µL rotor. One dimensional (1D) ^{13}C spectra of each sample was collected with 720 scans (1 h), which was repeated 17 times (total 18 spectra per sample). The spectra of each sample were processed, referenced to the ^{13}C spectrum of glucose standard, and summed as the final ^{13}C spectrum with Mnova 14 software (Mestrelab Research, S.L., A Coruña, Spain).

Additional experimental details are available in the appendix B.

3.4 Results and discussion

3.4.1 Factors influencing the formation of porous foam structures

Figures 3.2A and B show the change in foam density and volumetric shrinkage as a function of urea content. Foams prepared with 5 wt.% urea content had the highest density (91 kg/m^3) and maximum shrinkage. There is no statistical difference in densities among samples prepared with 15, 25, and 50 wt.% urea (32–40 kg/m^3). With respect to shrinkage, there is no

statistical difference in volumetric shrinkage values of foams containing 15, 25 wt.% urea. However, the similar CNF consistency freeze-dried foams showed statistically lower density (25 ± 0.6 kg/m^3) and shrinkage (21 ± 2%) values compared to the UCNF foams prepared through microwave irradiation. Although, there was no statistical difference in densities between 15 and 25 wt.% UCNF foams, foams with 25 wt.% urea were used for the rest of the experiments due to their shape uniformity. This urea wt.% is lower than that used in the previously published studies (Antonini et al., 2019; Josset et al., 2017), where a 1:1 CNF: urea ratio was needed to obtain a foamed structured via a freeze-thawing process followed by oven and air drying. The porosity of the UCNF foams with 25 wt.% urea content was 97–98 %. These foams were prepared through instantaneous microwave thawing, which means that the frozen samples were immediately placed in the microwave for thawing and drying. The effect of thawing conditions will be discussed further in later sections.

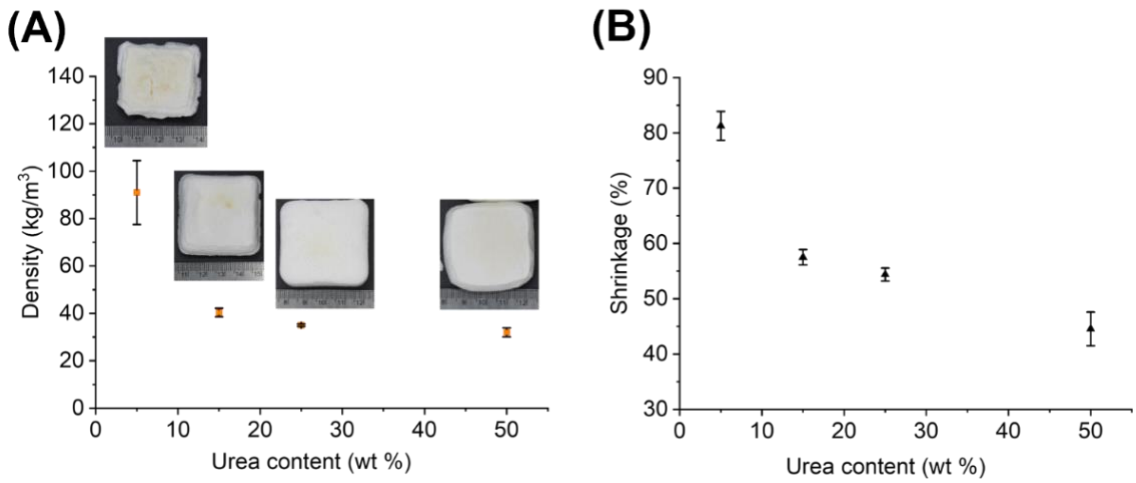

Figure 3.2. Change in density (A) and volumetric shrinkage (B) of the UCNF foams with respect to urea content. The error bars represent one standard deviation among three replicates. The digital photograph for each sample is shown on the corresponding density plot.

SEM images of foam samples with and without urea are shown in Figure 3.3A. It is evident that CNF without urea did not produce any foam structure. Starting from 15 wt.%, the open cell pore structures became more visible. The foams prepared with 25 and 50 wt.% urea content also

showed similar pore structures; however, an increase in the urea content resulted in a decrease in the loosely hanging fibrils that may be due to the hydrogen bonding of residual urea with CNF surface (Holm Kristensen et al., 2004) or the higher extent of crosslinking which will be discussed in a later section. The pores structure of freeze-dried foams without addition of urea were nearly similar to the UCNF foams (Figure 3.3B) at similar densities. However, the presence of loosely hanging fibrils is more noticeable in freeze-dried foams, which could be attributed to the lack of crosslinking among cellulose fibrils (González-Ugarte et al., 2020).

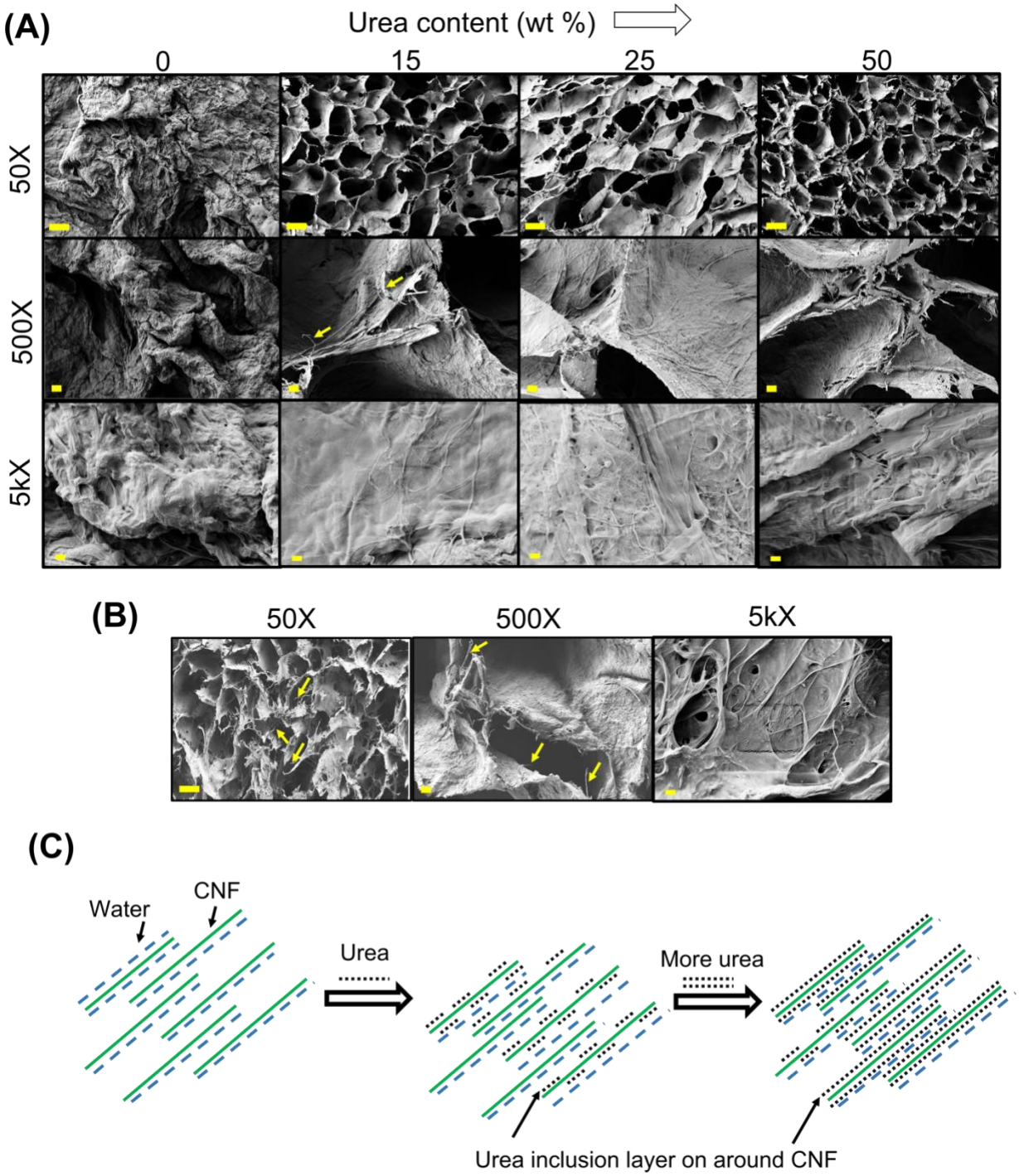

Figure 3.3. SEM micrographs of CNF foams without (0 wt.%) and with (additional 15, 25 and 50 wt.% of the dry mass of CNF) urea using MW irradiation (A), and freeze-dried neat CNF foams without urea of similar consistency in 50X, 500X and 5kX magnifications (B). Scale bar at 50X is 200 µm, 500X is 10 µm, and 5kX is 1 µm. The arrows indicate loosely hanging fibrils. The schematic presentation of the effect of urea on the formation of the inclusion layer around CNF (C).

Jiang et al. (Jiang et al., 2014) investigated the interactions among NaOH, urea, and cellulose in water. Although there was no direct interaction between cellulose and urea, as demonstrated by temperature-dependent NMR data, OH^- groups in NaOH interact with urea to create an inclusion complex with cellulose. Further addition of urea increases the inclusion complex's stability by reducing its mobility. Interestingly, at low temperature below 25 °C, intermolecular hydrogen bonds between cellulose molecules have been demonstrated to initiate breakdown, preventing the aggregation of individual cellulose inclusion complexes.

On the other hand, Cai et al. (Cai et al., 2012) investigated the interaction between cellulose and urea in aqueous medium without the presence of NaOH using molecular dynamics simulation. The study revealed that the stability of the inclusion layer complex between cellulose and urea depends on the minimized interaction between cellulose chains. This phenomenon is caused by the formation of hydrogen bonds between cellulose and urea molecules using the oxygen atoms of urea as proton-acceptors and the hydroxyl hydrogen atoms of cellulose as proton-donors. This kind of hydrogen bonding between cellulose and urea is very temperature sensitive and maintains the stability of the inclusion complex below 265 K (-8.15 °C). This study also revealed that, in a cellulose/urea/water system, almost two thirds of the cellulose-water hydrogen bonds were replaced by cellulose-urea hydrogen bonds allowing the formation of inclusion layers of urea around cellulose at a low temperature (Figure 3.3C). To verify this in our system, two additional thawing conditions were studied in addition to instantaneous thawing. The two conditions are 1) thawing at 8 °C for 24 h, and 2) thawing at room temperature (~ 23 °C) for 24h, both followed by the same microwave drying conditions. Figures B1A and B show that as the thawing temperature increases, the formed structures become denser.

Figures B1C and D show the effect of freezing rate on the density and shrinkage of the UCNF foams. One-way ANOVA showed that density (35–37 kg/m^3). and volume shrinkage were not statistically different at different freezing rates. However, flash freezing using liquid nitrogen resulted in a collapsed and dense structure during microwave drying which indicates that the rate

of freezing might be a critical factor for forming this type of structure. Besides, when CNF suspension of similar consistency (without urea) was frozen and instantaneously thawed by microwaving, its structure collapsed, regardless of the freezing rate. This was expected given the extensive network of hydrogen bonding those forms between the fibrils. Therefore, it is reasonable to assume that additional factors might influence the formation of porous structures of CNF/urea along with the freezing rate such as capillary forces due to the partial melting of ice crystals before the evaporation during microwave drying.

Although foams prepared at different freezing rates did not vary in their densities, the internal pore structures were different. The UCNF foam prepared at a slow freezing rate (0.06 °C/min) had a more homogenous internal pore structure compared to foams prepared at a fast-freezing rate (0.39 °C/min) that showed a less uniform pore structure by forming large irregular voids and cracks inside (Figure 3.4A).

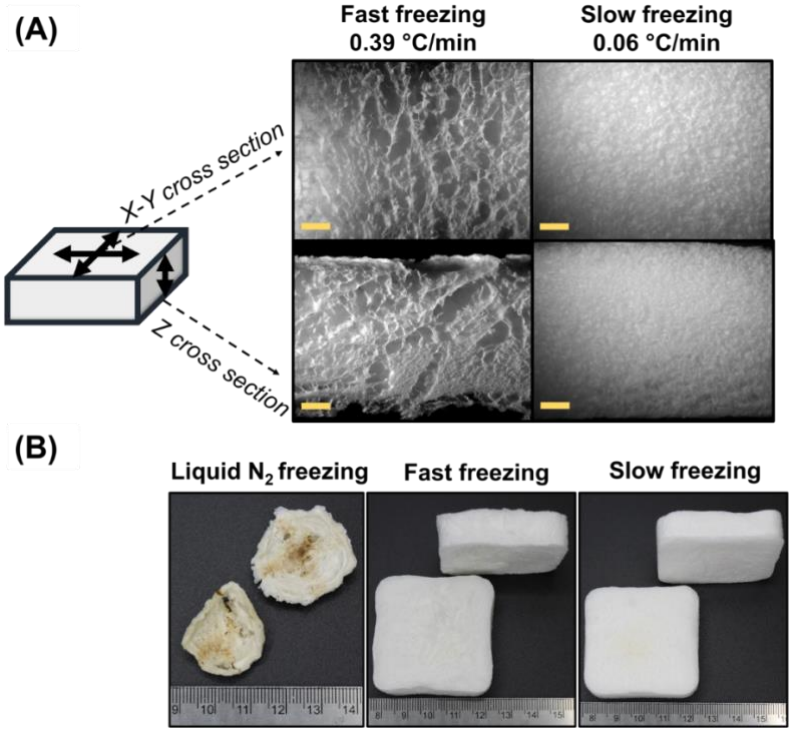

Figure 3.4. Variation of foam morphology observed under optical microscope along the X-Y and Z directional cross section (Scale bar: 2 mm) (A), and the digital photographs of UCNF foams with different freezing rate after drying in microwave (B). Ruler units are in cm.

The formation of distinct pore morphologies at different freezing rates may be caused by several concurrent events. Ice crystal size in a frozen sample is known to be significantly influenced by freezing temperature and rate. The present study deals with the UCNF suspension where the urea acts as the solute component of the system. It is worth noting that the difference in freezing rates of the samples with and without urea under the same freezing conditions (fast freezing) was insignificant. The 2 wt.% CNF suspension without urea had a freezing rate of 0.42 °C/min whereas with 25% of additional urea the freezing rate was 0.43 °C/min. Moreover, according to the freezing point depression principle, the addition of urea to water decreases the freezing temperature to a small extent, which likely does not affect the pore size significantly.

The overall time required to freeze UCNF suspension may affect the formation of urea inclusion complexes with cellulose. On one hand, slow freezing could allow sufficient time for the urea inclusion complex to form around individual fibrils resulting in homogenous pore sizes after drying. Additionally, the coalescing of ice crystals might also take place during freezing at slow freezing rate (Regand & Goff, 2003).

On the other hand, a fast-freezing rate might cause partially formed self-assembled urea inclusion complexes around the cellulose fibrils. Due to incomplete inclusion, the relative distances among those inclusion complexes might not be homogeneous which could be responsible for partial agglomeration of CNFs resulting in big non-homogeneous pores in the sample after drying.

Finally, in the case of liquid nitrogen/flash freezing, CNFs agglomerated after microwave drying without creating a porous structure (Figure 3.4B). This may also be related to the ice crystal size as well as time associated with the formation of urea inclusion complex. It is known that liquid nitrogen freezing produces a large number of tiny crystals (Zhang et al., 2022) that do not have sufficient time to coalesce compared to the conventional fast or slow freezing. Besides, due to the shortest possible freezing time, the self-assembled urea inclusion layer might not develop to the level necessary to create a porous structure. At the same time, the interfibrillar distance is

significantly smaller due to the formation of tiny ice crystals, which brings the CNFs closer to each other resulting in their agglomeration upon microwave drying. Consequently, even in the presence of urea, the intermolecular hydrogen bonding among CNFs becomes the dominating factor for agglomeration after drying the frozen suspension. The schematic for the proposed mechanism is presented in Figure 3.5A.

3.4.2 Effect of microwave power

Four microwave power settings (360, 600, 840 and 1200 W) were tested to examine their effect on the foam structure. Higher power results in more vigorous vibration of water molecules, and hence, faster water removal and possibly changes in the internal pore structure. At 360 W, the foams required 9 min to reach a moisture content of ~7-10%, whereas at 1200 W, the same moisture content was reached in 4 min. The density of the foams prepared at 360 W was significantly higher (47 kg/m^3) compared to the other power settings (40–42 kg/m^3). The increased density at the lowest power setting (i.e., longest drying time) indicates the critical role of thawing time in obtaining a porous structure.

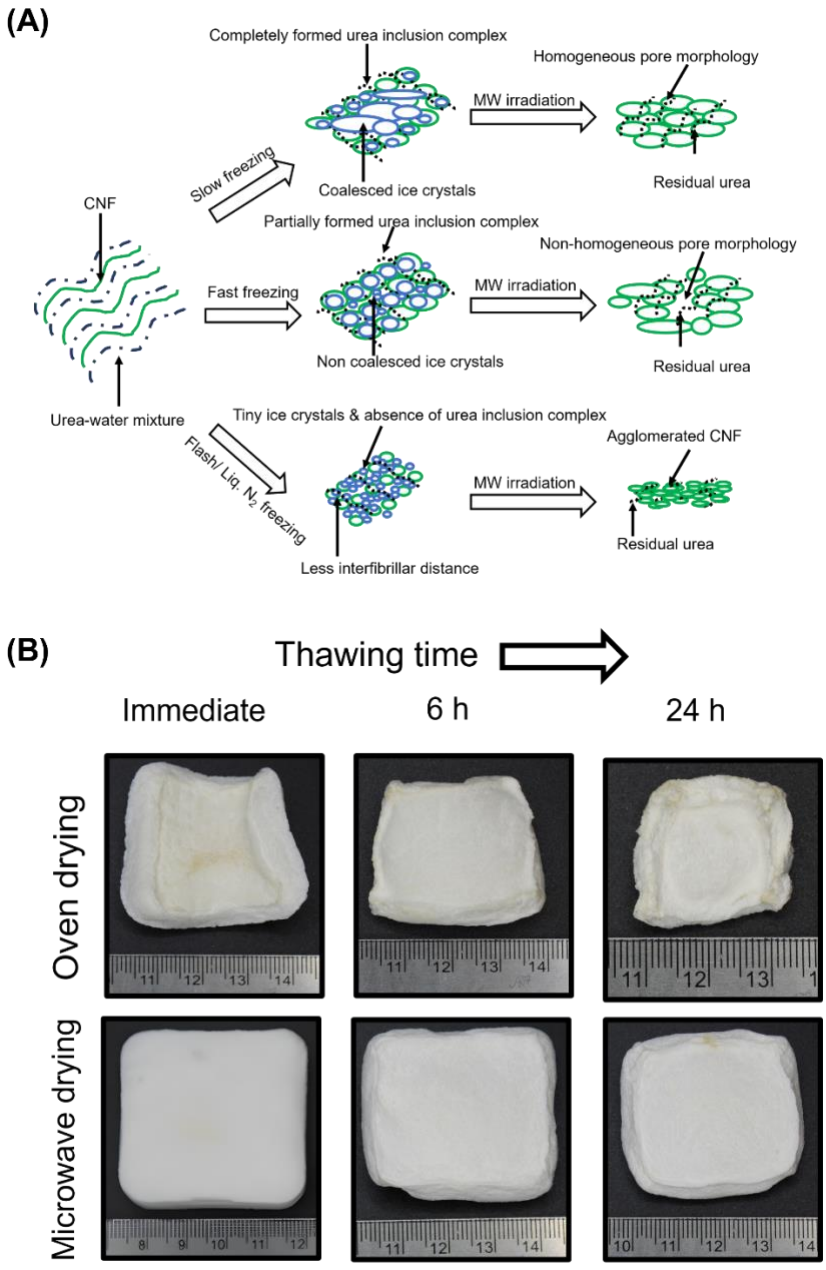

Figure 3.5. Proposed foam forming mechanism involving ice crystals and the urea inclusion layer with different freezing pathways (A) and the UCNF foams dried in the oven and microwave immediate after freezing, after 6 h and 24 h of room temperature thawing (B).

This finding supports the results shown in Figures B1A and B, where prolonged exposure to a higher temperature (8 and 24 °C) during thawing resulted in a dense and collapsed structure. To further support this finding, UCNF foams were prepared using oven drying and were compared with those prepared by microwaving. The time required to oven dry a foam sample at 80 °C

containing 97.5% of 'frozen' water was 6 h, which was considerably longer than microwaving. Figure 3.5B shows digital photographs of UCNF foams dried by microwave and oven after different thawing times. The results show the oven drying resulted in denser and less uniform structures compared to those prepared by microwaving. Again, this verifies the importance of instant and rapid thawing/drying through microwave drying to form uniform porous structure from urea and CNF. Finally, to examine whether continuous or non-continuous drying influence foam structure, foams were dried continuously without intervals. The results showed that there was no statistical difference between the two sets of samples.

3.4.3 Foam stability and crosslinking

UCNF foams showed favorable stability in wet conditions. The mass loss after soaking and agitating in water was less than 1 wt.%, which suggests the possibility of a crosslinking event. It is likely that this stability is due to covalent bonding rather than weak physical interactions. To further investigate this, FTIR analysis was performed on UCNF, rinsed UCNF, and freeze-dried CNF foams (Figure 3.6A). FTIR spectra of all three samples showed a broad peak around 3340 cm^{-1} and a sharp one at 2916 cm^{-1} corresponding to -OH stretching and -CH stretching vibration, respectively (Hospodarova et al., 2018). Cellulose peaks between 1650 and 900 cm^{-1} were observed as well as a 1644 cm^{-1} peak for the adsorbed water molecule -OH group in cellulose surface (Poletto et al., 2011). However, in case of UCNF foam, a new peak at 1715 cm^{-1} was observed which corresponds to the carbamate carbonyl group (C=O) (Segal & Eggerton, 1961; Willberg-Keyriläinen et al., 2018; Xiong et al., 2017). The peak at 1666 cm^{-1} is attributed to the carbonyl group of urea. To eliminate the effect of unreacted urea, the foams were rinsed with water to wash out residual urea. The small carbamate carbonyl peak of washed sample shifted to a higher wavenumber at 1745 cm^{-1} as opposed to 1715 cm^{-1} in unwashed samples. According to the literature, the peak in this region corresponds to carbonyl group of cellulose ester (Fei et al., 2017; Jandura et al., 2000), suggesting the formation of ester groups between urea and cellulose upon heating.

Furthermore, Figure 3.6B shows the solid-state ^{13}C HRMAS NMR spectra for the same three samples. The chemical shifts of carbon in the spectra could be assigned to 103.6 ppm for interior C4, 73.7 ppm for C2, C3, C5 and 63.7 ppm for C6 (Isogai et al., 1989). Apart from the peaks for cellulose, there are a few subtle differences among the three NMR spectra. The chemical shifts of the C=O group for crystalline urea was at 163.4 ppm (Guo et al., 2009). This urea C=O peak shifted to 160.1 ppm due to the adsorption of urea on cellulose induced by weak hydrogen bonding (Holm Kristensen et al., 2004).

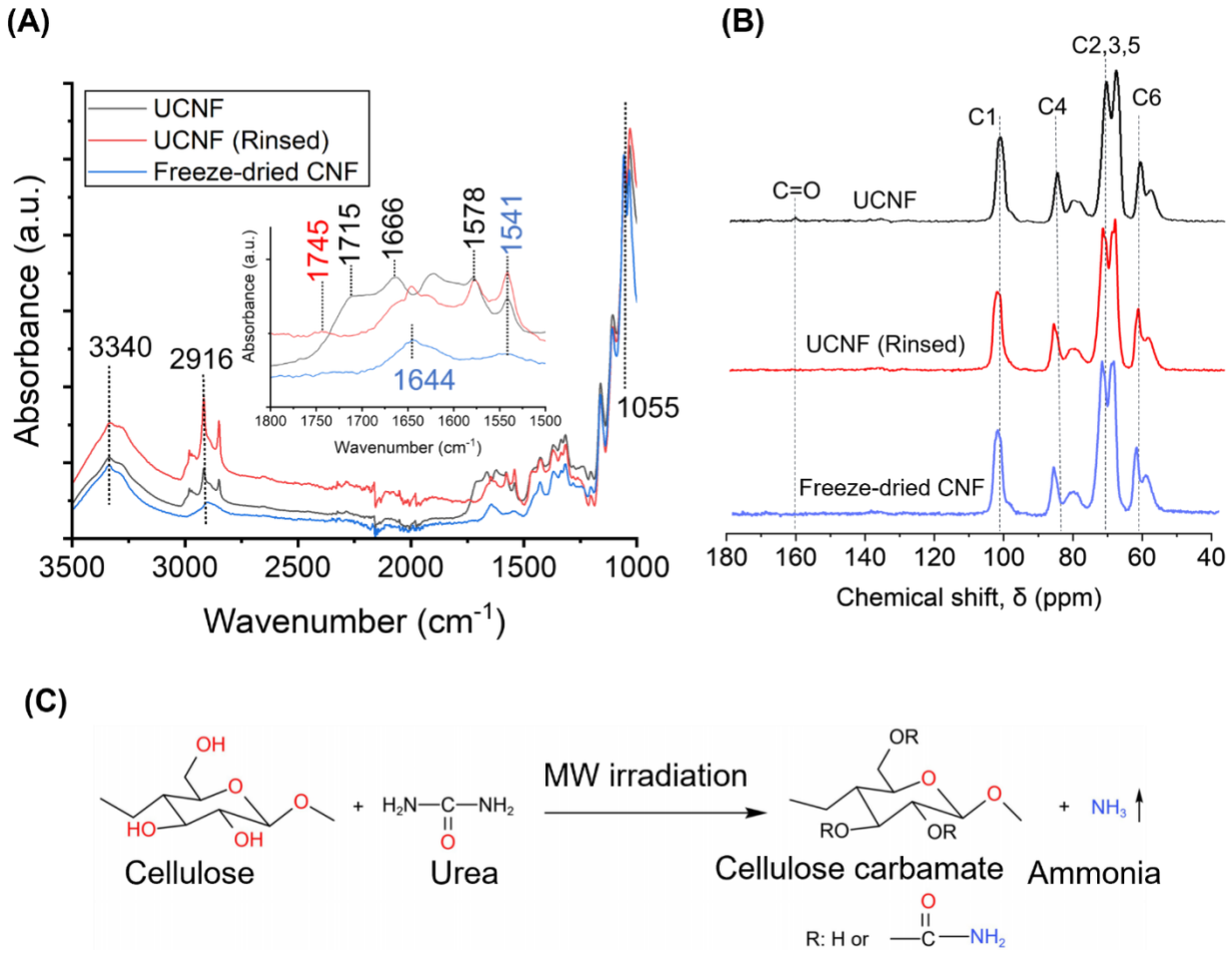

Figure 3.6. FT-IR (A), ^{13}C HRMAS NMR (B) spectra of different CNF foams and the possible crosslinking reaction (C).

However, upon rinsing with water, this peak was not observed indicating that the peak corresponded to residual urea. Hence, it may be possible that the stability of foams in water was

caused by a small amount of urea that reacted with cellulose that was undetected by NMR and hardly by FTIR. Further characterization will be needed to gain insights into the wet stability of the foams.

To confirm this, nitrogen content of foams was measured by the combustion method. The results showed that freeze-dried CNF foams contained a negligible amount of nitrogen (0.04%) likely due to impurities in the cellulose fraction. On the other hand, the nitrogen content of the UCNF foams was 3.5%, which reduced to 1.55% after rinsing with water. Doubling the amount of rinse water resulted in a negligible loss of nitrogen content (1.34%). This result, combined with FTIR and NMR, suggests the presence of covalent bonds between cellulose and urea that likely form cellulose carbamate esters. These covalent bonds, however, were hardly detectable by FTIR and NMR due to their small concentrations. This extent of crosslinking, however, is sufficient to render the foams stable in water when mildly agitated. The resulting crosslinking is likely due to heat-induced reaction during microwaving (Figure 3.6C). Previous studies reported the formation of cellulose carbamate by heating cellulose and urea. For instance, cellulose carbamate has been synthesized in cotton linters via microwave irradiation (Guo et al., 2009, 2010).

In addition to the crosslinking reaction, it is important to shed light on the decomposition of urea. The mechanism of aqueous urea decomposition has been investigated by computational methods previously (Alexandrova & Jorgensen, 2007). It was reported that urea preferentially decomposes in aqueous medium to ammonium rather than hydrolysis due to less required activation energy. The effect of temperature on aqueous urea decomposition has been studied in a separate work that examined the extent of urea decomposition at 60–100 °C range (Shaw & Bordeaux, 1955). In the present study, the extent of urea decomposition was determined gravimetrically by measuring the mass of dry foam and comparing it with the initial dry mass. The mass difference was negligible, assuming insignificant decomposition of urea during drying.

3.4.4 Hybrid foams

Hybrid foams were prepared by incorporating IONPs into the foams at various loadings. The density of the foams ranged between 31–45 kg/m^3 after the addition of IONPs. Hybrid foams were also tested for their stability in water under agitation. The average mass loss of the hybrid foams containing 7 wt.% IONP was 10%, whereas at 3 wt.% IONP mass loss was at 5.3%. However, an IONP loading of 10 wt.% resulted in a significantly higher mass loss (33%).

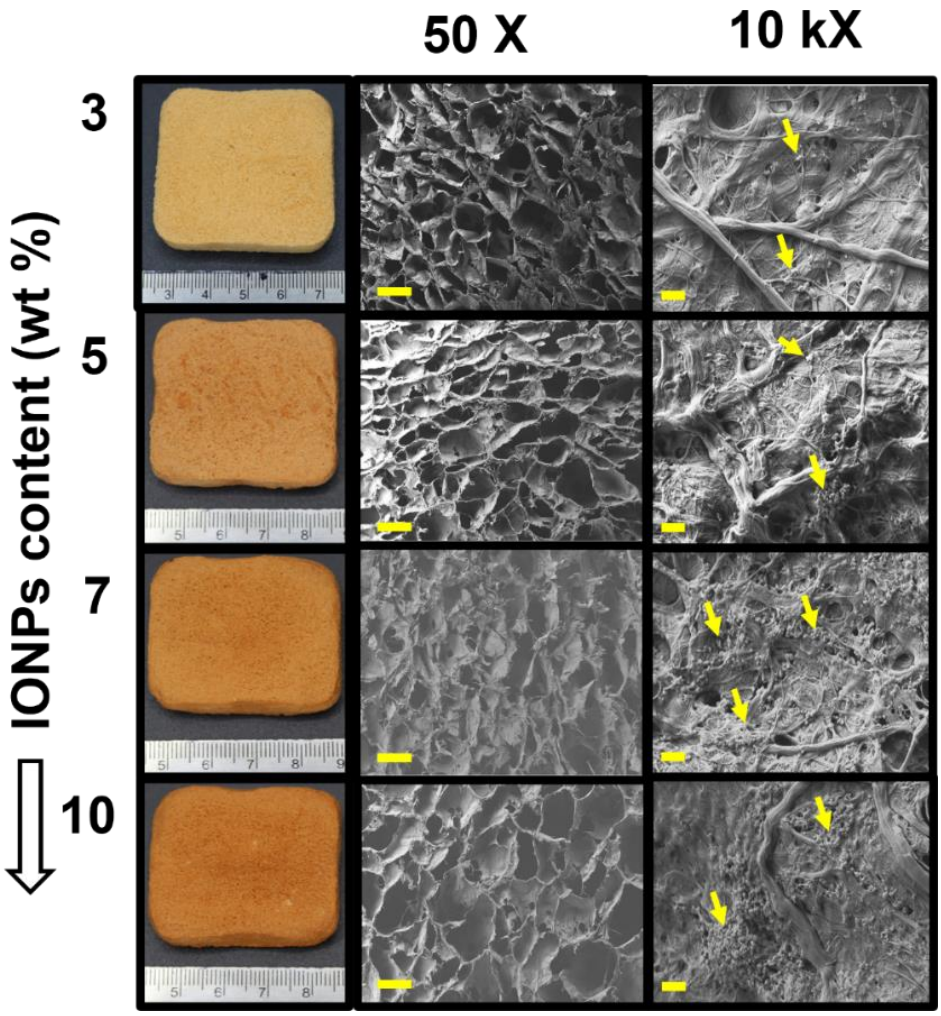

Figure 3.7. Digital photographs of UCNF-IONP hybrid foams with different IONP contents and the SEM images of corresponding hybrid foams in two different magnifications (50X and 10 kX). The arrows indicate the cluster of IONPs. Scale bar for 50X is 100μm and for 10 kX is 1 μm).

Figure 3.7 shows the digital photographs and SEM images of the UCNF foams with different IONP loadings. A previous study measured the IONP specific surface area at 162 m^2g^{-1} (Rahman et al., 2021). Due to their hydrophilic nature and positively charged surface under the pH condition of this study, the IONP surface forms hydrogen bonding as well as physical cross-linking with the CNF (Dang et al., 2018). As the IONP concentration increases, they tend to form multilayered clusters. The diameter of these clusters ranged from ~300 nm at 3 wt.% to ~2.3 µm at 10 wt.% IONP, as measured from the SEM micrographs. This could explain the increased mass loss of foams containing 10 wt.% IONP which results from the higher fraction of agglomerated IONPs within the foam which disrupts the extent of carbamate crosslinking leading to the disintegration of the foam in contact with water.

3.4.5 Comparison of foam processing procedures

Table 3.1 presents a comparison of the physical properties of cellulose-based foams/aerogels prepared by different procedures. Ferenczi et al. (Ferenczi et al., 2018) investigated power consumption of different drying techniques. The results showed that the microwave vacuum drying requires almost 12 times less energy than freeze-drying. Apart from energy and time efficiency, there are several additional advantages of the foams produced by microwave irradiation in the present study. Firstly, there is no external foaming agent such as Octylamine (OA) or Pluronic P123 used for this foam forming process; such reagents have been used extensively by previous studies, especially while replacing freeze-drying or supercritical CO_2 drying with oven/convection drying (Cervin et al., 2016; Demitri et al., 2014; Gordeyeva et al., 2016; Park et al., 2021). Secondly, in this study, the wet stability of the foams is achieved with an in-situ crosslinking reaction compared to the more complex steps reported in previous studies (Cervin et al., 2016; González-Ugarte et al., 2020; Hossen et al., 2018). To combine all aspects, this study reports a simple approach for producing wet stable CNF-based foams with significant time and energy efficiency.

Table 3.1. Comparison among cellulose based foams/aerogels processing procedures

Nanocellulose type	Reagents	Processing technique	Drying technique and time	Density (kg/m^3)	Porosity (%)	Stability in water	Reference
TEMPO-CNF	–	FC	FD	5.6	99.6	–	(Wicklein et al., 2015)
CMCNF	OA	High speed mixing	OD	9 – 109	92.7 – 99.4	–	(Park et al., 2021)
TEMPO-CNF	OA and SMP	High speed mixing	OD	6 – 200	87 – 99.6	Hydrophilic & Stable	(Cervin et al., 2016)
TEMPO-CNF	Pluronic P123, $CaCO_3$ and GDL	High speed mixing	CD	9.6 – 15.2	–	–	(Gordeyeva et al., 2016)
CMCNa	PEGDA and Pluronic F-127	High speed mixing	MWC & VD	–	–	–	(Demitri et al., 2014)
CNF	EtOH, 2-Propanol and PVA	Freezing with dry ice & EtOH	SE and AD	18	>98	–	(Li et al., 2017)
MFC	Urea	Controlled freezing	AD (48 h) & OD (18h)	29.1 – 36.4	97.4 – 98.1	–	(Josset et al., 2017)
CNF	–	Liquid N_2 freezing (10 s) or conventional freezing (24 h)	$ScCO_2$ drying	9 – 50	96.9 – 99.4	–	(Ciftci et al., 2017)
CNF	TiO_2	Freezing and ALD	FD	20 – 30	>98	Hydrophobic	(Korhonen et al., 2011)
TEMPO-CNF	EtOH and tBuOH	SE	$ScCO_2$ and FD	24.3	–	Unstable	(Darpentigny et al., 2020)

Table 3.1 continued

NFC	TMCS	Freezing and VPD	FD	3.12	–	Hydrophobic	(Xiao et al., 2015)
NFC	PVA	Freezing (6h)	FD (48 h)	7 – 20	99.51 – 98.52	Hydrophobic	(Chhajed et al., 2019)
CNF	MetCMC	UV-radiation followed by freezing in liquid N_2	FD	87.5	95	Stable	(Hossen et al., 2018)
CNF	Urea	Conventional freezing	MW (7 min)	35-37	>97	Stable	This work
CNF	Urea and IONPs	Conventional freezing	MW (7 min)	37 – 38	>97	Stable	This work

Abbreviations: TEMPO: 2,2,6,6-tetramethylpiperidine-1-oxyl radical, CMCNF: Carboxymethyl cellulose nanofibrils, OA: Octylamine, SMP: Sodium (meta)periodate, Pluronic P123: Pluronic tri-block (EO-PO-EO) copolymer P123, GDL: D-(+)-gluconic acid d-lactone, CMCNa: A sodium salt of carboxymethylcellulose, PEGDA: Polyethylene glycol diacrylate, PVA: Poly (vinyl alcohol), TMCS: Trimethylchlorosilane, NFC: Nanofibrillated cellulose, VPD: Vapor phase deposition, MetCMC: Methacrylate functionalized carboxymethyl cellulose, FC: Freeze casting, FD: Freeze-drying, OD: Oven-drying, CD: Convection-drying, MWC: Microwave curing, VD: Vacuum drying, MWC: Microwave curing, AD: Ambient-drying, SE: Solvent exchange, $ScCO_2$ drying: Supercritical CO_2 drying, TiO_2: Titanium dioxide, $CaCO_3$: Calcium carbonate, ALD: Atomic layer deposition, MFC: Microfibrillated cellulose, EtOH: Ethanol, tBuOH: tert-Butyl alcohol, MW: Microwave irradiation.

3.4.6 Mechanical properties

Figure 3.8A shows compressive stress-strain curves for the UCNF foams with 25% urea and UCNF-IONP foams with 25% urea and 3% IONPs in both wet and dry conditions performed with an experimental setup presented in Figure 3.8B. Freeze-dried CNF foams were also tested for comparison purposes. Those foams had a density of 26.4 kg/m^3 and were crosslinked using 5 wt. % Polycup^{TM}. The dry CNF and UCNF foams showed three regions for a typical foam compressive stress-strain curve: linear elastic region, a stress plateau region, and a densification region (Gibson & Ashby, 1997) . The compressive stress of the dry foams increased gradually up to 65% and rapidly afterwards (densification region). Although the compressive modulus of the dry foams was not statistically different, the compressive strengths were different (Figure 3.8C). Freeze-dried CNF foams showed slightly higher compressive strengths compared to the UCNF foams at

similar strain levels. It is worth mentioning that the compressive moduli and strengths at both 10% and 25% strain levels for UCNF foams did not show any statistical difference from the UCNF-IONP foam. Also, the UCNF foams showed lower compressive modulus compared to the previous urea-based foams (Antonini et al., 2019; Josset et al., 2017) at around similar densities. However, the urea content of those foams was four times higher than those of the UCNF or UCNF-IONPs foams in this study.

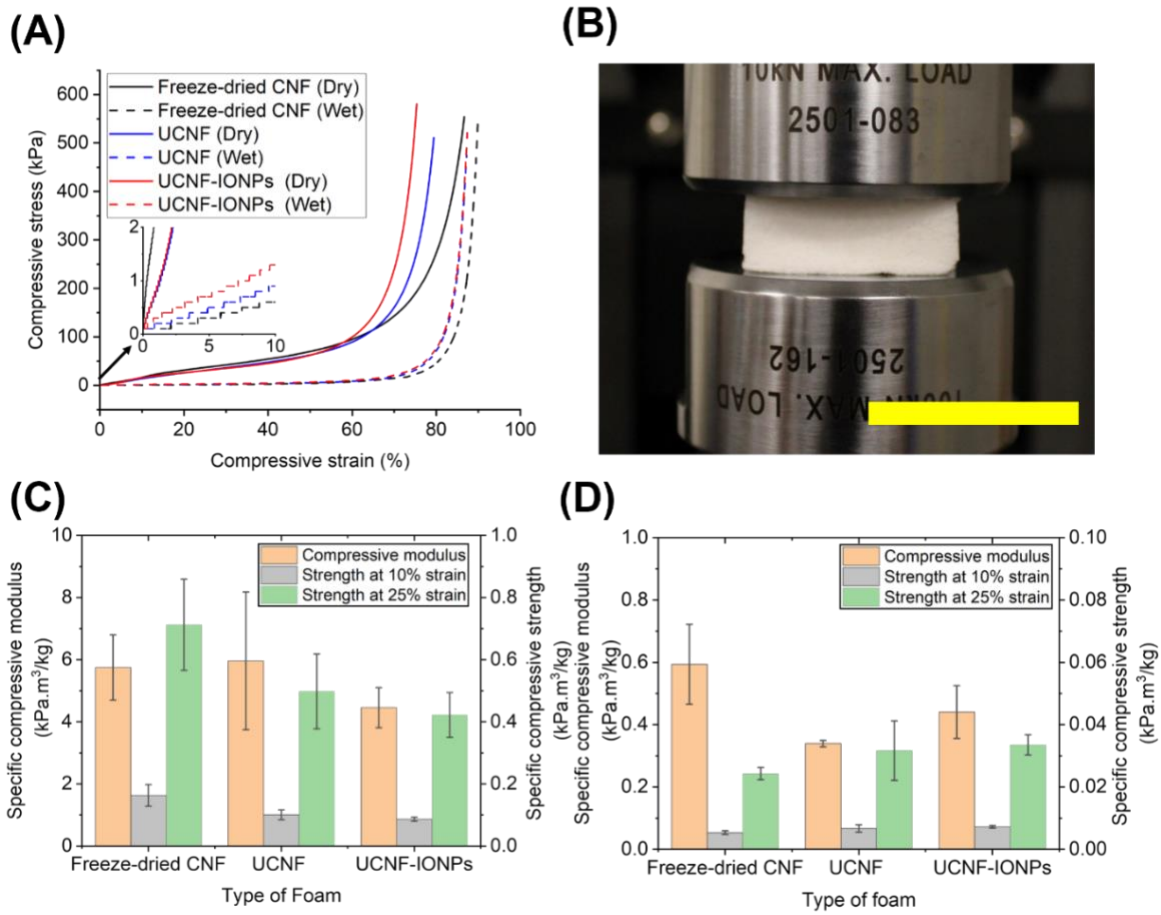

Figure 3.8. Stress-strain curves for both dry and wet foams (A), photo of the experimental set up (Scale bar is 3 cm) (B), specific compressive modulus, compressive strength at 10% and 25% strain for dry (C), and wet (D) foams. The error bars represent one standard deviation among three replicates for each group.

The increased mechanical properties of foams in previous studies (Antonini et al., 2019; Josset et al., 2017) may be caused by factors other than their higher urea content, such as their

varied supply of raw materials or testing conditions, including different loading or test speed. On the other hand, all the wet foams showed a considerable drop in both compressive moduli and strengths (Figure 3.8D) compared to dry samples. The freeze-dried CNF foams had a statistically higher specific compressive modulus than the UCNF and UCNF-IONP foams. The specific compressive strength of the wet freeze-dried foam at 10% strain was not statistically different from the wet UCNF and UCNF-IONP foams. But at 25% strain, the wet freeze-dried foam showed a statistically lower compressive strength than the wet UCNF-based foams. Overall, the mechanical performance of foams produced by microwave-assisted method is comparable to that produced by freeze-drying. A summary of the compressive testing results is presented in Table B1.

3.5 Conclusions

Freezing followed by instantaneous thawing-drying of a CNF-urea suspension produced low density (36 kg/m^3) CNF foams. A 15 wt.% urea content was sufficient to produce these foams, which is significantly less than what was used in prior research. Instantaneous thawing has been identified as a crucial factor in the production of CNF foams with low density and limited shrinkage. The microscopic images revealed that the foams formed at a slow freezing rate had pores with a uniform shape. Intriguingly, fast freezing in a freezing chamber or with liquid nitrogen resulted in either the formation of voids in the foam structure or total CNF agglomeration. Due to the presence of heat-induced in-situ carbamate crosslinking, the foams exhibited a favorable degree of stability in water. This feature was not altered by the hybridization of the CNF foams with IONPs. This study demonstrates the potential for large-scale, continuous manufacturing of nanocellulose-based porous foams at a lower cost and a lower energy consumption than any previously reported methods, thereby enhancing the viability of this porous material as a component of widely available commercial products.

CHAPTER 4

3D PRINTING OF CELLULOSE NANOFIBRILS ENABLED BY MICROWAVE TECHNOLOGY

4.1 Chapter summary

Cellulose nanofibril (CNF) is a sustainable nanomaterial that has a tremendous potential to replace synthetic polymers in additive manufacturing/ 3D printing. However, there are several challenges, such as preferably complex processing route and time and energy intensive drying, that still need to be overcome before extensively adopting this material in 3D printing applications instead of non-sustainable synthetic polymers. Herein, a novel CNF-based 3D printing technique using CNF paste (11.3 to 13.5 wt.% solids content) and urea and carboxymethyl cellulose (CMC) as additives has been reported. The amplitude-sweep tests and zeta potential analyses clearly showed that the rheological characteristics of the paste are significantly influenced by the addition of urea (25 and 50 wt.%) and CMC (1 and 2 wt.%). A notable improvement was observed in extrusion performance and printability when added with additives in comparison to CNF pastes without additives. Two distinct multilayer geometries were constructed, namely octagonal shells and single-shell cuboids with 100% infill. These structures were later solidified by freezing and rapidly dried through microwave irradiation. Samples containing 50 wt.% urea and 1 wt.% of CMC, had the lowest amount of volumetric shrinkage (~31%). The compressive properties of the samples were assessed. The results indicated that structures containing 2 wt.% CMC exhibited higher compressive strength than the structures with 1 wt.% CMC, regardless of the urea concentration. Intriguingly, a higher CMC content also positively influenced interlayer adhesion along the printing direction, thereby increasing the tensile strength of the structures. In addition, a thorough investigation of the chemical interactions among CNF, urea, and CMC was conducted using Fourier-transform infrared spectroscopy (FTIR). This distinct approach for 3D printing, based on the use of CNFs and microwave irradiation, provides an economically viable option to promote sustainable nanomaterials in the field of additive manufacturing and pave the way for further development.

4.2 Introduction

3D printing has become a paramount technology in manufacturing, allowing for the efficient production of diverse products. This state-of-the-art technique can handle a wide variety of materials, such as polymers, composites, metals, and ceramics, and is attained by the process of depositing materials in a sequential manner enabling the construction of complex and sophisticated structures and geometries (Gross et al., 2014; Velu et al., 2019). As a result, 3D printing has been extensively used in different industries such as packaging (Tracey et al., 2022), construction (Velu et al., 2019), energy storage (Zhang et al., 2017), biomedical (Bozkurt & Karayel, 2021), and environmental (Tan et al., 2023) sectors.

The main factors that contribute to the adoption of 3D printing technology over traditional production processes, such as welding, casting, milling, or molding, are its ability to be cost-effective, time-efficient, structurally precise, and reproducible (Jungst et al., 2016; Li et al., 2015). The widespread utilization of computer-aided design, together with advanced machine learning and artificial intelligence technologies, enhances this technology's appeal by providing a high level of automation and flexibility.

Cellulose is the most abundant source of biopolymers found naturally in plant cell walls. Cellulose-based nanomaterials are set to be widely used to replace plastic-based non-sustainable polymers due to their unique characteristics, which include a high degree of abundance, biodegradability, a wide range of chemical modifications, and desirable mechanical properties (Moon et al., 2011; Trache et al., 2020). Several types of cellulosic nanomaterials exist, with cellulose nanofibrils (CNFs) being the most prevalent type that are prepared mechanically through size reduction and refining (Moon et al., 2011). Chemical modifications produce a few other forms, including cellulose nanocrystals (CNCs), and 2,2,6,6-tetramethylpiperidine-1-oxyl (TEMPO)-oxidized CNF. CNFs are the most economical form of cellulose nanomaterials in terms of production expenses.

Cellulose nanomaterials represent a highly promising choice for recyclable composite materials with significant potential in the realm of 3D printing technology. Depending on their intended uses, several derivatives such as CNF, CNC, TEMPO-CNF, and others can function as either rheological modifiers or mechanical reinforcements (Yadav et al., 2021). To date, chemically modified CNFs have been regarded as the primary focus for main building block in extrusion-based 3D printing research. Furthermore, in many cases, the CNFs are combined with supplementary agents to augment mechanical robustness, aid smooth printability, or induce chemical crosslinking to enhance wet stability, consequently increasing the overall expense of material preparation for 3D printing application.

Structures crafted from water-based pastes must undergo a drying phase while retaining their original shape. Freeze-drying is a commonly used method for this purpose (Baniasadi et al., 2021); nevertheless, it is infamous for its significant energy consumption and time requirements, often lasting between 24 to 48 h. Therefore, for large-scale applications, this approach is deemed unsuitable.

A low concentration (3 wt.%) of CNF proves to be suboptimal for 3D printing applications. The primary reason for this is the higher water content, which disrupts the printing process by allowing water to drain out of the material. This leads to issues with over/under extrusion through the nozzle. Furthermore, structures produced with such low CNF concentrations do not possess the required mechanical stability for the formation of multilayer structures that is attributed to a relatively low viscosity. Recent studies have investigated the use of carboxymethyl cellulose (CMC) to improve the water retention of CNFs while altering their rheological properties. Azark et al. (Azrak et al., 2021) utilized a high CNF concentration (~23.5 wt.%) combined with CMC at a CMC:CNF ratio of 0.1:1 to produce a paste of approximately 18 wt.%. Their research showed that the addition of CMC with a high CNF concentration enabled the continuous extrusion of wet fibrils using a single-screw extruder. Upon further drying, a recyclable CNF-based cord was produced.

A later investigation conducted by the same research group also demonstrated the production of wet/dry sheets using the of CMC as a processing aid with CNF (Azrak et al., 2020).

Thibaut et al. (Thibaut et al., 2019) used dried short natural cellulose fibers with CMC for making a high solid content paste (42 wt.%) to create 3D printed multilayered structures. These structures were dried using either air drying or immersion in an ethanol solution. Nevertheless, both approaches resulted in significant height shrinkage (41%), and the air drying (48 h) remained time-consuming and inefficient.

Urea has been proved to be crucial for enhancing dissolution of cellulose by creating a layer of urea-hydrate inclusion complexes with cellulose (Cai & Zhang, 2005; Fauziyah et al., 2019). Molecular dynamic simulations have previously indicated that upon freezing, urea alters a major portion of the hydrogen bonding from cellulose-water to cellulose-urea by creating more free water in the structure (Cai et al., 2012). Expanding upon this idea, we have recently implemented an innovative technique for manufacturing lightweight hybrid CNF foams, resulting in notable enhancements in terms of affordability and efficiency by substituting conventional freeze-drying method with microwave irradiation (Rahman et al., 2023). In short, that study has demonstrated that molding and freezing of 2 wt.% CNF suspension with urea facilitates rapid drying through microwave irradiation.

While there has been numerous research on cellulose-based 3D printing methods, most use costly chemically modified cellulose components such as TEMPO-CNF as the main constituents. Notably, the drying methods in many of these studies involve freeze-drying, solvent exchange, or oven drying, all of which require a substantial amount of time and energy. Consequently, these technologies are not ideal for large-scale production.

This work investigated the 3D printing with CNFs as the primary component and utilizes urea and CMC as processing aids. Additionally, rapid drying was achieved using microwave irradiation. The analysis involved assessing the paste rheology and surface charge properties of CNFs to determine the most optimal formulation for smooth printability. The overall printing

process was optimized by fine-tuning different printing parameters. Two distinct types of multilayered geometric structures, octagonal shells and single-shelled 100% infill grid cuboids were printed, and the volumetric shrinkage of the cuboids was determined. Additionally, comprehensive analyses of both compressive and tensile properties were conducted to gain insights into layer adhesion with varying urea-to-CMC ratios. FTIR analyses were performed to understand the chemical interactions among CNF, urea, and CMC in dried samples. Overall, this study demonstrates an energy-efficient extrusion-based additive manufacturing process that is environmentally friendly and sustainable.

4.3 Experimental section

4.3.1 Materials

The cellulose nanofibrils (CNFs) used in this work were provided by the University of Maine Process Development Center (PDC) in Orono, Maine, USA. A chemically processed and purified softwood pulp, known as bleached softwood kraft pulp, was used to attain a fine content of 90%. Fine content refers to the proportion of fibers having a length $\leq$ 200 μm. The CNF suspension was produced at a concentration of 3 wt. %. To achieve a 20 wt. % of CNF suspension, a mechanical pressing method was utilized to increase its consistency. Urea (NH_2CONH_2; 99.0-100.5%) was obtained from Sigma-Aldrich, MO, USA. Carboxymethyl cellulose sodium salt (CMC) (with an approximate degree of polymerization of 500) was obtained from Tokyo Chemical Industry Co., LTD., Tokyo, Japan. All the reagents utilized in this study were of analytical grade and used without further purification.

4.3.2 Paste preparation

CNF suspension was used to generate six different paste formulations by combining CNFs, urea, and CMC. The concentrations of urea (25 and 50 wt.%) and CMC (1 and 2 wt.%) were varied in relation to the dry mass of CNFs. The procedure encompassed two stages: In one portion of water, the specified quantity of urea for a particular paste formulation was added at room temperature, creating an aqueous solution. Concurrently, in a separate portion of water, a

specified quantity of dry CMC powder was introduced at a temperature of 65 °C with continuous agitation. Upon complete dissolution of CMC, the solution was allowed to cool to room temperature. Afterwards, both solutions were simultaneously added to a 20 wt.% CNF suspension to reduce its concentration to 11.3–13.5 wt.% CNF. This was accomplished by utilizing high-shear mixing for 30 minutes, using a KitchenAid Artisan Quart Tilt-Head Stand Mixer (Benton Harbor, MI, USA). Finally, the resultant pastes were tightly packed in Ziplock bags to be stored at room temperature until they were used in the future. The paste formulation summary is presented in Table 4.1.

Table 4.1 Formulations of CNF paste with and without urea and CMC in a unit of part per hundred (pph), including solid contents (for 100 g of dry CNF)

Paste-composition (CNF–Urea–CMC) (pph)	CNF (g)	Urea (g)	CMC (g)	Final solids content (%)
100–0–0	100	0	0	9
100–25–0	100	25	0	11.3
100–25–1	100	25	1	11.3
100–25–2	100	25	2	11.3
100–50–1	100	50	1	13.5
100–50–2	100	50	2	13.5

4.3.3 Extrusion-based 3D printing & process optimization

The pastes listed in Table 4.1 were inserted into the cylindrical tube of a extrusion-based 3D printer (3D Potter, Stuart, FL, USA). The paste was gently pressed to eliminate any air pockets within the tube. This 3D printer can move in both horizontal and vertical directions, owing to its inbuilt motors. At the bottom of the cylindrical tube, there is an opening that allows for the connection of brass nozzles of different diameters. For all 3D printing experiments in this study, a nozzle diameter of 7 mm was consistently used. In this study, two distinct structure types were created using manually designed G-codes. The first one consisted of regular octagonal shells,

which were made up of eight layers and had sides of 4 cm. The second one consisted of grid cuboids with a single shell and 100% infill, with sides measuring 3.5 cm. It is important to mention that 400 grit sandpaper was used as the substrate for all printing tasks for added convenience and adhesion of the print to the bed. Table C1 contains detailed information on the optimized printing process parameters. After printing, the produced structures were placed in a conventional freezer at -20 °C for at least 12 h. To carry out the subsequent drying procedure, we used an LG LMC1575 microwave oven (LG Electronics Inc., Seoul, South Korea) with a power input of up to 1200 W. Distinct microwave drying optimizations were required for octagonal shells and cuboids due to their structural differences. For octagonal shells, an initial input of 1200 W of power for a duration of 2 min was followed by 3 min of heating at a power of 360 W, with 1 min intervals between each minute. However, in the case of cuboids, an energy input of 1200 W was supplied for a duration of 3 min, followed by a heating period of 4 min with 1 min interval at the same energy input. To prevent over-drying or burning, the final water content of the structures was maintained at approximately 10-12%. Afterwards, the structures were placed in room temperature with adequate airflow for at least 12 h to further reduce the moisture content.

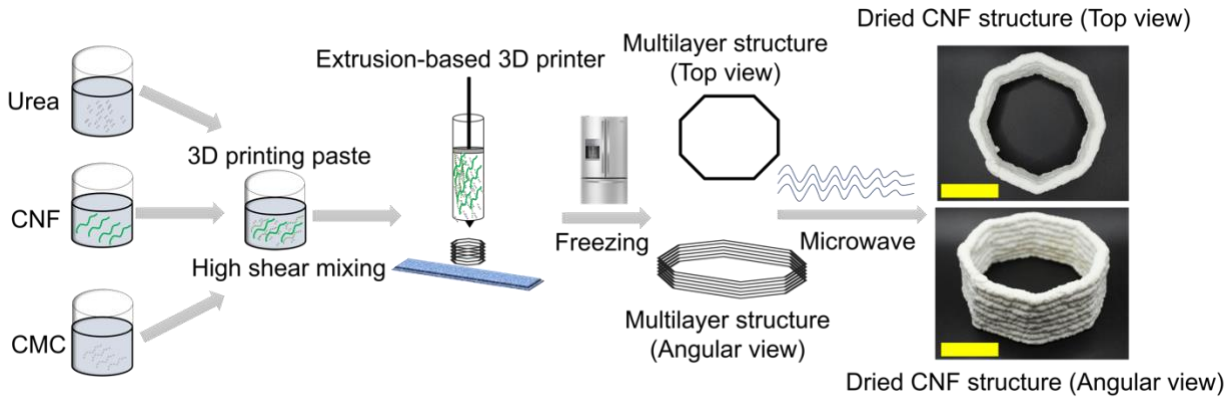

Figure 4.1. Schematic illustration of the formation of microwave-dried structures using CNF-based 3D printing (Scale: 5 cm)

Finally, all the structures were subjected to conditioning at a relative humidity of 50 ± 2% and a temperature of 23 ± 2 °C, for a duration of 24 h before further quantitative testing and

measurements. Figure 4.1 provides a visual representation of the complete 3D printing procedure. Finally, all the structures were subjected to conditioning at a relative humidity of 50 ± 2% and a temperature of 23 ± 2 °C, for a duration of 24 h before further quantitative testing and measurements. Figure 4.1 shows a visual representation of the complete 3D printing procedure.

4.4 Characterization

4.4.1 Rheological characterization

A Discovery HR-2 oscillating rheometer (TA Instruments, New Castle, DE, USA) was used to evaluate the rheological characteristics of the CNF-based pastes. The analysis was carried out at a temperature of 23 ± 0.5 °C with ~0.2 grams of the pastes placed on an 8 mm parallel plate fixture with a 1000 μm gap. Through amplitude sweeps at a frequency of 10 Hz, encompassing a shear stress range of 10 to 10,000 Pa, the storage and loss modulus of the pastes were measured. The yield stress of the pastes was calculated as the applied stress at the point of intersection between the storage modulus, G', and the loss modulus, G".

4.4.2 Volumetric shrinkage analysis

Volume assessments were carried out to compare the volumes of 100% infill single-shelled grid cuboids at different stages. Three stages were compared: after printing, after freezing, and after drying. Equation 4.1 was used to calculate the volumetric shrinkage % by contrasting the estimated printed volume (V_1) with the post-conditioned dry volume (V_2):

$$\text{Volumetric shrinkage (\%)} = \frac{V2}{V1} \times 100 \quad (4.1)$$

4.4.3 Microscopic analysis

The morphology of the dried structures was investigated using a Zeiss NVision 40 scanning electron microscope (Carl Zeiss AG, Oberkochen, Germany). Thin slices with a thickness of 2-4 mm were cut from the cross sections of the cuboid samples and attached to a double-sided carbon tape for observation. A few millimeters from either of the failed specimen layers from the tensile tests were similarly attached to a double-sided carbon tape for the

investigation of tensile failures between two layers. All specimens were sputter coated with a 6 nm gold-palladium layer, and a fixed electron high tension voltage of 3 kV was maintained for all measurements.

4.4.4 Zeta potential analysis

Using a Nano ZS90 Zetasizer (Malvern, UK), the zeta potential of several paste formulations was assessed. In each case, 50 mL of a 0.001 wt.% suspension was prepared with a 30-second ultrasonication. The suspension's pH was adjusted to range between 6.4 and 6.6. The upper part of the suspensions was collected and used for all measurements after allowing the suspensions to settle for 30 minutes. Each sample was subjected to six replications, and the results are presented as an average value with standard deviation.

4.4.5 FTIR analysis

A Spectrum Two FTIR spectrophotometer (PerkinElmer, Waltham, MA, USA) was used to study the chemical interactions among CNF, urea, and CMC within the dried structure. The wavenumber 1055 cm^{-1}, which reflects the stretching vibration of the cellulose backbone and is unaffected by chemical reactions, was used to normalize all of the FTIR spectra (Zhang et al., 2012).

4.4.6. Mechanical analysis

Using an Instron 5942 machine (Instron Corporation, Norwood, MA, USA) equipped with a 500 N load cell, the compressive and tensile properties of the dried structures along the z-axis were evaluated. A modified ASTM C165 standard procedure was used, and the testing speed was set to 0.89 mm/min. From 4-layer 100% infill shells, cuboid samples with dimensions of 2.5 cm $\times$ 2.5 cm $\times$ 2.0 cm were used for the compression tests. The modulus of elasticity was estimated using the linear elastic region of the corresponding stress-strain curve, and the compressive strengths were calculated at two distinct strain levels (10% and 25%). All data were normalized according to the respective densities for each type of specimen. Tensile tests were performed

along the z/printing direction to assess the adhesion and inter-layer strength. A modified ASTM D638 Type V method was used for the tensile testing. A FSL Muse Core Desktop CO2 Laser Cutter (Sandhill Road, Las Vegas, NV) was used to cut dog bone-shaped specimens from the sides of the dried 8-layer octagonal shells. These specimens had a gauge length of 1 cm and a total length of 3.5 cm. A constant test speed of 1 mm/min was used throughout all tests.

4.4.7. Statistical analysis

To determine the statistical significance among various dependent variables, one-way analysis of variance (ANOVA) was used. To assess the precise differences between the pairs of means, Duncan's Multiple Range Test (DMRT) was performed as a post hoc test. All the analyses with a 95% confidence interval were carried out using IBM SPSS Statistics 25 software (Armonk, NY, USA).

4.5 Results and discussion

4.5.1 Optimization of the paste formulation for multilayer structure

To optimize the formulation of CNF-based pastes to use in multilayer 3D printing applications, it was necessary to evaluate the printability and extent of shrinkage of the resulting structures in relation to the solid contents of the pastes and their composition. Figure 4.2A depicts the top and side views of an eight-layer regular octagonal shell following the drying process. It is noticeable that the structure without the addition of urea and CMC does not retain its shape after drying whereas all the structures with urea and CMC content retained their shapes.

Before discussing the printability and net-shape production of these structures, it is essential to comprehend the function of each paste component. In each of the four paste formulations, CNFs are the primary component. The addition of urea plays a crucial role in preserving the shape of the frozen structures during microwave drying as explained in chapter 3. In addition, the incorporation of CMC contributes to achieving a smooth and continuous filament flow by modifying the rheological properties of CNF-urea pastes.

Notably, CNF by itself, without urea and CMC, was incapable of producing any structure. This limitation was attributed to the inability to extrude continuous filaments, which resulted in filament breakage as well as over and under extrusion, causing subsequent layers to collapse. The addition of 25 wt. % urea to CNF improved printability significantly, indicating that the addition of urea to CNF suspensions modifies the rheological properties of CNF pastes.

According to a study by Halonen et al. (Halonen et al., 2017), the addition of urea to water increases the solution viscosity and surface tension. In line with the same study, increasing the temperature above 293.15 K decreases kinematic viscosity, whereas increasing the mass fraction of urea in the solution also increases viscosity. Given that all CNF pastes contain between 86–89 % water, it is expected that the addition of urea will alter the viscosity of the pastes. Although there was a noticeable improvement in the printability of multilayer structures, there were still questions about the reproducibility terms of following the multilayer structures.

The addition of only 1 wt.% CMC improved the 3D printability of the paste, and this improvement was further enhanced when the CMC content was increased to 2 wt.%. CMC acts as a processing aid, effectively reducing friction and entanglements between cellulose fibrils and simultaneously decreasing the viscosity of CNF (Mazhari Mousavi et al., 2017). In addition, the incorporation of CMC improved the water retention capacity of CNF by reducing the phase separation between CNF and water. This effect is due to the system's increased anionic surface charge (Kumar et al., 2017).

Azrak et al. (Azrak et al., 2021; Azrak et al., 2020) reported the production of continuously processed filaments from a CNF + CMC paste with a high solid content (18 wt.%) using a single-screw extruder. The wet filaments were then dried in an oven at 70 °C for one hour to produce dry cords. Even though this study documented the extrusion of CNF + CMC paste, utilizing these filaments in additive manufacturing presented several research gaps. First, the feasibility of constructing multilayered structures with CNF + CMC paste had not been examined. Second, the

use of urea as a processing aid for microwave drying is a novel technique that has previously been employed in CNF-based hybrid foam formation but not assessed for 3D printing application.

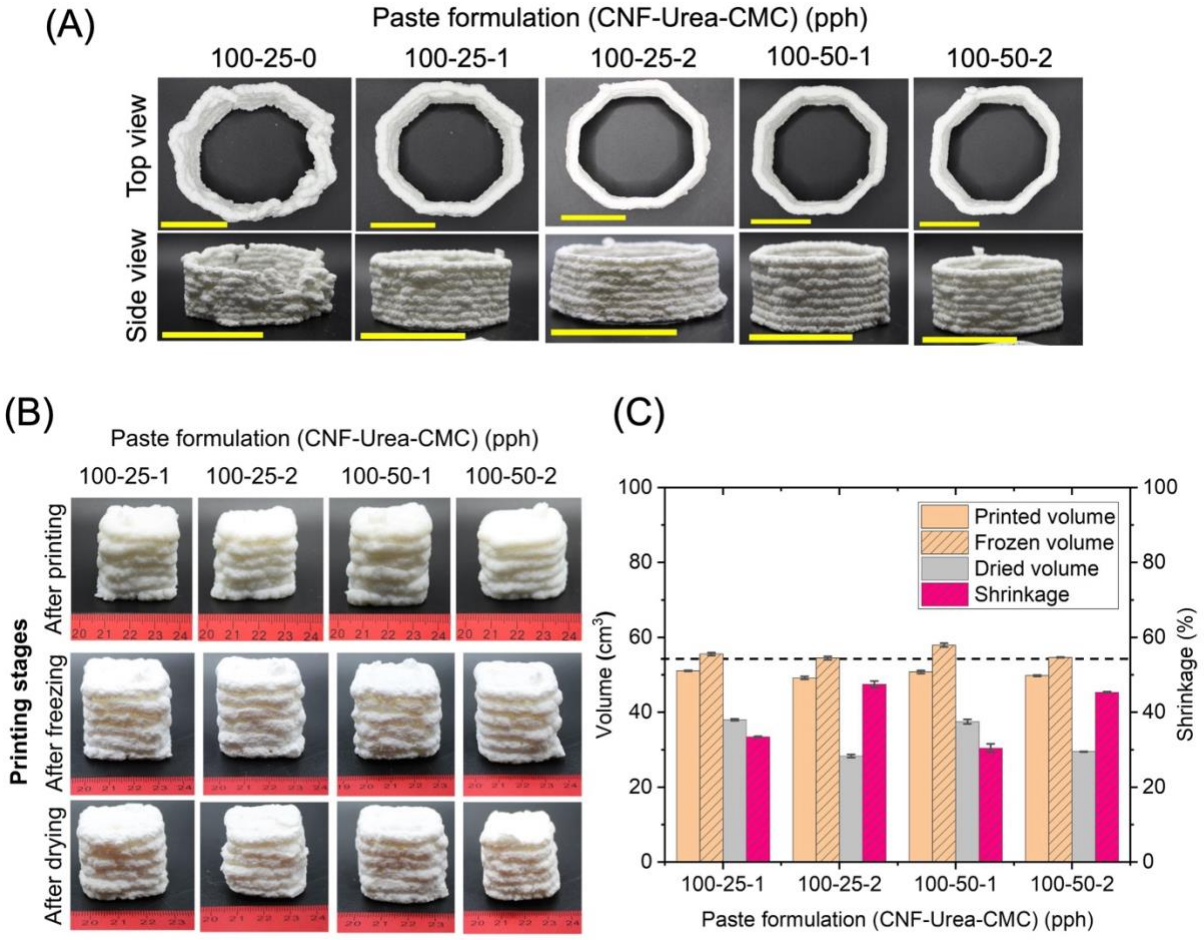

Figure 4.2. Images of multilayer octagons (Top and side views) (Scale bar: 5 cm) (A), cuboid with different printing stages (ruler scale in cm) (B), and volume and shrinkage of structures at three structural conditions with four working paste formulations. The horizontal dashed line represents the estimated printed volume. The error bars indicate one standard deviation among three replications for each group.

Figure 4.2B depicts the cuboid structures in various conditions during their manufacturing process, displaying their relative sizes, while Figure 4.2C displays the quantitative data. On closer inspection, it was discovered that the actual printed volume of the cuboids was approximately 5% less than the estimated printed volume. The estimated printed volume is the calculated volume according to the command provided for 3D printing of the cuboid. This deviation between actual

and estimated printing volume could be attributed to the base layer's interaction with the bed surface, which might cause it to flatten the layer due to the manual adjustment of nozzle to bed distance.

Following the freezing process, the volume of the cuboids increased by approximately 3%. This could be attributed to volume expansion during the phase change from water to ice within the frozen structures, as discussed by Noerdlinger and Brower (Noerdlinger & Brower, 2007).

Nonetheless, the most important finding was that microwave drying of the frozen structures resulted in noticeable shrinkage, regardless of the tested formulation. Although all four paste formulations shrunk in their final dry state, an apparent pattern was found. Structures prepared with formulations containing 2 wt.% CMC shrunk more than those containing 1 wt.% CMC when the ratio of CNF to urea was kept constant.

The formulation "100-50-1" displayed statistically less shrinkage (30.5% $\pm$ 1.1%) and comparable density (0.15 g/cm^3 $\pm$ 0.003 g/cm^3) among all four formulations compared to "100-25-1." Therefore, it is reasonable to conclude that the ratio of urea to CMC significantly affects the net shape of the dried structures.

4.5.2 Morphology of the structures

Figure 4.3A displays SEM images of the surface and cross-sections of microwave-dried structures. A porous nature was observed in both surface and cross-sections, a common occurrence attributed to the random entanglement of misaligned CNFs. The pores on the cross-sections were significantly larger than those on the surface of the structures. Intriguingly, there was no apparent distinction in the cross-sections when various paste formulations were compared. However, the surface of the structures exhibited more prominent wrinkling when the ratio of CMC to urea was higher. The higher CMC content retained more water in the structure, and the direct exposure to microwave irradiation might have caused the cross section to dry more rapidly than the surface, resulting in the observed surface wrinkling.

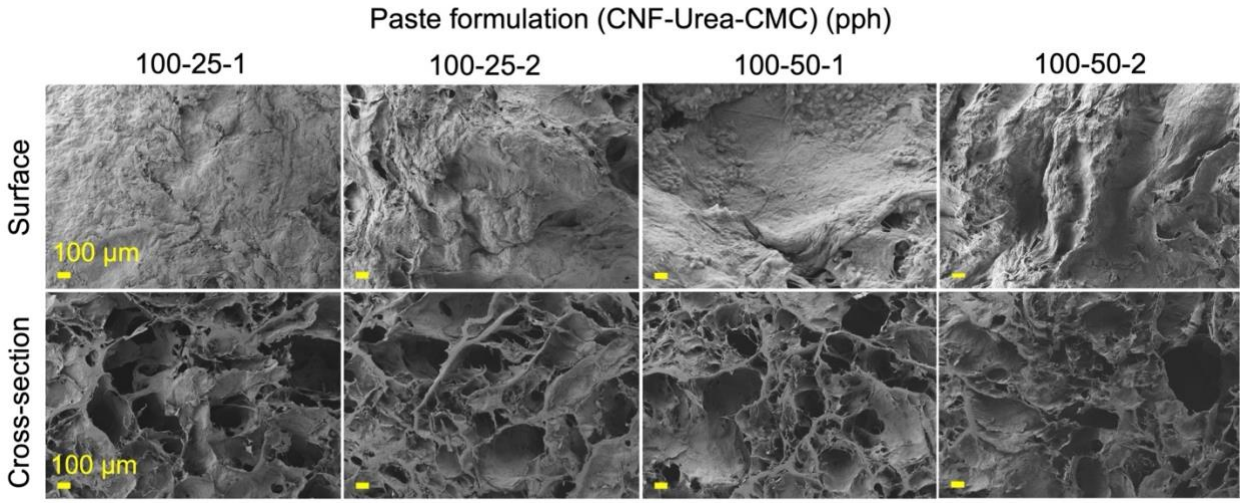

Figure 4.3. Representative SEM images from the surface and cross-sections of dried samples with different paste formulations.

4.5.3 Rheology, printability, and shape retention

Understanding the yield stress (τ_y) is essential for the manufacturing of fiber-based 3D printing process. In extrusion-based printing, a critical stress threshold must be exceeded to initiate the flow of pastes through a particular nozzle diameter. The applied shear stress (τ_{max}) must be greater than the yield stress (τ_y) to initiate the transformation of the polymer paste superstructure into a continuous flow from a static state. Figure 4.4 (A-F) illustrates the results of various paste formulations' stress sweep tests. In every instance, the samples initially exhibited a paste-like or elastic behavior at low shear stress, with the storage modulus (G') exceeding the loss modulus (G"). At higher shear stresses, this behavior was followed by a transition to a liquid-like or viscous state, characterized by the loss modulus exceeding the storage modulus (G" > G').

Quantitatively, the G' for CNF alone, without urea and CMC, was determined to be 248 kPa, which was considerably greater than those for all other formulations. The addition of 25 wt.% urea to the CNF pastes decreased G' to 135 kPa, indicating that urea significantly reduces the capacity to store energy for CNFs. Adding 1 wt.% CMC to CNF pastes containing 25 wt.% urea further decreased the storage modulus to approximately 95 kPa. However, increasing the CMC

content to 1 wt. % with the same amount of urea (25 wt. %) or 2 wt.% with double the amount of urea (50 wt.%) increased the storage modulus to 125 kPa. Intriguingly, increasing the CMC content to 2 wt.% while maintaining the same amount of urea (50 wt.%) resulted in the lowest storage modulus value of 66 kPa, indicating the lowest ability to store energy of all the pastes.

Figure 4.4 (G) represents an illustration of the possible interactions among the components of the paste. As expected, adding only urea to CNF did not render the paste printable, and thus shape retention was not possible. Although the addition of urea to CNF paste modifies its rheology by decreasing τ_y, its primary function is to make it microwave-dryable. To elaborate, at low temperature the hydrogen bonding alteration creates an inclusion complex with urea around cellulose fibrils (Cai et al., 2012). Recently, this idea was successfully utilized in production of molded hybrid-CNF foams using microwave irradiation (Rahman et al., 2023). According to this work, the addition of 25 wt. % urea led to the highest shape retention and the least amount of deformation. Although the addition of CMC alone to CNF renders the paste printable, the absence of urea led to the aggregation of CNF and, consequently, prevented shape retention upon microwave drying. Therefore, both urea and CMC are required for printability and shape retention after microwave drying. There is, however, a ratio that provides optimal printability as well as the greatest volume/shape retention. From the previously discussed volume and shrinkage results, the “100-50-1” formulation met these criteria with statistically highest volume retention and the lowest shrinkage among the four formulations. The competitive interactions among CNF, urea, and CMC might play a significant factor here. Table 4.2 provides a summary of the rheology results.

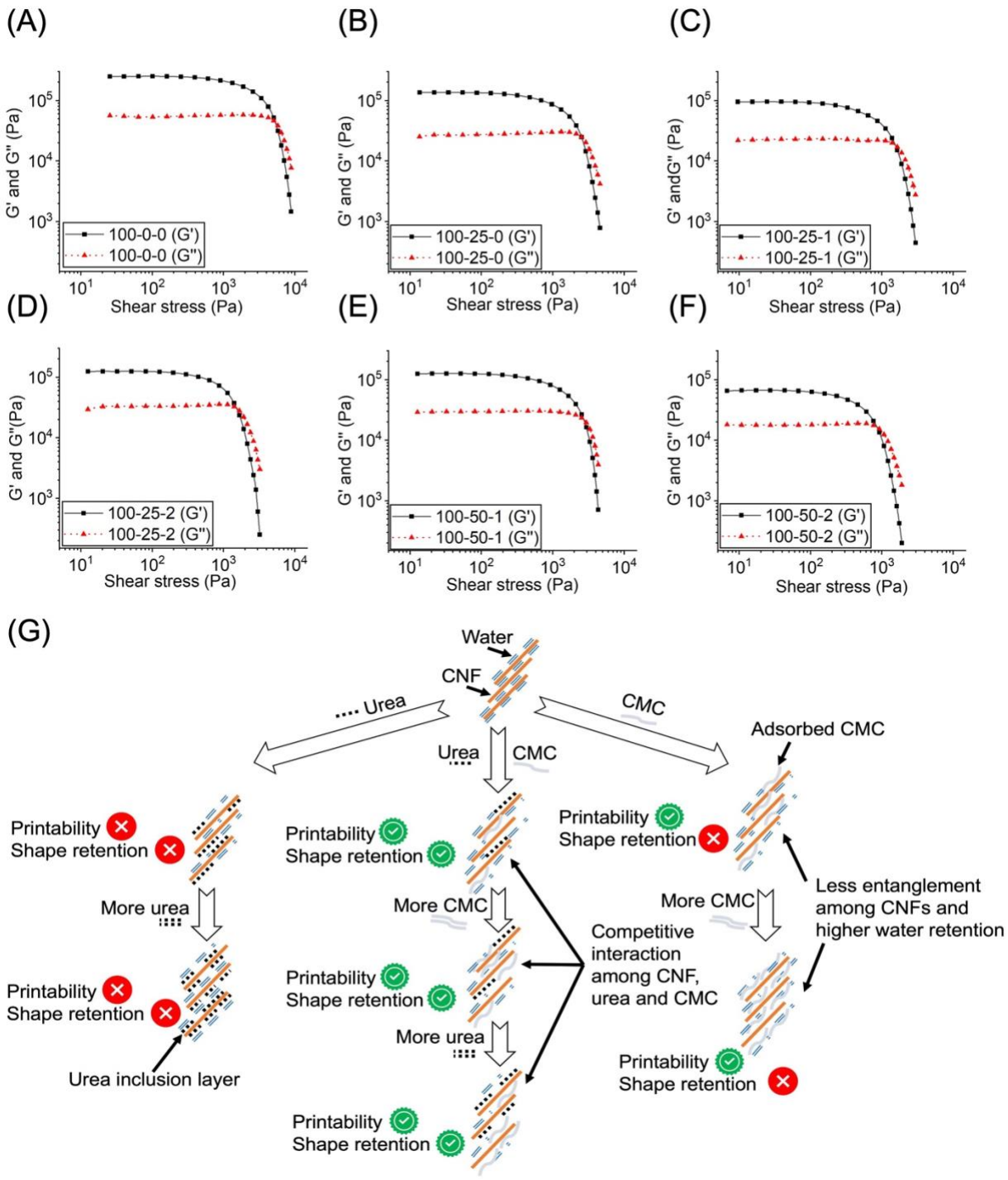

Figure 4.4. Amplitude-sweep test at a fixed angular frequency of 10 Hz for different paste formulations (A-F) and a schematic diagram illustrating the interactions among paste components, printability, and shape retention (G).

Through zeta potential measurements, the surface charge of CNF was initially measured at -38.0± 1.9 mV (Table 4.2). Nonetheless, it is well-established that CMC significantly interacts with and adsorbs onto the cellulose surface, resulting in an overall increase in anionic charge and a reduction in mechanical entanglement by increasing water retention capacity (Kumar et al., 2017). In terms of the nature of the surface charge, urea is a neutral but highly polar molecule. This does not preclude the formation of intermediate positive/negative charge species upon dissociation in water or interaction with CMC and CNF. Due to the addition of 25 wt.% urea, the surface negative charge of CNF increased to -40.9 ± 1.5 mV. Adding 1 wt.% CMC, however, significantly decreased this value to -31.6 ± 0.6 mV. As the CMC content increased while the CNF to urea ratio remained constant (Table 4.2), the surface negative charge of the pastes increased as well. Additionally, it was mentioned previously that urea forms an inclusion complex around cellulose fibrils, with this complex forming to a greater extent at temperatures below room temperature. Therefore, it is reasonable to assume that CMC interacts with CNF at room temperature and increases its surface negative charge. When the amount of urea increases in a system containing the same amount of CMC, it is possible that CMC's adsorption is hindered by the higher concentration of urea, which competes with CNF to form urea-hydrate complexes and engages in hydrogen bonding/van der Waals interactions with water (Huber et al., 2016; Rezus & Bakker, 2006). Adding more CMC to the system may partly mitigate this issue. Consequently, this competition between CMC and urea for interaction with CNF is likely to influence the overall paste rheology, surface charge, and shape retention of the structures upon microwave drying.

Table 4.2. Summary of rheology and zeta potential with different paste formulations

Paste-composition (CNF-Urea-CMC) (pph)	Storage modulus, G' (kPa)	Loss modulus, G'' (kPa)	Yield stress, τ_y (kPa)	Zeta potential (mV)	Printability (Yes/No)
100-0-0	250.4	57.7	4.9	-38.0 (±1.9)	No
100-25-0	135.3	30.4	2.2	-40.9 (±1.5)	No
100-25-1	124.6	35.4	1.8	-31.6 (±0.6)	Yes
100-25-2	95.1	23.3	1.5	-48.2 (±1.0)	Yes
100-50-1	125.9	30.4	2.8	-38.5 (±1.3)	Yes
100-50-2	66.5	19.0	0.9	-46.6 (±2.5)	Yes

4.5.4 Mechanical properties

To evaluate the mechanical properties of the dry samples, both compression and tensile testing were conducted. Figure 4.5A illustrates the compressive stress-strain curves for all four printable formulation samples. The curves displayed a linear elastic region, a plateau region, and a densification region, as is typical for compression tests of cellular solids (Gibson & Ashby, 1997). Previous studies (Müller et al., 2022; Siqueira et al., 2017), it was observed that the direction in which the load is applied is a crucial factor for evaluating the mechanical properties of 3D-printed structures. Depending on the print (Z-axis) and fiber direction (XY-axis), the mechanical properties vary significantly, with the anisotropy effect generally producing higher compressive strength along the fiber direction 12/15/2023 5:39:00 PM. To comprehend the compressive/tensile properties of this study, all samples were tested in the direction of the print (Figure 4.5B).

Depending on the sample, all stress-strain curves gradually increased between 23-33% until they reached the maximum force. It is important to note that samples containing 1 wt. % CMC had a statistically higher density (0.19 g/cm^3) than samples containing 2 wt.% CMC (0.15 g/cm^3). To determine whether CMC content is a crucial factor influencing the mechanical properties, all results were normalized with respect to their corresponding densities. The data revealed that samples with a higher CMC content had statistically greater compressive strength at both 15% and 25% strain, indicating that CMC content has a substantial effect on compressive properties (Figure 4.5C).

Multilayered structures were subjected to tensile tests to determine how the formulations affected the adhesion between layers. Similar to the compression test, the density-normalized tensile strengths exhibited a similar trend. The samples containing 2 wt.% CMC had statistically greater tensile strengths than those containing 1 wt.% CMC (Figure 4.5D). This indicates that the inter-layer adhesion along the print direction (Z-axis) improves as the urea-to-CMC ratio isdecreased. Table C2 provides a summary of the mechanical testing outcomes.

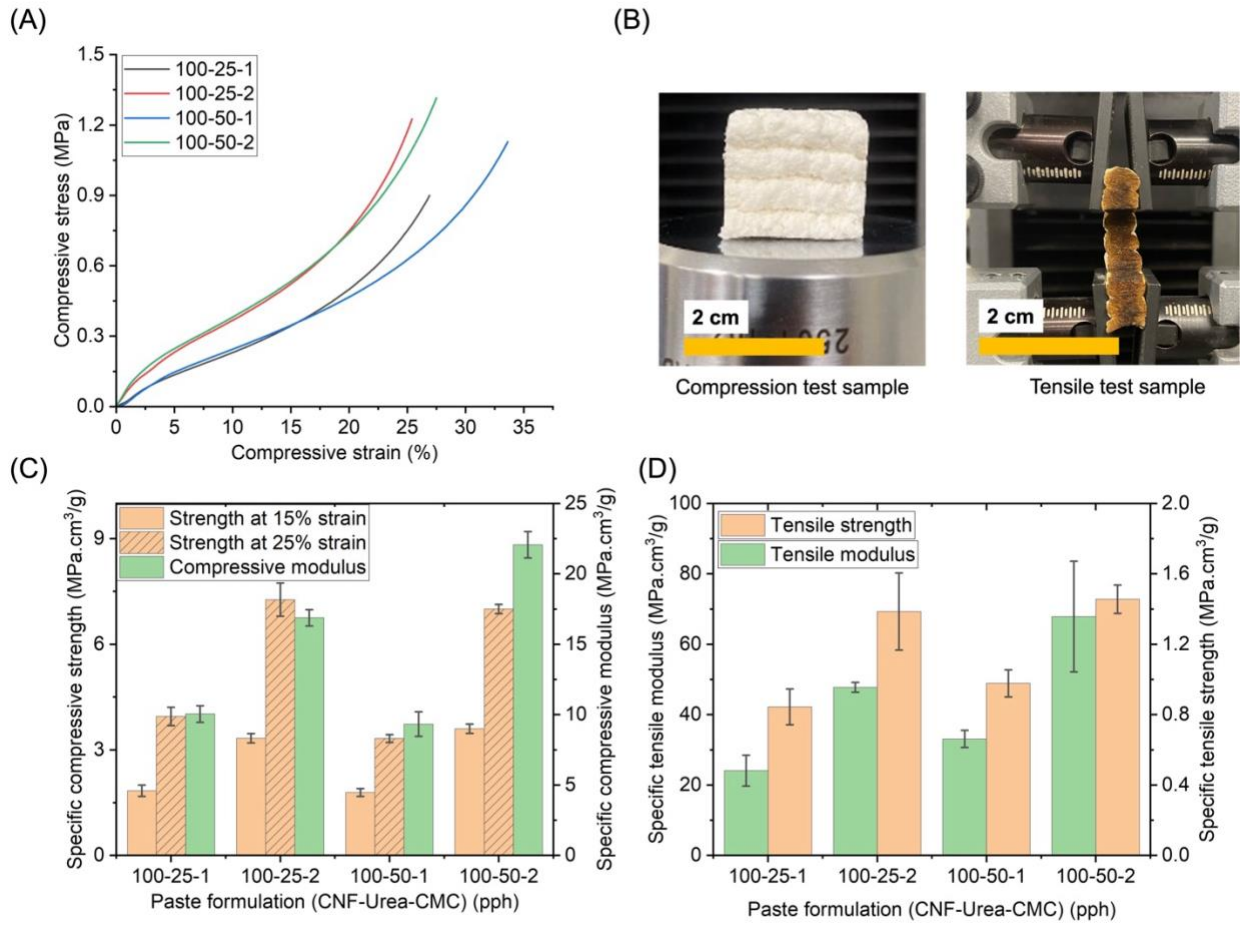

Figure 4.5. Compressive stress-strain curves for dried structures (A), images for both compression and tensile test samples (B), specific compressive (C) and tensile properties (D) of structures. The error bars represent one standard deviation among three replicates for each group.

To evaluate this phenomenon, SEM images of broken tensile samples were captured (Figure 4.6). The representative SEM images displayed a recognizable pattern. The two formulations (“100-25-1” and “100-50-1”) with a lower CMC content exhibited a greater extent of defibrillated surface (yellow region) compared to a fibrillated interface (green region) where more fibrils protruded from the structure because of the tensile forces.

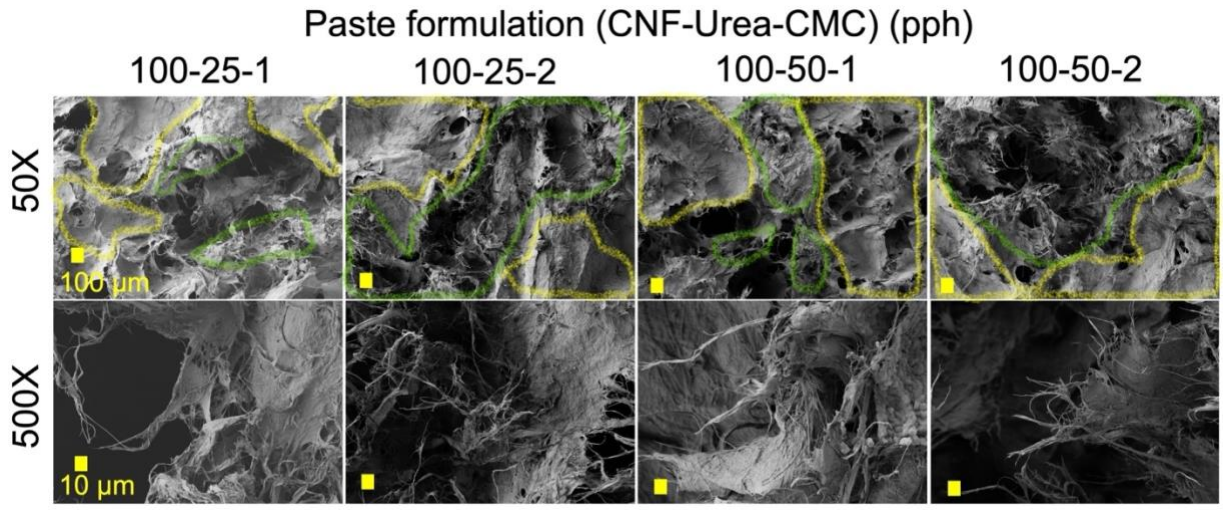

Figure 4.6. Tensile failure analysis for 3D-printed structures in two different magnifications (50X and 500X). Yellow and green regions represent the structure surface and interface, respectively.

In contrast, formulations with a higher CMC content ("100-25-2" and "100-50-2") demonstrated the opposite effect. At a higher magnification (500X), all four samples exhibited fiber entanglement and infusion, which may have resulted from crosslinking via heat-induced ester bonds due to the formation of cellulose carbamate which will be discussed in next section. Consequently, it is evident that the ratio of urea to CMC in the system significantly affected both the compression and tensile behaviors.

4.5.5 FTIR analysis and possible chemical interactions

Figure C3 depicts the FTIR spectra of the structures after drying. All of the samples displayed typical cellulose peaks at 3335 cm^{-1} and 2899 cm^{-1}, corresponding to -OH and -CH stretching, respectively (Hospodarova et al., 2018). These peaks were present in all CNF/CMC-associated samples. Figure 4.7A and B depict the fingerprint regions of the corresponding FTIR spectra. All samples exhibited peaks at 1368 cm^{-1}, 1429 cm^{-1}, 1335 cm^{-1}, and 1055 cm^{-1}, which correspond to the bending and stretching of $-CH_2$, -CH, -OH, and the C-O backbone in cellulose (Aguayo et al., 2018). Also, pure CNF exhibited a weak peak at 1645 cm^{-1}, most likely attributable to the -OH group of adsorbed bound water (Poletto et al., 2011). Due to the asymmetric stretching

of the carboxylate (COO^-) group, neat CMC displayed a sharp peak at 1591 cm^{-1} (Eyholzer et al., 2010; Onyianta et al., 2018). Expectedly, the intensity of this peak was higher in the structures with 2% CMC than 1% CMC. However, urea also exhibited a sharp peak at 1591 cm^{-1} due to both C=O stretching and $-NH_2$ bending (Fischer & McDowell, 1960). Consequently, the peak at this wavelength may be the result of the presence of both residual urea and CMC in the structures. Peaks at 1655 cm^{-1} and 1538 cm^{-1} correspond to amide I (C=O stretching, CONH) and amide II, respectively (Azrak et al., 2020). At 1450 cm^{-1}, all samples exhibited peaks or shoulders attributable to the C=N bonds in resonance structures of urea, which may also have been caused by the crystallization of residual urea in the system. Sharp peaks were observed at 1735 cm^{-1} indicates the carbonyl group of cellulose esters formed between urea and cellulose upon heating (Fei et al., 2017; Guo et al., 2010; Jandura et al., 2000). Figure 4.7C depicts the potential interactions between CNF, urea, and CMC under microwave irradiation.

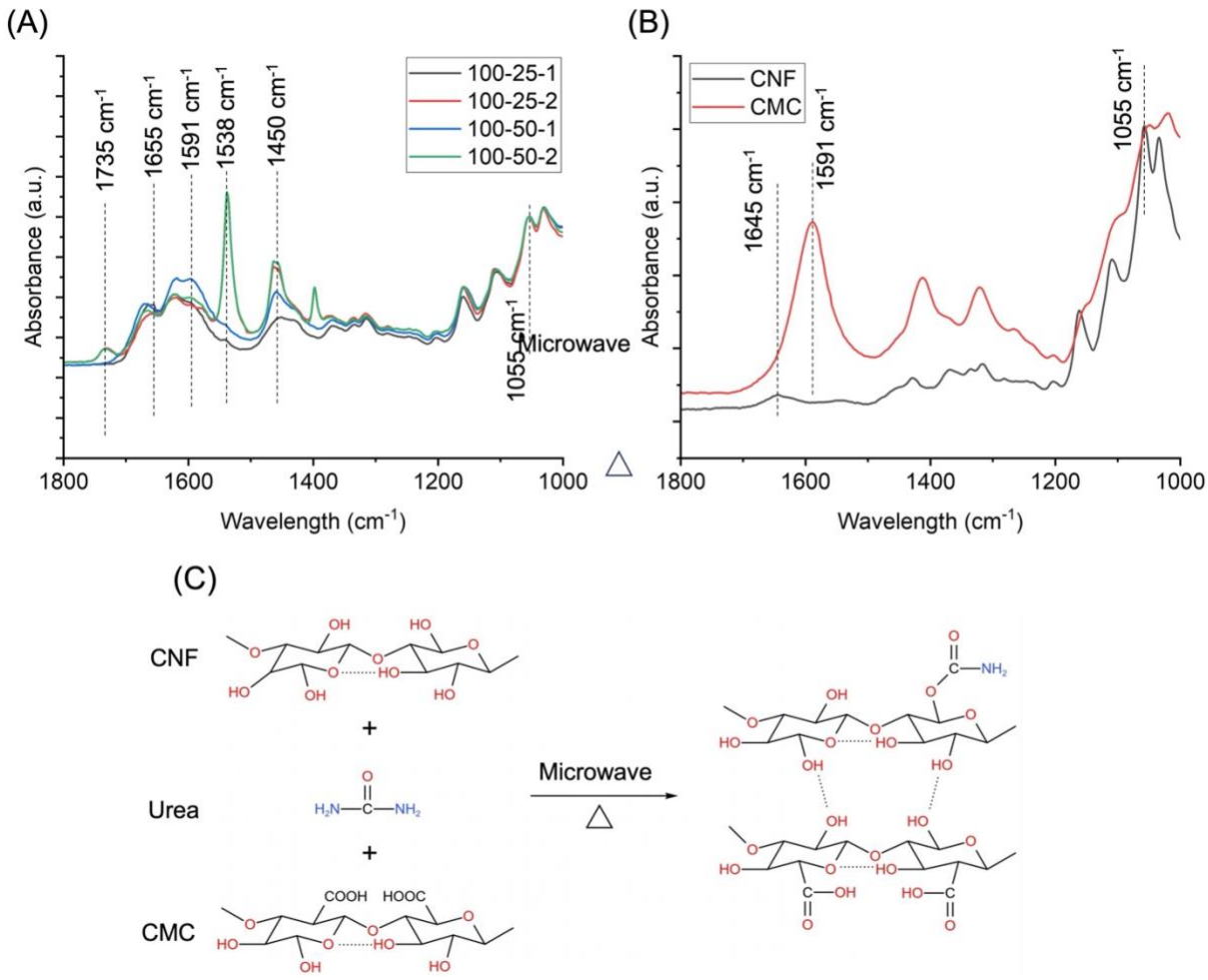

Figure 4.7. FTIR spectra from the fingerprint regions for structures made with different paste formulations (A), neat CNF and CMC (B), and possible chemical interactions upon microwave heating.

4.5.6. Comparison among the cellulose-based 3D printing techniques

Table 4.3 provides a comprehensive comparison of 3D printing techniques utilizing cellulose-based materials. It is important to note that many previous studies have used chemically modified TEMPO–CNF as the main paste or ink component (Baniasadi et al., 2021; Huan et al., 2019; Huang et al., 2019; Mietner et al., 2021). However, TEMPO-CNF is nearly 30 times more expensive than native CNF produced mechanically. In addition, the use of supporting reagents is a significant aspect of these techniques, as they serve to improve printability and crosslink structures to enhance mechanical stability. Numerous of these studies have incorporated

crosslinking agents such as $CaCl_2$ or citric acid via external application or in-situ mixing with cellulose-based ink (Baniasadi et al., 2021; Diaz-Gomez et al., 2022; Huan et al., 2019; Lackner et al., 2022).

This work also distinguished by its independence from the conventional freeze-drying technique in favor of a brief microwave-irradiation procedure. This change offers a significant advantage over alternative approaches. (Ferenczi et al., 2018) have demonstrated that vacuum microwave drying uses approximately 12 times less energy than freeze-drying. This study opts for regular microwave drying as opposed to vacuum, which not only conserves energy but also improves the overall effectiveness of drying printed structures. Hence, this concludes with a straightforward technique for 3D printing with cellulose nanofibrils followed by microwave drying, which offers significant cost and time savings in comparison to existing techniques.

Table 4.3. Comparison of various 3D printing procedures using cellulose-based materials

Cellulose type	Supporting reagents	Total solids content (wt. %)	Processing/ Drying technique	Nozzle diameter	Shrinkage (%)	Reference
TEMPO-CNF	QSM, $CaCl_2$	2	Freezing (-20 °C) and Freeze-drying (48h)	840 µm	7	(Baniasadi et al., 2021)
NFC	CMC and citric acid	7.5 –17.5	Freeze-drying DHT treatment (24 h)	250 µm	–	(Lackner et al., 2022)
CNF	XT, H_2O_2, HRP	7.71–13.6	Submerging in a 1% H_2O_2 solution in water	420 µm	_	(Markstedt et al., 2017)
CNF	CMC	42	Air drying (48 h) and solvent exchange (2 h)	700 µm	32±4 – 34±3 (Height)	(Thibaut et al., 2019)
CMC	Citric acid	15	Freezing (-80 °C) and Freeze-drying (24 h)	410 µm	_	(Diaz-Gomez et al., 2022)
CMC	Alginate	4 – 8	Crosslinked with 4% $CaCl_2$	410 µm	–	(Habib et al., 2018)
BCNF	Silk, gelatin, and GP	22.8 – 23.9	Freeze-drying/ solvent exchange (30 min) & 1 % GP (24 h)	410 µm	–	(Huang et al., 2019)
TEMPO-CNF	$FeCl_2$/ $Al(NO3)_2$/ $CaCl_2$/ $Mg(NO_3)_2$	2.64	Oven drying (Overnight) or freeze-drying	580 or 840 µm	–	(Mietner et al., 2021)
TEMPO-OBC	SF, HRP and H_2O_2	7	Drying at 37 °C (1 h) & freeze-drying (Overnight)	320 µm	–	(Huang et al., 2021)
TEMPO–CNF	Parafin	2.5	Freezing at -20 °C (24 h) and freeze-drying (72 h)	410 µm	20–27	(Zheng et al., 2022)

Table 4.3 continued

CNF	Alginate, PLA and $CaCl_2$	CNF/Alginate: 1.5% and PLA: 12%	Freezing at -18 °C (Overnight) and freeze-drying (> 48 h)	630 µm	5	(Huan et al., 2019)
CNF	Urea and CMC	11.26 – 13.52	Freezing (12 h) and Microwave (7–8 min)	7 mm	30.5 ± 1.1	This work

[a]Abbreviations: TEMPO: 2,2,6,6-tetramethylpiperidine-1-oxyl radical; QSM: quince seed mucilage; NFC: nanofibrillated cellulose; XT: xylan− tyramine; HRP: horseradish peroxidase; GP: Genipin; TEMPO–OBC: 2,2,6,6-tetramethylpiperidine-1-oxyl (TEMPO)-oxidized bacterial cellulose (OBC) nanofibrils; SF: silk fibroin; PLA: polylactide

4.6 Conclusions

A novel method of 3D printing employing native CNFs with urea and CMC additives was developed. Stress sweep tests performed on the 3D printing pastes revealed that an increase in CMC content resulted in a decrease in the yield stress (τ_y), allowing pastes to flow smoothly and uniformly through the printing nozzle. In addition, a higher concentration of CMC resulted in a greater negative surface charge in the CNF paste, although the addition of a greater proportion of urea partially mitigated this effect. Maintaining the urea-to-CMC ratio was identified as a crucial factor for minimizing shrinkage and shape deformation during the microwave drying. In addition, the study revealed that urea and CMC had different effects on the shrinkage of the final dried structures. The formulation with the lowest shrinkage was the one with a dry mass ratio of CNF:urea:CMC = 100:50:1 (30.5% ± 1.1%). Notably, in density-normalized mechanical tests, formulations with a higher CMC content demonstrated statistically superior mechanical properties compared to formulations with a lower CMC content. CMC significantly influenced interlayer adhesion in the z-direction, as shown by SEM images. Lastly, Fourier transform infrared (FTIR) analysis revealed that mutual interactions between CNF, urea, and CMC under microwave irradiation may result in the formation of cellulose esters, as indicated by prominent peaks at 1735 cm^{-1}. This study demonstrated a novel and cost-effective strategy for 3D printing with CNF-based

materials, proposing an alternative microwave-based drying technique which has the potential to promote the use of sustainable nanomaterials in additive manufacturing.

CHAPTER 5

CONCLUSIONS AND FUTURE DIRECTIONS

5.1 Conclusions

In this dissertation, fundamental aspects of CNF-based foam forming mechanism were investigated and applied towards water filtration, molded and additive manufacturing for potential environmental applications.

In chapter 2, the use of CNFs as a support for nanoscale particles was investigated. The results showed that the freeze-dried hybrid CNF aerogels could prevent the nanoparticle agglomeration which effectively increased the arsenic adsorption efficiency from water. This work effectively addressed the shortcomings of using nanoparticles-based fixed bed columns for water treatment system and a potential for using cellulose-based sustainable nanomaterials as a water treatment technology. To further search for an alternative manufacturing technique for hybrid CNF foams in chapter 3, microwave irradiation was applied in accordance with a novel CNF foam forming mechanism. The foams prepared through this technique exhibited similar mechanical properties such as freeze-dried foams. In addition, a new in-situ crosslinking reaction route was proposed which provided a favorable wet-stability of those foams. This newly developed cost and time efficient foam forming method has a potential to scale up the cellulose-based sustainable nanomaterials in diverse range of applications. Chapter 4 extended and modified the novel foam forming technique developed in chapter 3 and successfully applied it in 3D printing. Analyzing the paste rheology and structure's shape retention upon microwave drying; comprehensive understanding was developed. It was found that the mechanical and chemical properties of the structures were highly dependent on the optimized ratio of paste additives. This newly developed cost and time-efficient additive manufacturing technique enable to scale up the cellulose-based 3D printing for a wide range of applications.

The intellectual contribution of this dissertation encompasses the advancement of novel scientific understanding regarding foam formation techniques utilizing cellulose nanomaterials and the feasibility of additive manufacturing and potential strategies for microwave drying of porous structures in a molded foam. The potential of cellulose nanomaterial-based foams for a diverse array of environmental applications was forecasted, in addition to their use in water filtration.

5.2 Recommendations for future directions

For **chapter 2**,

I. Future work may include large-scale testing (i.e. in fixed-bed columns) and the investigation of the adsorbent performance towards other types of contaminants.

II. The recycling of adsorbent media is an important part of any water treatment system. In this work, no recycling or reuse procedure via desorption of arsenic and regeneration of the adsorbent was investigated, which provides an opportunity for future work.

For **chapter 3**,

III. Future research could potentially focus on the examination of additional parameters during the freezing process, such as freezing temperature and airflow direction, which are expected to influence the morphology of the pores.

IV. Future work could focus on assessing the feasibility and challenges of large-scale production of the foams.

V. Although the hybrid foams were successfully formed using nanoparticles with CNF and urea; it remains unclear how the presence of nanoparticles affects the morphology of the pores and formation mechanism.

For **chapter 4**,

VI. Further optimizations of the 3D printing process are still needed in order to develop a better understanding of the printability of CNF paste.

REFERENCES

Abdelhamid, H. N., & Mathew, A. P. (2021). Cellulose-Based Materials for Water Remediation: Adsorption, Catalysis, and Antifouling. *Frontiers in Chemical Engineering*, *3*, 790314. https://doi.org/10.3389/fceng.2021.790314

Aguayo, M., Fernández Pérez, A., Reyes, G., Oviedo, C., Gacitúa, W., Gonzalez, R., & Uyarte, O. (2018). Isolation and Characterization of Cellulose Nanocrystals from Rejected Fibers Originated in the Kraft Pulping Process. *Polymers*, *10*(10), 1145. https://doi.org/10.3390/polym10101145

Alexandrova, A. N., & Jorgensen, W. L. (2007). Why Urea Eliminates Ammonia Rather than Hydrolyzes in Aqueous Solution. *The Journal of Physical Chemistry B*, *111*(4), 720–730. https://doi.org/10.1021/jp066478s

Anirudhan, T. S., Divya, L., & Parvathy, J. (2013). Arsenic adsorption from contaminated water on Fe(III)-coordinated amino-functionalized poly(glycidylmethacrylate)-grafted TiO_2 -densified cellulose: Sorptive potential of a novel anion exchanger. *Journal of Chemical Technology & Biotechnology*, *88*(5), 878–886. https://doi.org/10.1002/jctb.3916

Anirudhan, T. S., Senan, P., & Suchithra, P. S. (2011). Evaluation of Iron(III)-Coordinated Amino-Functionalized Poly(Glycidyl Methacrylate)-Grafted Cellulose for Arsenic(V) Adsorption from Aqueous Solutions. *Water, Air, & Soil Pollution*, *220*(1–4), 101–116. https://doi.org/10.1007/s11270-010-0738-9

Antonini, C., Wu, T., Zimmermann, T., Kherbeche, A., Thoraval, M.-J., Nyström, G., & Geiger, T. (2019). Ultra-Porous Nanocellulose Foams: A Facile and Scalable Fabrication Approach. *Nanomaterials*, *9*(8), 1142. https://doi.org/10.3390/nano9081142

Anwar, J., Shafique, U., Waheed-uz-Zaman, Rehman, R., Salman, M., Dar, A., Anzano, J. M., Ashraf, U., & Ashraf, S. (2015). Microwave chemistry: Effect of ions on dielectric heating in microwave ovens. *Arabian Journal of Chemistry*, *8*(1), 100–104. https://doi.org/10.1016/j.arabjc.2011.01.014

Azrak, S. M. E. A., Gohl, J. A., Moon, R. J., Schueneman, G. T., Davis, C. S., & Youngblood, J. P. (2021). Controlled Dispersion and Setting of Cellulose Nanofibril—Carboxymethyl Cellulose Pastes. *Cellulose*, *28*(14), 9149–9168. https://doi.org/10.1007/s10570-021-04081-5

Baltpurvins, K. A., Burns, R. C., Lawrance, G. A., & Stuart, A. D. (1997). Effect of Ca^{2+} , Mg^{2+} , and Anion Type on the Aging of Iron(III) Hydroxide Precipitates. *Environmental Science & Technology*, *31*(4), 1024–1032. https://doi.org/10.1021/es960498y

Baniasadi, H., Polez, R. T., Kimiaei, E., Madani, Z., Rojas, O. J., Österberg, M., & Seppälä, J. (2021). 3D printing and properties of cellulose nanofibrils-reinforced quince seed mucilage bio-inks. *International Journal of Biological Macromolecules*, *192*, 1098–1107. https://doi.org/10.1016/j.ijbiomac.2021.10.078

Battisha, I. K., Afify, H. H., & Ibrahim, M. (2006). Synthesis of Fe2O3 concentrations and sintering temperature on FTIR and magnetic susceptibility measured from 4 to 300K of monolith silica gel

prepared by sol–gel technique. *Journal of Magnetism and Magnetic Materials*, *306*(2), 211–217. https://doi.org/10.1016/j.jmmm.2006.01.251

Bozkurt, Y., & Karayel, E. (2021). 3D printing technology; methods, biomedical applications, future opportunities and trends. *Journal of Materials Research and Technology*, *14*, 1430–1450. https://doi.org/10.1016/j.jmrt.2021.07.050

Bushell, M., Beauchemin, S., Kunc, F., Gardner, D., Ovens, J., Toll, F., Kennedy, D., Nguyen, K., Vladisavljevic, D., Rasmussen, P. E., & Johnston, L. J. (2020). Characterization of Commercial Metal Oxide Nanomaterials: Crystalline Phase, Particle Size and Specific Surface Area. *Nanomaterials*, *10*(9), 1812. https://doi.org/10.3390/nano10091812

Cai, J., & Zhang, L. (2005). Rapid Dissolution of Cellulose in LiOH/Urea and NaOH/Urea Aqueous Solutions. *Macromolecular Bioscience*, *5*(6), 539–548. https://doi.org/10.1002/mabi.200400222

Cai, L., Liu, Y., & Liang, H. (2012). Impact of hydrogen bonding on inclusion layer of urea to cellulose: Study of molecular dynamics simulation. *Polymer*, *53*(5), 1124–1130. https://doi.org/10.1016/j.polymer.2012.01.008

Casentini, B., Gallo, M., & Baldi, F. (2019). Arsenate and arsenite removal from contaminated water by iron oxides nanoparticles formed inside a bacterial exopolysaccharide. *Journal of Environmental Chemical Engineering*, *7*(1), 102908. https://doi.org/10.1016/j.jece.2019.102908

Cervin, N. T., Johansson, E., Larsson, P. A., & Wågberg, L. (2016). Strong, Water-Durable, and Wet-Resilient Cellulose Nanofibril-Stabilized Foams from Oven Drying. *ACS Applied Materials & Interfaces*, *8*(18), 11682–11689. https://doi.org/10.1021/acsami.6b00924

Chen, C., & Hu, L. (2018). Nanocellulose toward Advanced Energy Storage Devices: Structure and Electrochemistry. *Accounts of Chemical Research*, *51*(12), 3154–3165. https://doi.org/10.1021/acs.accounts.8b00391

Chen, C., Sun, W., Wang, L., Tajvidi, M., Wang, J., & Gardner, D. J. (2022). Transparent Multifunctional Cellulose Nanocrystal Films Prepared Using Trivalent Metal Ion Exchange for Food Packaging. *ACS Sustainable Chemistry & Engineering*, *10*(29), 9419–9430. https://doi.org/10.1021/acssuschemeng.2c01805

Chhajed, M., Yadav, C., Agrawal, A. K., & Maji, P. K. (2019). Esterified superhydrophobic nanofibrillated cellulose based aerogel for oil spill treatment. *Carbohydrate Polymers*, *226*, 115286. https://doi.org/10.1016/j.carbpol.2019.115286

Ciftci, D., Ubeyitogullari, A., Huerta, R. R., Ciftci, O. N., Flores, R. A., & Saldaña, M. D. A. (2017). Lupin hull cellulose nanofiber aerogel preparation by supercritical CO 2 and freeze drying. *The Journal of Supercritical Fluids*, *127*, 137–145. https://doi.org/10.1016/j.supflu.2017.04.002

Da Silva, D. J., & Rosa, D. S. (2022). Chromium removal capability, water resistance and mechanical behavior of foams based on cellulose nanofibrils with citric acid. *Polymer*, *253*, 125023. https://doi.org/10.1016/j.polymer.2022.125023

Dang, B., Chen, Y., Wang, H., Chen, B., Jin, C., & Sun, Q. (2018). Preparation of High Mechanical Performance Nano-Fe3O4/Wood Fiber Binderless Composite Boards for Electromagnetic

Absorption via a Facile and Green Method. *Nanomaterials*, *8*(1), 52. https://doi.org/10.3390/nano8010052

Darezereshki, E. (2011). One-step synthesis of hematite (α-Fe2O3) nano-particles by direct thermal-decomposition of maghemite. *Materials Letters*, *65*(4), 642–645. https://doi.org/10.1016/j.matlet.2010.11.030

Darpentigny, C., Nonglaton, G., Bras, J., & Jean, B. (2020). Highly absorbent cellulose nanofibrils aerogels prepared by supercritical drying. *Carbohydrate Polymers*, *229*, 115560. https://doi.org/10.1016/j.carbpol.2019.115560

Das, S., Hendry, M. J., & Essilfie-Dughan, J. (2011). Transformation of Two-Line Ferrihydrite to Goethite and Hematite as a Function of pH and Temperature. *Environmental Science & Technology*, *45*(1), 268–275. https://doi.org/10.1021/es101903y

Demitri, C., Giuri, A., Raucci, M. G., Giugliano, D., Madaghiele, M., Sannino, A., & Ambrosio, L. (2014). Preparation and characterization of cellulose-based foams via microwave curing. *Interface Focus*, *4*(1), 20130053. https://doi.org/10.1098/rsfs.2013.0053

Diaz-Gomez, L., Gonzalez-Prada, I., Millan, R., Da Silva-Candal, A., Bugallo-Casal, A., Campos, F., Concheiro, A., & Alvarez-Lorenzo, C. (2022). 3D printed carboxymethyl cellulose scaffolds for autologous growth factors delivery in wound healing. *Carbohydrate Polymers*, *278*, 118924. https://doi.org/10.1016/j.carbpol.2021.118924

Dong, F., Xu, X., Shaghaleh, H., Guo, J., Guo, L., Qian, Y., Liu, H., & Wang, S. (2020). Factors influencing the morphology and adsorption performance of cellulose nanocrystal/iron oxide nanorod composites for the removal of arsenic during water treatment. *International Journal of Biological Macromolecules*, *156*, 1418–1424. https://doi.org/10.1016/j.ijbiomac.2019.11.182

El Awad Azrak, S. M., Costakis, W. J., Moon, R. J., Schueneman, G. T., & Youngblood, J. P. (2020). Continuous Processing of Cellulose Nanofibril Sheets Through Conventional Single-Screw Extrusion. *ACS Applied Polymer Materials*, *2*(8), 3365–3377. https://doi.org/10.1021/acsapm.0c00477

Eyholzer, Ch., Bordeanu, N., Lopez-Suevos, F., Rentsch, D., Zimmermann, T., & Oksman, K. (2010). Preparation and characterization of water-redispersible nanofibrillated cellulose in powder form. *Cellulose*, *17*(1), 19–30. https://doi.org/10.1007/s10570-009-9372-3

Farrell, J., & Chaudhary, B. K. (2013). Understanding Arsenate Reaction Kinetics with Ferric Hydroxides. *Environmental Science & Technology*, *47*(15), 8342–8347. https://doi.org/10.1021/es4013382

Fauziyah, M., Widiyastuti, W., Balgis, R., & Setyawan, H. (2019). Production of cellulose aerogels from coir fibers via an alkali–urea method for sorption applications. *Cellulose*, *26*(18), 9583–9598. https://doi.org/10.1007/s10570-019-02753-x

Fei, P., Liao, L., Cheng, B., & Song, J. (2017). Quantitative analysis of cellulose acetate with a high degree of substitution by FTIR and its application. *Analytical Methods*, *9*(43), 6194–6201. https://doi.org/10.1039/C7AY02165H

Ferenczi, S., Molnár, H., Adányi, N., & Cserhalmi, Z. (2018). *Comparison of Microwave Vacuum-, Freeze- and Hot-Air Drying by Energy Efficiency and Aroma Composition of Dried Hop (Humulus lupulus)*.

Fischer, P. H. H., & McDowell, C. A. (1960). THE INFRARED ABSORPTION SPECTRA OF UREA–HYDROCARBON ADDUCTS. *Canadian Journal of Chemistry*, *38*(2), 187–193. https://doi.org/10.1139/v60-025

French, A. D. (2014). Idealized powder diffraction patterns for cellulose polymorphs. *Cellulose*, *21*(2), 885–896. https://doi.org/10.1007/s10570-013-0030-4

Ghosh, A., Chakrabarti, S., & Ghosh, U. C. (2014). Fixed-bed column performance of Mn-incorporated iron(III) oxide nanoparticle agglomerates on As(III) removal from the spiked groundwater in lab bench scale. *Chemical Engineering Journal*, *248*, 18–26. https://doi.org/10.1016/j.cej.2014.03.010

Gibson, L. J., & Ashby, M. F. (1997). *Cellular Solids: Structure and Properties* (2nd ed.). Cambridge University Press; Cambridge Core. https://doi.org/10.1017/CBO9781139878326

González-Ugarte, A. S., Hafez, I., & Tajvidi, M. (2020). Characterization and properties of hybrid foams from nanocellulose and kaolin-microfibrillated cellulose composite. *Scientific Reports*, *10*(1), 17459. https://doi.org/10.1038/s41598-020-73899-z

Gordeyeva, K. S., Fall, A. B., Hall, S., Wicklein, B., & Bergström, L. (2016). Stabilizing nanocellulose-nonionic surfactant composite foams by delayed Ca-induced gelation. *Journal of Colloid and Interface Science*, *472*, 44–51. https://doi.org/10.1016/j.jcis.2016.03.031

Gross, B. C., Erkal, J. L., Lockwood, S. Y., Chen, C., & Spence, D. M. (2014). Evaluation of 3D Printing and Its Potential Impact on Biotechnology and the Chemical Sciences. *Analytical Chemistry*, *86*(7), 3240–3253. https://doi.org/10.1021/ac403397r

Guo, Y., Zhou, J., Song, Y., & Zhang, L. (2009). An Efficient and Environmentally Friendly Method for the Synthesis of Cellulose Carbamate by Microwave Heating: An Efficient and Environmentally Friendly Method for …. *Macromolecular Rapid Communications*, *30*(17), 1504–1508. https://doi.org/10.1002/marc.200900238

Guo, Y., Zhou, J., Wang, Y., Zhang, L., & Lin, X. (2010). An efficient transformation of cellulose into cellulose carbamates assisted by microwave irradiation. *Cellulose*, *17*(6), 1115–1125. https://doi.org/10.1007/s10570-010-9446-2

Habib, A., Sathish, V., Mallik, S., & Khoda, B. (2018). 3D Printability of Alginate-Carboxymethyl Cellulose Hydrogel. *Materials*, *11*(3), 454. https://doi.org/10.3390/ma11030454

Hafez, I., Amini, E., & Tajvidi, M. (2020). The synergy between cellulose nanofibrils and calcium carbonate in a hybrid composite system. *Cellulose*, *27*(7), 3773–3787. https://doi.org/10.1007/s10570-020-03032-w

Hafez, I., & Tajvidi, M. (2021). Comprehensive Insight into Foams Made of Thermomechanical Pulp Fibers and Cellulose Nanofibrils via Microwave Radiation. *ACS Sustainable Chemistry & Engineering*, *9*(30), 10113–10122. https://doi.org/10.1021/acssuschemeng.1c01816

Halonen, S., Kangas, T., Haataja, M., & Lassi, U. (2017). Urea-Water-Solution Properties: Density, Viscosity, and Surface Tension in an Under-Saturated Solution. *Emission Control Science and Technology*, *3*(2), 161–170. https://doi.org/10.1007/s40825-016-0051-1

Hao, L., Liu, M., Wang, N., & Li, G. (2018). A critical review on arsenic removal from water using iron-based adsorbents. *RSC Advances*, *8*(69), 39545–39560. https://doi.org/10.1039/C8RA08512A

Hasan, I., Wang, J., & Tajvidi, M. (2021). Tuning physical, mechanical and barrier properties of cellulose nanofibril films through film drying techniques coupled with thermal compression. *Cellulose*, *28*(18), 11345–11366. https://doi.org/10.1007/s10570-021-04269-9

Holm Kristensen, J., Bampos, N., & Duer, M. (2004). Solid state 13C CP MAS NMR study of molecular motions and interactions of urea adsorbed on cotton cellulose. *Physical Chemistry Chemical Physics*, *6*(12), 3175. https://doi.org/10.1039/b403537b

Hospodarova, V., Singovszka, E., & Stevulova, N. (2018). Characterization of Cellulosic Fibers by FTIR Spectroscopy for Their Further Implementation to Building Materials. *American Journal of Analytical Chemistry*, *09*(06), 303–310. https://doi.org/10.4236/ajac.2018.96023

Hossain, R., Tajvidi, M., Bousfield, D., & Gardner, D. J. (2022). Recyclable grease-proof cellulose nanocomposites with enhanced water resistance for food serving applications. *Cellulose*, *29*(10), 5623–5643. https://doi.org/10.1007/s10570-022-04608-4

Hossen, M. R., Dadoo, N., Holomakoff, D. G., Co, A., Gramlich, W. M., & Mason, M. D. (2018). Wet stable and mechanically robust cellulose nanofibrils (CNF) based hydrogel. *Polymer*, *151*, 231–241. https://doi.org/10.1016/j.polymer.2018.07.016

Hu, X., Ding, Z., Zimmerman, A. R., Wang, S., & Gao, B. (2015). Batch and column sorption of arsenic onto iron-impregnated biochar synthesized through hydrolysis. *Water Research*, *68*, 206–216. https://doi.org/10.1016/j.watres.2014.10.009

Huan, S., Ajdary, R., Bai, L., Klar, V., & Rojas, O. J. (2019). Low Solids Emulsion Gels Based on Nanocellulose for 3D-Printing. *Biomacromolecules*, *20*(2), 635–644. https://doi.org/10.1021/acs.biomac.8b01224

Huang, L., Du, X., Fan, S., Yang, G., Shao, H., Li, D., Cao, C., Zhu, Y., Zhu, M., & Zhang, Y. (2019). Bacterial cellulose nanofibers promote stress and fidelity of 3D-printed silk based hydrogel scaffold with hierarchical pores. *Carbohydrate Polymers*, *221*, 146–156. https://doi.org/10.1016/j.carbpol.2019.05.080

Huang, L., Yuan, W., Hong, Y., Fan, S., Yao, X., Ren, T., Song, L., Yang, G., & Zhang, Y. (2021). 3D printed hydrogels with oxidized cellulose nanofibers and silk fibroin for the proliferation of lung epithelial stem cells. *Cellulose*, *28*(1), 241–257. https://doi.org/10.1007/s10570-020-03526-7

Huber, T., Starling, K., Cen, W. (Samantha), Fee, C., & Dimartino, S. (2016). Effect of Urea Concentration on the Viscosity and Thermal Stability of Aqueous NaOH/Urea Cellulose Solutions. *Journal of Polymers*, *2016*, 1–9. https://doi.org/10.1155/2016/2658747

Iacob, M., Cazacu, M., Turta, C., Doroftei, F., Botko, M., Čižmár, E., Zeleňáková, A., & Feher, A. (2015). Amorphous iron–chromium oxide nanoparticles with long-term stability. *Materials Research Bulletin*, *65*, 163–168. https://doi.org/10.1016/j.materresbull.2015.01.055

Isogai, A., Usuda, M., Kato, T., Uryu, T., & Atalla, R. H. (1989). Solid-state CP/MAS carbon-13 NMR study of cellulose polymorphs. *Macromolecules*, *22*(7), 3168–3172. https://doi.org/10.1021/ma00197a045

Jandura, P., Kokta, B. V., & Riedl, B. (2000). Fibrous long-chain organic acid cellulose esters and their characterization by diffuse reflectance FTIR spectroscopy, solid-state CP/MAS13C-NMR, and X-ray diffraction. *Journal of Applied Polymer Science*, *78*(7), 1354–1365. https://doi.org/10.1002/1097-4628(20001114)78:7<1354::AID-APP60>3.0.CO;2-V

Jiang, S., Zhang, M., Li, M., Zhu, J., Ge, A., Liu, L., & Yu, J. (2021). Cellulose-based composite thermal-insulating foams toward eco-friendly, flexible and flame-retardant. *Carbohydrate Polymers*, *273*, 118544. https://doi.org/10.1016/j.carbpol.2021.118544

Jiang, Z., Fang, Y., Xiang, J., Ma, Y., Lu, A., Kang, H., Huang, Y., Guo, H., Liu, R., & Zhang, L. (2014). Intermolecular Interactions and 3D Structure in Cellulose–NaOH–Urea Aqueous System. *The Journal of Physical Chemistry B*, *118*(34), 10250–10257. https://doi.org/10.1021/jp501408e

Jorfi, M., & Foster, E. J. (2015). Recent advances in nanocellulose for biomedical applications. *Journal of Applied Polymer Science*, *132*(14), n/a-n/a. https://doi.org/10.1002/app.41719

Joshi, S., Sharma, M., Kumari, A., Shrestha, S., & Shrestha, B. (2019). Arsenic Removal from Water by Adsorption onto Iron Oxide/Nano-Porous Carbon Magnetic Composite. *Applied Sciences*, *9*(18), 3732. https://doi.org/10.3390/app9183732

Josset, S., Hansen, L., Orsolini, P., Griffa, M., Kuzior, O., Weisse, B., Zimmermann, T., & Geiger, T. (2017). Microfibrillated cellulose foams obtained by a straightforward freeze–thawing–drying procedure. *Cellulose*, *24*(9), 3825–3842. https://doi.org/10.1007/s10570-017-1377-8

Jungst, T., Smolan, W., Schacht, K., Scheibel, T., & Groll, J. (2016). Strategies and Molecular Design Criteria for 3D Printable Hydrogels. *Chemical Reviews*, *116*(3), 1496–1539. https://doi.org/10.1021/acs.chemrev.5b00303

Kondo, T. (1997). The assignment of IR absorption bands due to free hydroxyl groups in cellulose. *Cellulose*, *4*, 12.

Korhonen, J. T., Kettunen, M., Ras, R. H. A., & Ikkala, O. (2011). Hydrophobic Nanocellulose Aerogels as Floating, Sustainable, Reusable, and Recyclable Oil Absorbents. *ACS Applied Materials & Interfaces*, *3*(6), 1813–1816. https://doi.org/10.1021/am200475b

Kumar, V., Ottesen, V., Syverud, K., Gregersen, Ø. W., & Toivakka, M. (2017). Coatability of cellulose nanofibril suspensions: Role of rheology and water retention. *BioResources*, *12*(4), 7656–7679. https://doi.org/10.15376/biores.12.4.7656-7679

Lackner, F., Liu, H., Štiglic, A. D., Bračič, M., Kargl, R., Nidetzky, B., Mohan, T., & Kleinschek, K. S. (2022). 3D Printed Porous Nanocellulose-Based Scaffolds As Carriers for Immobilization of Glycosyltransferases. *ACS Applied Bio Materials*, *5*(12), 5728–5740. https://doi.org/10.1021/acsabm.2c00763

LakshmiBalasubramaniam, S., Patel, A. S., Nayak, B., Howell, C., & Skonberg, D. (2021). Antioxidant and antimicrobial modified cellulose nanofibers for food applications. *Food Bioscience*, *44*, 101421. https://doi.org/10.1016/j.fbio.2021.101421

Lassoued, A., Lassoued, M. S., Dkhil, B., Gadri, A., & Ammar, S. (2017). Structural, optical and morphological characterization of Cu-doped α-Fe 2 O 3 nanoparticles synthesized through co-precipitation technique. *Journal of Molecular Structure*, *1148*, 276–281. https://doi.org/10.1016/j.molstruc.2017.07.051

Lavoine, N., & Bergström, L. (2017). Nanocellulose-based foams and aerogels: Processing, properties, and applications. *Journal of Materials Chemistry A*, *5*(31), 16105–16117. https://doi.org/10.1039/C7TA02807E

Li, L., Maddalena, L., Nishiyama, Y., Carosio, F., Ogawa, Y., & Berglund, L. A. (2022). Recyclable nanocomposites of well-dispersed 2D layered silicates in cellulose nanofibril (CNF) matrix. *Carbohydrate Polymers*, *279*, 119004. https://doi.org/10.1016/j.carbpol.2021.119004

Li, T., Aspler, J., Kingsland, A., Cormier, L. M., & Zou, X. (n.d.). *3D PRINTING – A REVIEW OF TECHNOLOGIES, MARKETS, AND OPPORTUNITIES FOR THE FOREST INDUSTRY*. *5*(2).

Li, Y., Tanna, V. A., Zhou, Y., Winter, H. H., Watkins, J. J., & Carter, K. R. (2017). Nanocellulose Aerogels Inspired by Frozen Tofu. *ACS Sustainable Chemistry & Engineering*, *5*(8), 6387–6391. https://doi.org/10.1021/acssuschemeng.7b01608

Liao, X., Zhu, J., Zhong, W., & Chen, H.-Y. (2001). Synthesis of amorphous Fe2O3 nanoparticles by microwave irradiation. *Materials Letters*, *50*(5–6), 341–346. https://doi.org/10.1016/S0167-577X(01)00251-8

Liu, H., Li, P., Qiu, F., Zhang, T., & Xu, J. (2020). Controllable preparation of FeOOH/CuO@WBC composite based on water bamboo cellulose applied for enhanced arsenic removal. *Food and Bioproducts Processing*, *123*, 177–187. https://doi.org/10.1016/j.fbp.2020.06.018

Liu, P., Sehaqui, H., Tingaut, P., Wichser, A., Oksman, K., & Mathew, A. P. (2014). Cellulose and chitin nanomaterials for capturing silver ions (Ag+) from water via surface adsorption. *Cellulose*, *21*(1), 449–461. https://doi.org/10.1007/s10570-013-0139-5

Macera, L., Taglieri, G., Daniele, V., Passacantando, M., & D'Orazio, F. (2020). Nano-Sized Fe(III) Oxide Particles Starting from an Innovative and Eco-Friendly Synthesis Method. *Nanomaterials*, *10*(2), 323. https://doi.org/10.3390/nano10020323

Markstedt, K., Escalante, A., Toriz, G., & Gatenholm, P. (2017). Biomimetic Inks Based on Cellulose Nanofibrils and Cross-Linkable Xylans for 3D Printing. *ACS Applied Materials & Interfaces*, *9*(46), 40878–40886. https://doi.org/10.1021/acsami.7b13400

Mazhari Mousavi, S. M., Afra, E., Tajvidi, M., Bousfield, D. W., & Dehghani-Firouzabadi, M. (2017). Cellulose nanofiber/carboxymethyl cellulose blends as an efficient coating to improve the structure and barrier properties of paperboard. *Cellulose*, *24*(7), 3001–3014. https://doi.org/10.1007/s10570-017-1299-5

Mietner, J. B., Jiang, X., Edlund, U., Saake, B., & Navarro, J. R. G. (2021). 3D printing of a bio-based ink made of cross-linked cellulose nanofibrils with various metal cations. *Scientific Reports*, *11*(1), 6461. https://doi.org/10.1038/s41598-021-85865-4

Mingos, D. M. P., & Baghurst, D. R. (1991). Tilden Lecture. Applications of microwave dielectric heating effects to synthetic problems in chemistry. *Chemical Society Reviews*, *20*(1), 1. https://doi.org/10.1039/cs9912000001

Mohammed, N., Grishkewich, N., & Tam, K. C. (2018). Cellulose nanomaterials: Promising sustainable nanomaterials for application in water/wastewater treatment processes. *Environmental Science: Nano*, *5*(3), 623–658. https://doi.org/10.1039/C7EN01029J

Mohan, D., & Pittman, C. U. (2007). Arsenic removal from water/wastewater using adsorbents—A critical review. *Journal of Hazardous Materials*, *142*(1), 1–53. https://doi.org/10.1016/j.jhazmat.2007.01.006

Mohapatra, M., Hariprasad, D., Mohapatra, L., Anand, S., & Mishra, B. K. (2012). Mg-doped nano ferrihydrite—A new adsorbent for fluoride removal from aqueous solutions. *Applied Surface Science*, *258*(10), 4228–4236. https://doi.org/10.1016/j.apsusc.2011.12.047

Mondal, P., Balomajumder, C., & Mohanty, B. (2007). A laboratory study for the treatment of arsenic, iron, and manganese bearing ground water using Fe3+ impregnated activated carbon: Effects of shaking time, pH and temperature. *Journal of Hazardous Materials*, *144*(1–2), 420–426. https://doi.org/10.1016/j.jhazmat.2006.10.078

Moon, R. J., Martini, A., Nairn, J., Simonsen, J., & Youngblood, J. (2011). Cellulose nanomaterials review: Structure, properties and nanocomposites. *Chemical Society Reviews*, *40*(7), 3941. https://doi.org/10.1039/c0cs00108b

Müller, L. A. E., Zingg, A., Arcifa, A., Zimmermann, T., Nyström, G., Burgert, I., & Siqueira, G. (2022). Functionalized Cellulose Nanocrystals as Active Reinforcements for Light-Actuated 3D-Printed Structures. *ACS Nano*, *16*(11), 18210–18222. https://doi.org/10.1021/acsnano.2c05628

Müller, Y., Tot, I., Potthast, A., Rosenau, T., Zimmermann, R., Eichhorn, K.-J., Nitschke, C., Scherr, G., Freudenberg, U., & Werner, C. (2010). The impact of esterification reactions on physical properties of cellulose thin films. *Soft Matter*, *6*(15), 3680. https://doi.org/10.1039/c0sm00005a

Najib, N., & Christodoulatos, C. (2019). Removal of arsenic using functionalized cellulose nanofibrils from aqueous solutions. *Journal of Hazardous Materials*, *367*, 256–266. https://doi.org/10.1016/j.jhazmat.2018.12.067

Nechita, P., & Năstac, S. M. (2022). Overview on Foam Forming Cellulose Materials for Cushioning Packaging Applications. *Polymers*, *14*(10), 1963. https://doi.org/10.3390/polym14101963

Nicomel, N., Leus, K., Folens, K., Van Der Voort, P., & Du Laing, G. (2015). Technologies for Arsenic Removal from Water: Current Status and Future Perspectives. *International Journal of Environmental Research and Public Health*, *13*(1), 62. https://doi.org/10.3390/ijerph13010062

Nirmaan, A. M. C., Rohitha Prasantha, B. D., & Peiris, B. L. (2020). Comparison of microwave drying and oven-drying techniques for moisture determination of three paddy (Oryza sativa L.)

varieties. *Chemical and Biological Technologies in Agriculture*, *7*(1), 1. https://doi.org/10.1186/s40538-019-0164-1

Noerdlinger, P. D., & Brower, K. R. (2007). The melting of floating ice raises the ocean level. *Geophysical Journal International*, *170*(1), 145–150. https://doi.org/10.1111/j.1365-246X.2007.03472.x

Obokata, T., & Isogai, A. (2007). The mechanism of wet-strength development of cellulose sheets prepared with polyamideamine-epichlorohydrin (PAE) resin. *Colloids and Surfaces A: Physicochemical and Engineering Aspects*, *302*(1–3), 525–531. https://doi.org/10.1016/j.colsurfa.2007.03.025

Onyianta, A. J., Dorris, M., & Williams, R. L. (2018). Aqueous morpholine pre-treatment in cellulose nanofibril (CNF) production: Comparison with carboxymethylation and TEMPO oxidisation pre-treatment methods. *Cellulose*, *25*(2), 1047–1064. https://doi.org/10.1007/s10570-017-1631-0

Padmavathy, K. S., Madhu, G., & Haseena, P. V. (2016). A study on Effects of pH, Adsorbent Dosage, Time, Initial Concentration and Adsorption Isotherm Study for the Removal of Hexavalent Chromium (Cr (VI)) from Wastewater by Magnetite Nanoparticles. *Procedia Technology*, *24*, 585–594. https://doi.org/10.1016/j.protcy.2016.05.127

Park, S. Y., Goo, S., Shin, H., Kim, J., & Youn, H. J. (2021). Structural properties of cellulose nanofibril foam depending on wet foaming conditions in Pickering stabilization. *Cellulose*, *28*(16), 10291–10304. https://doi.org/10.1007/s10570-021-04151-8

Parks, G. A. (1965). The isoelectric points of solid oxides, solid hydroxides, and aqueous hydroxy complex systems. *Chemical Reviews*, *65*, 177–198.

Phanthong, P., Reubroycharoen, P., Hao, X., Xu, G., Abudula, A., & Guan, G. (2018). Nanocellulose: Extraction and application. *Carbon Resources Conversion*, *1*(1), 32–43. https://doi.org/10.1016/j.crcon.2018.05.004

Phu, N. D., Ngo, D. T., Hoang, L. H., Luong, N. H., Chau, N., & Hai, N. H. (2011). Crystallization process and magnetic properties of amorphous iron oxide nanoparticles. *Journal of Physics D: Applied Physics*, *44*(34), 345002. https://doi.org/10.1088/0022-3727/44/34/345002

Poletto, M., Pistor, V., Zeni, M., & Zattera, A. J. (2011). Crystalline properties and decomposition kinetics of cellulose fibers in wood pulp obtained by two pulping processes. *Polymer Degradation and Stability*, *96*(4), 679–685. https://doi.org/10.1016/j.polymdegradstab.2010.12.007

Qing, Y., Wu, Y., Cai, Z., & Li, X. (2013). Water-Triggered Dimensional Swelling of Cellulose Nanofibril Films: Instant Observation Using Optical Microscope. *Journal of Nanomaterials*, *2013*, 1–6. https://doi.org/10.1155/2013/594734

Rabani, I., Yoo, J., Kim, H.-S., Lam, D. V., Hussain, S., Karuppasamy, K., & Seo, Y.-S. (2021). Highly dispersive Co_3O_4 nanoparticles incorporated into a cellulose nanofiber for a high-performance flexible supercapacitor. *Nanoscale*, *13*(1), 355–370. https://doi.org/10.1039/D0NR06982E

Rahman, M. M., Hafez, I., Tajvidi, M., & Amirbahman, A. (2021). Highly Efficient Iron Oxide Nanoparticles Immobilized on Cellulose Nanofibril Aerogels for Arsenic Removal from Water. *Nanomaterials*, *11*(11), 2818. https://doi.org/10.3390/nano11112818

Rahman, M. M., Hafez, I., Tajvidi, M., & Amirbahman, A. (2023). Fundamentals of Hybrid Cellulose Nanofibril Foam Production by Microwave-Assisted Thawing/Drying Mechanism. *ACS Sustainable Chemistry & Engineering*, *11*(36), 13240–13250. https://doi.org/10.1021/acssuschemeng.3c00599

Ratnaike, R. (2003). Acute and chronic arsenic toxicity. *Postgraduate Medical Journal*, *79*(933), 391–396. https://doi.org/10.1136/pmj.79.933.391

Regand, A., & Goff, H. D. (2003). Structure and ice recrystallization in frozen stabilized ice cream model systems. *Food Hydrocolloids*, *17*(1), 95–102. https://doi.org/10.1016/S0268-005X(02)00042-5

Rezus, Y. L. A., & Bakker, H. J. (2006). Effect of urea on the structural dynamics of water. *Proceedings of the National Academy of Sciences*, *103*(49), 18417–18420. https://doi.org/10.1073/pnas.0606538103

Rodriguez, D. M. P. (2010). *A Thesis Presented to The Academic Faculty*. 203.

Salahuddin, B., Aziz, S., Gao, S., Hossain, Md. S. A., Billah, M., Zhu, Z., & Amiralian, N. (2022). Magnetic Hydrogel Composite for Wastewater Treatment. *Polymers*, *14*(23), 5074. https://doi.org/10.3390/polym14235074

Segal, L., & Eggerton, F. V. (1961). Some Aspects of the Reaction between Urea and Cellulose. *Textile Research Journal*, *31*(5), 460–471. https://doi.org/10.1177/004051756103100510

Shankar, S., Shanker, U., & Shikha. (2014). Arsenic Contamination of Groundwater: A Review of Sources, Prevalence, Health Risks, and Strategies for Mitigation. *The Scientific World Journal*, *2014*, 1–18. https://doi.org/10.1155/2014/304524

Shaw, W. H. R., & Bordeaux, J. J. (1955). The Decomposition of Urea in Aqueous Media. *Journal of the American Chemical Society*, *77*(18), 4729–4733. https://doi.org/10.1021/ja01623a011

Singh, K., Sinha, T. J. M., & Srivastava, S. (2015). Functionalized nanocrystalline cellulose: Smart biosorbent for decontamination of arsenic. *International Journal of Mineral Processing*, *139*, 51–63. https://doi.org/10.1016/j.minpro.2015.04.014

Siqueira, G., Kokkinis, D., Libanori, R., Hausmann, M. K., Gladman, A. S., Neels, A., Tingaut, P., Zimmermann, T., Lewis, J. A., & Studart, A. R. (2017). Cellulose Nanocrystal Inks for 3D Printing of Textured Cellular Architectures. *Advanced Functional Materials*, *27*(12), 1604619. https://doi.org/10.1002/adfm.201604619

Smedley, P. L., & Kinniburgh, D. G. (2002). A review of the source, behaviour and distribution of arsenic in natural waters. *Applied Geochemistry*, *17*(5), 517–568. https://doi.org/10.1016/S0883-2927(02)00018-5

Stumm, W., & Morgan, J. J. (2012). *Aquatic chemistry: chemical equilibria and rates in natural waters*. John Wiley & Sons.

Sun, J., Wang, W., & Yue, Q. (2016). Review on Microwave-Matter Interaction Fundamentals and Efficient Microwave-Associated Heating Strategies. *Materials*, *9*(4), 231. https://doi.org/10.3390/ma9040231

Tan, J. Z. Y., Ávila-López, M. A., Jahanbakhsh, A., Lu, X., Bonilla-Cruz, J., Lara-Ceniceros, T. E., Andresen, J. M., & Maroto-Valer, M. M. (2023). 3D direct ink printed materials for chemical conversion and environmental remediation applications: A review. *Journal of Materials Chemistry A*, *11*(11), 5408–5426. https://doi.org/10.1039/D2TA08922J

Tang, W., Su, Y., Li, Q., Gao, S., & Shang, J. K. (2013). Superparamagnetic magnesium ferrite nanoadsorbent for effective arsenic (III, V) removal and easy magnetic separation. *Water Research*, *47*(11), 3624–3634. https://doi.org/10.1016/j.watres.2013.04.023

Tauhiduzzaman, M., Hafez, I., Bousfield, D., & Tajvidi, M. (2021). Modeling Microwave Heating and Drying of Lignocellulosic Foams through Coupled Electromagnetic and Heat Transfer Analysis. *Processes*, *9*(11), 2001. https://doi.org/10.3390/pr9112001

Thibaut, C., Denneulin, A., Rolland Du Roscoat, S., Beneventi, D., Orgéas, L., & Chaussy, D. (2019). A fibrous cellulose paste formulation to manufacture structural parts using 3D printing by extrusion. *Carbohydrate Polymers*, *212*, 119–128. https://doi.org/10.1016/j.carbpol.2019.01.076

Tian, Y., Wu, M., Liu, R., Wang, D., Lin, X., Liu, W., Ma, L., Li, Y., & Huang, Y. (2011). Modified native cellulose fibers—A novel efficient adsorbent for both fluoride and arsenic. *Journal of Hazardous Materials*, *185*(1), 93–100. https://doi.org/10.1016/j.jhazmat.2010.09.001

Tracey, C. T., Predeina, A. L., Krivoshapkina, E. F., & Kumacheva, E. (2022). A 3D printing approach to intelligent food packaging. *Trends in Food Science & Technology*, *127*, 87–98. https://doi.org/10.1016/j.tifs.2022.05.003

Trache, D., Tarchoun, A. F., Derradji, M., Hamidon, T. S., Masruchin, N., Brosse, N., & Hussin, M. H. (2020). Nanocellulose: From Fundamentals to Advanced Applications. *Frontiers in Chemistry*, *8*, 392. https://doi.org/10.3389/fchem.2020.00392

Velu, R., Raspall, F., & Singamneni, S. (2019). 3D printing technologies and composite materials for structural applications. In *Green Composites for Automotive Applications* (pp. 171–196). Elsevier. https://doi.org/10.1016/B978-0-08-102177-4.00008-2

Voisin, H., Bergström, L., Liu, P., & Mathew, A. (2017). Nanocellulose-Based Materials for Water Purification. *Nanomaterials*, *7*(3), 57. https://doi.org/10.3390/nano7030057

Wang, D., Feng, X., Zhang, L., Li, M., Liu, M., Tian, A., & Fu, S. (2019). Cyclotriphosphazene-bridged periodic mesoporous organosilica-integrated cellulose nanofiber anisotropic foam with highly flame-retardant and thermally insulating properties. *Chemical Engineering Journal*, *375*, 121933. https://doi.org/10.1016/j.cej.2019.121933

Wen, Z., Zhang, Y., Dai, C., Chen, B., Guo, S., Yu, H., & Wu, D. (2014). Synthesis of ordered mesoporous iron manganese bimetal oxides for arsenic removal from aqueous solutions. *Microporous and Mesoporous Materials*, *200*, 235–244. https://doi.org/10.1016/j.micromeso.2014.08.049

Wicklein, B., Kocjan, A., Salazar-Alvarez, G., Carosio, F., Camino, G., Antonietti, M., & Bergström, L. (2015). Thermally insulating and fire-retardant lightweight anisotropic foams based on nanocellulose and graphene oxide. *Nature Nanotechnology*, *10*(3), 277–283. https://doi.org/10.1038/nnano.2014.248

Willberg-Keyriläinen, P., Hiltunen, J., & Ropponen, J. (2018). Production of cellulose carbamate using urea-based deep eutectic solvents. *Cellulose*, *25*(1), 195–204. https://doi.org/10.1007/s10570-017-1465-9

Xiao, S., Gao, R., Lu, Y., Li, J., & Sun, Q. (2015). Fabrication and characterization of nanofibrillated cellulose and its aerogels from natural pine needles. *Carbohydrate Polymers*, *119*, 202–209. https://doi.org/10.1016/j.carbpol.2014.11.041

Xiong, L.-K., Yu, G.-M., & Yin, C.-Y. (2017). Synthesis and characterization of cellulose carbamate by liquid-solid phase method. *Fibers and Polymers*, *18*(1), 88–94. https://doi.org/10.1007/s12221-017-5758-2

Yadav, C., Saini, A., Zhang, W., You, X., Chauhan, I., Mohanty, P., & Li, X. (2021). Plant-based nanocellulose: A review of routine and recent preparation methods with current progress in its applications as rheology modifier and 3D bioprinting. *International Journal of Biological Macromolecules*, *166*, 1586–1616. https://doi.org/10.1016/j.ijbiomac.2020.11.038

Yi, T., Zhao, H., Mo, Q., Pan, D., Liu, Y., Huang, L., Xu, H., Hu, B., & Song, H. (2020). From Cellulose to Cellulose Nanofibrils—A Comprehensive Review of the Preparation and Modification of Cellulose Nanofibrils. *Materials*, *13*(22), 5062. https://doi.org/10.3390/ma13225062

Yousif, A. M., Zaid, O. F., & Ibrahim, I. A. (2016). Fast and selective adsorption of As(V) on prepared modified cellulose containing Cu(II) moieties. *Arabian Journal of Chemistry*, *9*(5), 607–615. https://doi.org/10.1016/j.arabjc.2015.02.004

Yu, X. (2013). One-step synthesis of magnetic composites of cellulose@iron oxide nanoparticles for arsenic removal. *J. Mater. Chem. A*, *1*(3), 959–965. https://doi.org/10.1039/C2TA00315E

Yu, X., Tong, S., Ge, M., Wu, L., Zuo, J., Cao, C., & Song, W. (2013). Synthesis and characterization of multi-amino-functionalized cellulose for arsenic adsorption. *Carbohydrate Polymers*, *92*(1), 380–387. https://doi.org/10.1016/j.carbpol.2012.09.050

Zeng, H., Zhai, L., Qiao, T., Yu, Y., Zhang, J., & Li, D. (2020). Efficient removal of As(V) from aqueous media by magnetic nanoparticles prepared with Iron-containing water treatment residuals. *Scientific Reports*, *10*(1), 9335. https://doi.org/10.1038/s41598-020-65840-1

Zhang, C., Su, J., Zhu, H., Xiong, J., Liu, X., Li, D., Chen, Y., & Li, Y. (2017). The removal of heavy metal ions from aqueous solutions by amine functionalized cellulose pretreated with microwave-H_2O_2. *RSC Advances*, *7*(54), 34182–34191. https://doi.org/10.1039/C7RA03056H

Zhang, F., Wei, M., Viswanathan, V. V., Swart, B., Shao, Y., Wu, G., & Zhou, C. (2017). 3D printing technologies for electrochemical energy storage. *Nano Energy*, *40*, 418–431. https://doi.org/10.1016/j.nanoen.2017.08.037

Zhang, M., Li, M., Xu, Q., Jiang, W., Hou, M., Guo, L., Wang, N., Zhao, Y., & Liu, L. (2022). Nanocellulose-based aerogels with devisable structure and tunable properties via ice-template

induced self-assembly. *Industrial Crops and Products*, *179*, 114701. https://doi.org/10.1016/j.indcrop.2022.114701

Zhang, W., Zhang, Y., Lu, C., & Deng, Y. (2012). Aerogels from crosslinked cellulose nano/micro-fibrils and their fast shape recovery property in water. *Journal of Materials Chemistry*, *22*(23), 11642. https://doi.org/10.1039/c2jm30688c

Zhang, Y., Li, J., Ma, N., Meng, Z., & Sui, G. (2019). Processing cellulose@Fe3O4 into mechanical, magnetic and biodegradable synapse-like material. *Composites Part B: Engineering*, *177*, 107432. https://doi.org/10.1016/j.compositesb.2019.107432

Zheng, Y., Zhu, Y., Yu, Z., Zhu, J., Zhang, Y., Ye, Y., Zheng, D., & Jiang, F. (2022). Passive thermal regulation with 3D printed phase change material/cellulose nanofibrils composites. *Composites Part B: Engineering*, *247*, 110332. https://doi.org/10.1016/j.compositesb.2022.110332

Zhu, H., Yang, X., Cranston, E. D., & Zhu, S. (2016). Flexible and Porous Nanocellulose Aerogels with High Loadings of Metal-Organic-Framework Particles for Separations Applications. *Advanced Materials*, *28*(35), 7652–7657. https://doi.org/10.1002/adma.201601351

APPENDICES

APPENDIX A. SUPPORTING INFORMATION FOR CHAPTER 2

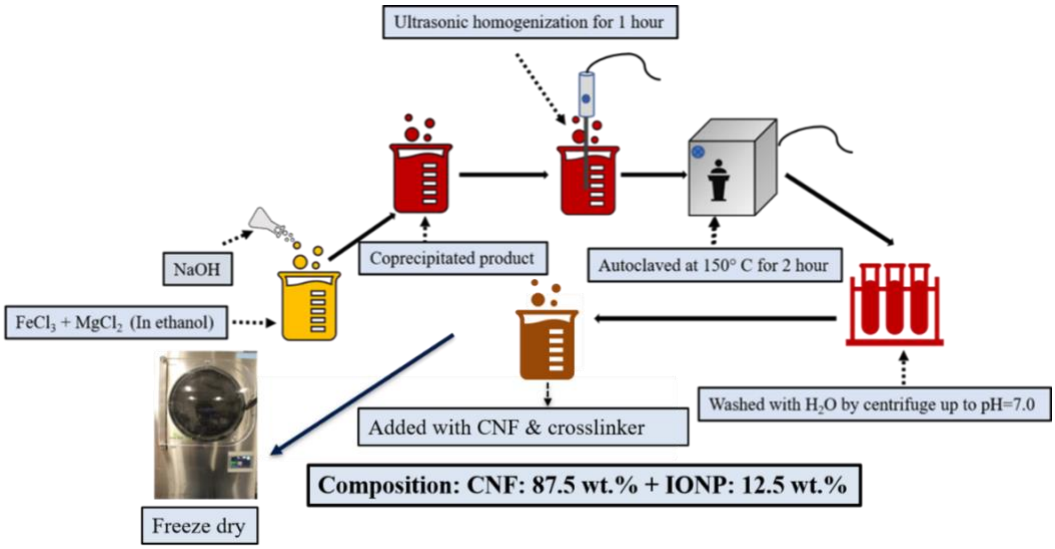

Figure A1. The summery of preparatory scheme for CNF-IONP aerogel

Table A1. Summary of aerogel formulation before and after the incorporation of IONP

	CNF		IONP		Crosslinker (CL)		Adsorbent
Sample name	CNF wt. (%)	CNF dry mass (mg)	IONP wt. (%)	IONP dry mass (mg)	CL wt. % (Based on dry CNF)	CL dry mass (mg)	Adsorbent dry mass (mg)
CNF Aerogel	100	35	0	5	5	0.07	35.07
CNF-IONP Aerogel	87.5	35	12.5	5	5	0.07	40.07

Figure A2. Proposed reaction mechanism between cellulose and Polycup™

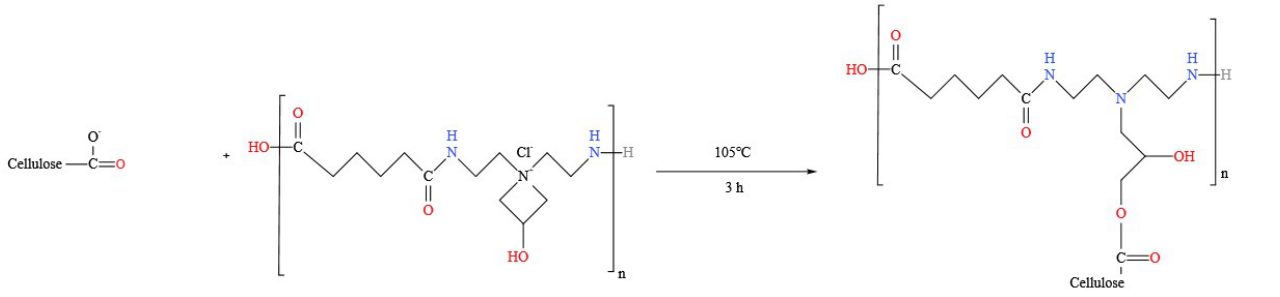

Cellulose with carboxylate group Polycup™ (polyamide-epichlorohydrin) 5150 cross-linker Cellulose crosslinked with PolycupTM (polyamide-epichlorohydrin) 5150 cross-linker

Figure A3. The FT-IR spectrum of crosslinked and un-crosslinked CNF aerogel

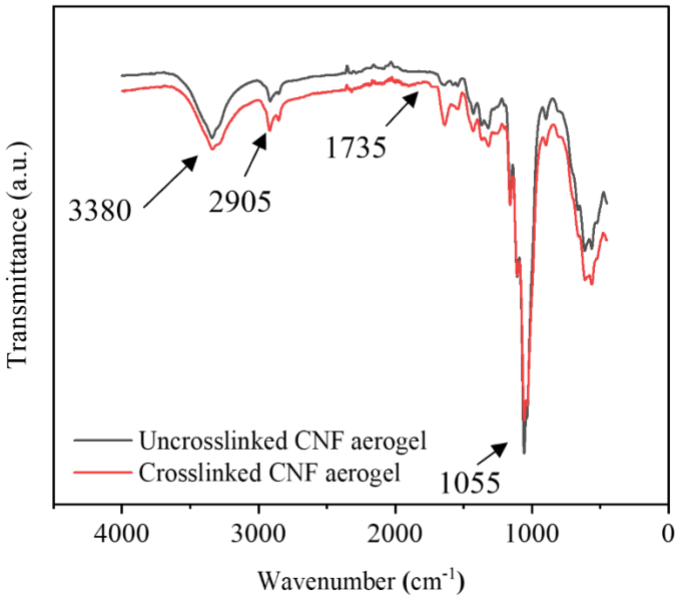

APPENDIX B. SUPPORTING INFORMATION FOR CHAPTER 3

Foam characterization

The density, ρ (g/cm^3), and porosity, Ø (%), of the foams were calculated by measuring the solid volume of the foams (V_S) using an Accupyc II gas pycnometry system (Micromeritics Instrument Corporation, Norcross, GA, USA) and the total geometric volume (V_T) by a digital caliper and corresponding mass (m) according to the equations B1 and B2, respectively.

$$\text{Density, } \rho \text{ (g/cm}^3\text{)} = \frac{m}{V_T} \quad \text{(B1)}$$

$$\text{Porosity, Ø (\%)} = \left(1 - \frac{V_S}{V_T}\right) \times 100 \quad \text{(B2)}$$

The volumetric shrinkage (%) was calculated by measuring the total geometric volume of the foams (V_T) and the mold (V_{Mold}) using equation B3.

$$\text{Volumetric shrinkage (\%)} = \frac{V_{Mold} - V_{Total}}{V_{Mold}} \times 100 \quad \text{(B3)}$$

For both wet and dry foams, compressive properties were evaluated using an Instron 5942 (Instron Corporation, Norwood, MA, USA) equipped with a 500 N load cell. All tests were conducted according to a modified ASTM C165 standard method at a test speed of 0.89 mm/min. All the samples were cut into 3 × 3 cm specimens and conditioned before testing. The compressive strengths at two different strain levels (10% and 25%) were reported and the compressive modulus was calculated from the corresponding linear-elastic region on the stress-strain curve. For wet testing, the foams were immersed in water for 2 min and excess water was removed by a paper towel prior to testing.

Statistical analysis

One-way analysis of variance (ANOVA) was performed to determine the statistical significance between the means of the measured properties. Duncan's Multiple Range Test (DMRT) was conducted as a post hoc test to evaluate the specific differences among the pairs of means. All analyses were performed using IBM SPSS Statistics 25 software (Armonk, NY, USA) at a 95% confidence level.

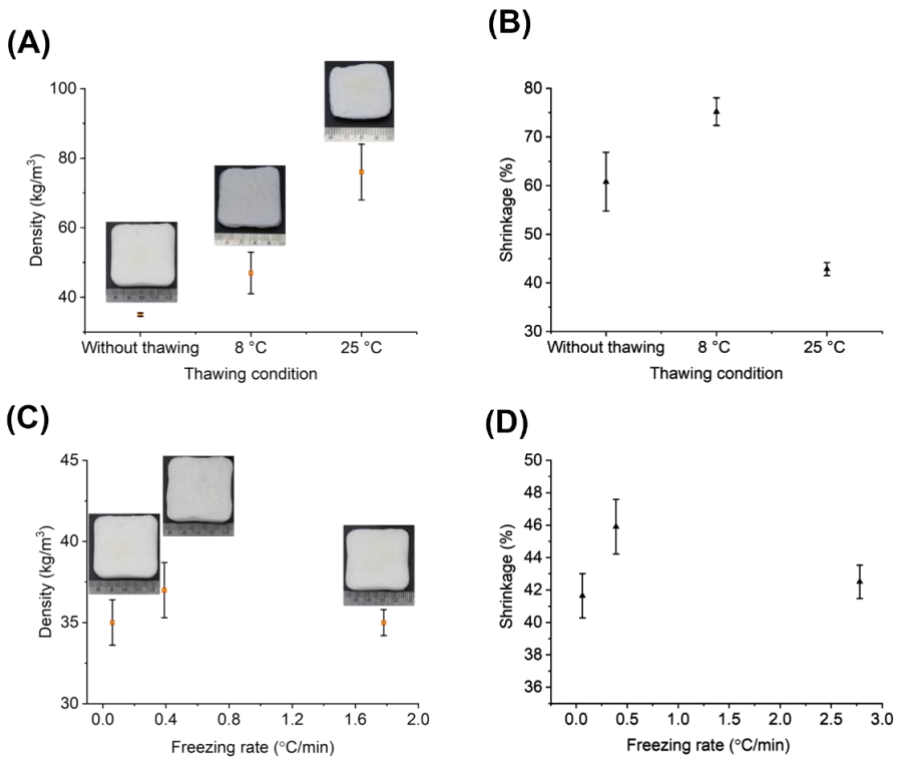

Figure B1. Variations in the density and volume shrinkage of UCNF foams with 25 wt% urea content at different thawing conditions (A, B) and freezing rate (C, D). The error bars represent one standard deviation. The digital photograph for each type of samples is shown on the corresponding density plot.

Table B1. Summary of compressive properties for freeze-dried CNF without urea and with 5% Polycup, UCNF with 25% urea, and UCNF-IONP foams with 25% urea and 3% IONPs along Z direction[a]

				Specific compressive strength ($kPa.m^3/kg$)	
Foam type	Condition	Density (kg/m^3)	Specific Young's modulus ($kPa.m^3/kg$)	At 10% strain	At 25% strain
Freeze-dried CNF	Dry	27.4 (1.1)^{A}	5.8 (1.1)^{A}	0.71 (0.15)^{A}	1.63 (0.03)^{A}
	Wet	27.4 (1.1)^{A}	0.6 (0.1)^{B}	0.02 (0.00)^{C}	0.05 (0.01)^{C}
UCNF	Dry	36.3 (1.3)^{B}	6.0 (2.2)^{A}	0.50 (0.12)^{B}	1.0 (0.16)^{B}
	Wet	36.7 (1.0)^{B}	0.3 (0.1)^{C}	0.03 (0.01)^{C}	0.07 (0.01)^{D}
UCNF-IONP	Dry	38.4 (1.4)^{B}	4.5 (0.6)^{A}	0.42 (0.07)^{B}	0.86 (0.06)^{B}
	Wet	36.9 (1.9)^{B}	0.4 (0.1)^{C}	0.03 (0.00)^{C}	0.07 (0.00)^{D}

[a]Values at parenthesis represents the standard deviation among there replicates for each group. Means with the same letters within each column are not statistically different within 95% confidence interval (P > 0.05).

APPENDIX C. SUPPORTING INFORMATION FOR CHAPTER 4

Table C1: Optimized printing process parameters for CNF-based 3D printing

Parameter name	Value	Unit	Description
Linear movement	17.2	mm/s	The linear movement speed of the extruder head
Extruder diameter	7	mm	The orifice diameter of the nozzle
Layer height	5	mm	Distance incremented between each layer
Extrusion width	8.53 (±0.6)	mm	The width of the non-circular printing path
Piston speed	6.4	mm/min	The speed of the nozzle piston
Gravimetric flowrate	25.8 (±1.6)	gm/min	Gravimetric flow rate, calculated from piston speed and nozzle diameter
Layer infill	100 (Cuboids)	%	Amount of material used to fill the model volume
Perimeters	1 (Cuboids)		Number of external shells
Infill pattern	Grid (Cuboids)		Pattern used in the infill
First layer height	5	mm	Distance between the syringe tip and printing platform during the first layer

Table C2. Summary of mechanical properties of the 3D printed structures manufactured with differently formulated pastes [a]

Structure formulation (CNF-urea-CMC) (pph)	Density (g/cm^3)	Compressive modulus ($MPa.cm^3/g$)	Compressive strength at 15% strain ($MPa.cm^3/g$)	Compressive strength at 25% strain ($MPa.cm^3/g$)	Tensile modulus ($MPa.cm^3/g$)	Tensile strength ($MPa.cm^3/g$)
100–25–1	0.15^{A}	10.1 ± 0.6^{A}	1.8 ± 0.2^{A}	4.0 ± 0.3^{A}	24.1 ± 4.4^{A}	0.8 ± 0.1^{A}
100–25–2	0.19^{B}	16.9 ± 0.6^{B}	3.3 ± 0.1^{B}	7.3 ± 0.5^{B}	47.8 ± 1.4^{B}	1.4 ± 0.2^{B}
100–50–1	0.15^{A}	9.3 ± 0.9^{A}	1.8 ± 0.1^{A}	3.3 ± 0.1^{A}	33.1 ± 2.4^{A}	1.0 ± 0.1^{A}
100–50–2	0.19^{B}	22.1 ± 0.9^{B}	3.6 ± 0.1^{B}	7 ± 0.1^{B}	67.9 ± 15.7^{C}	1.4 ± 0.1^{B}

[a] Values at parenthesis represents the standard deviation among three replicates for each group. Means with the same letters within each column are not statistically different within 95% confidence interval (P > 0.05).

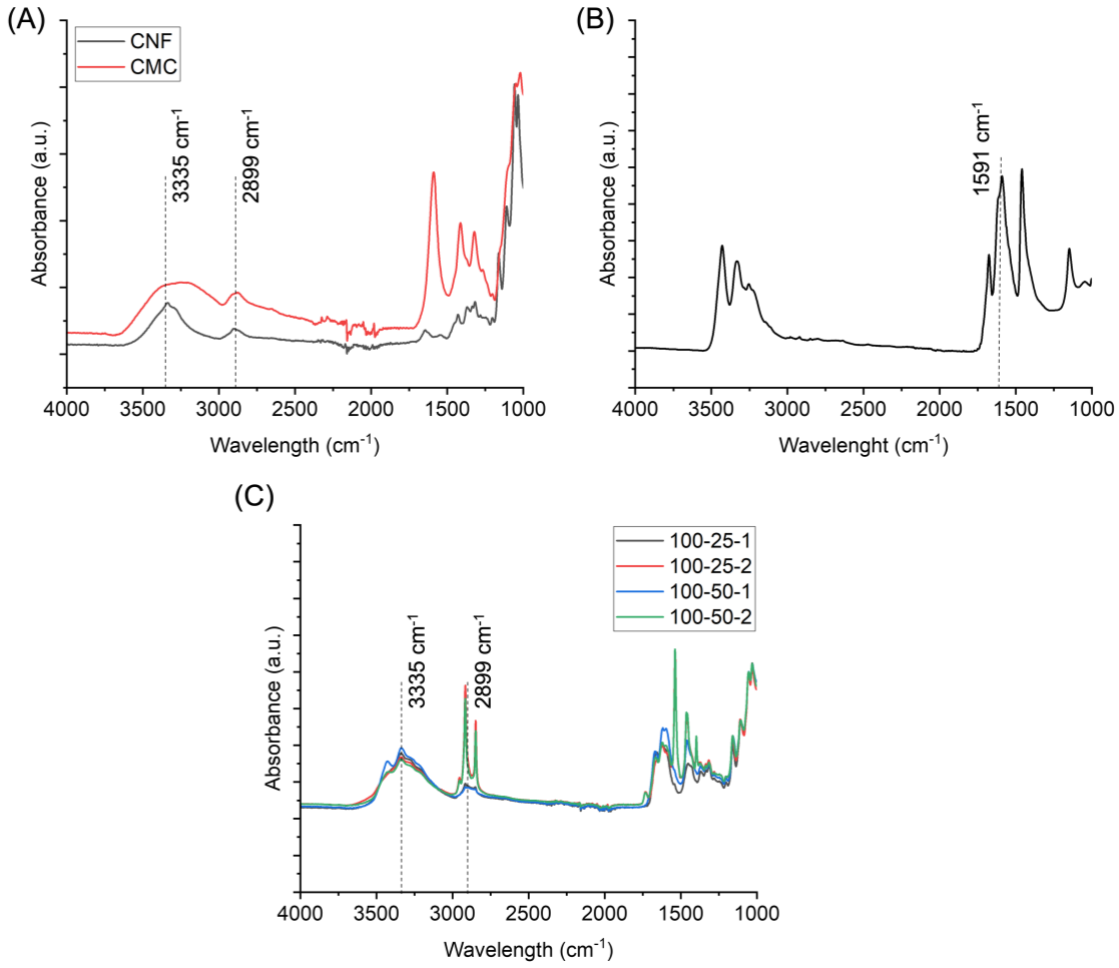

Figure C1. FTIR spectra for CNF and CMC (A), solid urea (B) and structures made with different paste formulations.

BIOGRAPHY OF THE AUTHOR

Md Musfiqur Rahman was born in Chittagong, Bangladesh. He attended Shahjalal University of Science & Technology, Sylhet and graduated in 2017 with a Bachelor's degree in Chemistry and a Master's degree in Physical Chemistry in 2019. He started his PhD in Forest Resources with a concentration in Bioproducts Engineering at the School of Forest Resources, University of Maine in spring 2020. His work involved investigation of low-density cellulose nanomaterials-based foams/aerogels for environmental applications. Musfiqur is a candidate for the Doctor of Philosophy degree in Forest Resources with a concentration in Bioproducts Engineering from the University of Maine in December 2023.